

NORTHWESTERN UNIVERSITY

Bimetallic Effects in the Homopolymerization of Styrene and Copolymerization of Ethylene and Styrenic Comonomers. Scope, Kinetics, and Mechanism/Catalytic In Situ Synthesis of High Energy Storage Density Metal Oxide-Polyolefin Nanocomposites Using Supported Metallocenes. Systematics of Nanoparticle, Shape, and Interfacial Characteristics on Leakage Current Density, Permittivity, and Breakdown Strength

A DISSERTATION

SUBMITTED TO THE GRADUATE SCHOOL
IN PARTIAL FULFILLMENTS OF THE REQUIREMENTS

for the degree

DOCTOR OF PHILOSOPHY

Field of Chemistry

By

Neng Guo

EVANSTON, ILLINOIS

December 2007

© Copyright by Neng Guo 2007

All Rights Reserved

ABSTRACT

Bimetallic Effects in the Homopolymerization of Styrene and Copolymerization of Ethylene and Styrenic Comonomers. Scope, Kinetics, and Mechanism/Catalytic In Situ Synthesis of High Energy Storage Density Metal Oxide-Polyolefin Nanocomposites Using Supported Metallocenes. Systematics of Nanoparticle, Shape, and Interfacial Characteristics on Leakage Current Density, Permittivity, and Breakdown Strength

Neng Guo

Chapter 1 describes the homopolymerization of styrene and the copolymerization of ethylene and styrenic comonomers mediated by the single-site bimetallic “constrained geometry catalysts” (CGCs), $(\mu\text{-CH}_2\text{CH}_2\text{-3,3}')\{\eta^5\text{-indenyl}\}[1\text{-Me}_2\text{Si}(\text{tBuN})(\text{TiMe}_2)]_2$ [EBICGC(TiMe₂)₂; **Ti₂**], $(\mu\text{-CH}_2\text{CH}_2\text{-3,3}')\{\eta^5\text{-indenyl}\}[1\text{-Me}_2\text{Si}(\text{tBuN})(\text{ZrMe}_2)]_2$ [EBICGC(ZrMe₂)₂; **Zr₂**], $(\mu\text{-CH}_2\text{-3,3}')\{\eta^5\text{-indenyl}\}[1\text{-Me}_2\text{Si}(\text{tBuN})(\text{TiMe}_2)]_2$ [MBICGC(TiMe₂)₂; **C1-Ti₂**], and $(\mu\text{-CH}_2\text{-3,3}')\{\eta^5\text{-indenyl}\}[1\text{-Me}_2\text{Si}(\text{tBuN})(\text{ZrMe}_2)]_2$ [MBICGC(ZrMe₂)₂; **C1-Zr₂**], in combination with the borate activator/cocatalyst $\text{Ph}_3\text{C}^+\text{B}(\text{C}_6\text{F}_5)_4^-$ (**B₁**). Under identical styrene homopolymerization conditions, **C1-Ti₂ + B₁** and **Ti₂ + B₁** exhibit ~ 65 and ~ 35 times greater polymerization activities, respectively, than does monometallic $[1\text{-Me}_2\text{Si}(3\text{-ethylindenyl})(\text{tBuN})]\text{TiMe}_2$ (**Ti₁**) + **B₁**. **C1-Zr₂ + B₁** and **Zr₂ + B₁** exhibit ~ 8 and ~ 4 times greater polymerization activities, respectively, than does the monometallic control $[1\text{-Me}_2\text{Si}(3\text{-ethylindenyl})(\text{tBuN})]\text{ZrMe}_2$ (**Zr₁**) + **B₁**. NMR analyses show that the bimetallic catalysts suppress the regiochemical insertion selectivity exhibited by the monometallic analogues. In ethylene copolymerization, **Ti₂ + B₁** enchains 15.4% more styrene (**B**), 28.9% more 4-methylstyrene (**C**), 45.4% more 4-fluorostyrene (**D**), 41.2% more 4-chlorostyrene (**E**), and 31.0% more 4-bromostyrene (**F**) than does **Ti₁ + B₁**.

This observed bimetallic chemoselectivity effect follows the same general trend as the electron density on the styrenic *ipso* carbon ($\mathbf{D} > \mathbf{E} > \mathbf{F} > \mathbf{C} > \mathbf{B}$). Kinetic studies reveal that both $\mathbf{Ti}_2 + \mathbf{B}_1$ and $\mathbf{Ti}_1 + \mathbf{B}_1$ -mediated ethylene + styrene copolymerizations follow second-order Markovian statistics and tend to be alternating. Moreover, calculated reactivity ratios indicate that $\mathbf{Ti}_2 + \mathbf{B}_1$ favors styrene insertion more than does $\mathbf{Ti}_1 + \mathbf{B}_1$. All the organozirconium complexes ($\mathbf{C1-Zr}_2$, \mathbf{Zr}_2 , and \mathbf{Zr}_1) are found to be incompetent for ethylene + styrene copolymerization, yielding only mixtures of polyethylene and polystyrene. Model compound $(\mu\text{-CH}_2\text{CH}_2\text{-3,3'})\{(\eta^5\text{-indenyl})[1\text{-Me}_2\text{Si}(\text{tBuN})][\text{Ti}(\text{CH}_2\text{Ph})_2]\}_2$ {EBICGC[Ti(CH₂Ph)₂]₂; $\mathbf{Ti}_2(\mathbf{CH}_2\mathbf{Ph})_4$ } was designed, synthesized, and characterized. In situ activation studies with cocatalyst B(C₆F₅)₃ suggest an η^1 -coordination mode for the benzyl groups, thus supporting the proposed mechanism. For ethylene + styrene copolymerization, polar solvents are found to increase copolymerization activities and coproduce atactic polystyrene impurities in addition to ethylene-co-styrene, without diminishing the comonomer incorporation selectivity. Both homopolymerization and copolymerization results argue that substantial cooperative effects between catalytic sites are operative.

In Chapter 2, a series of 0-3 metal oxide-polyolefin nanocomposites is synthesized via in situ olefin polymerization using the metallocene catalysts *C*₂-symmetric dichloro[*rac*-ethylenebisindenyl]zirconium(IV) (EBIZrCl₂), Me₂Si(*t*BuN)(η^5 -C₅Me₄)TiCl₂ (CGCTiCl₂), and (η^5 -C₅Me₅)TiCl₃ (Cp*TiCl₃) immobilized on methylaluminoxane (MAO)-treated barium titanate (BaTiO₃), zirconium dioxide (ZrO₂), 3 mol% yttria-stabilized zirconia (TZ3Y), 8 mol% yttria-stabilized zirconia (TZ8Y), *sphere*-shaped titanium dioxide (TiO₂), and *rod*-shaped TiO₂ nanoparticles. The resulting composite materials are characterized by X-ray diffraction (XRD), scanning electron microscopy (SEM), transmission electron microscopy (TEM), ¹³C nuclear magnetic resonance (NMR) spectroscopy, and differential scanning calorimetry (DSC). It is

shown by TEM that the nanoparticles are well-dispersed in the polymer matrix and each individual nanoparticle is surrounded by polymer. Electrical measurements reveal that most of the nanocomposites have leakage current densities $\sim 10^{-8}$ - 10^{-6} A/cm², and the relative permittivities of the nanocomposites increase as the nanoparticle volume fraction increases, with measured values as high as 6.1. At the same volume fraction, *rod*-shaped TiO₂ nanoparticle-polypropylene nanocomposites exhibit greater relative permittivities than the corresponding *sphere*-shaped TiO₂ nanoparticle-polypropylene nanocomposites. The energy densities of these nanocomposites are estimated to be as high as 9.4 J/cm³.

ACKNOWLEDGEMENTS

First, I would like to thank my advisor, Professor Tobin Marks for his guidance and patience through my whole graduate school career. What impresses me most is his hardworking and curiosity of the nature, which continuously motivates and inspires me to pursue and learn new things. I feel lucky to have had the opportunity to work in Tobin's group and learn so many things like chemistry, presentation skills, manuscript drafting, and communication skills. I think he perfectly defines what a great scientist and advisor should be. I would also like to thank my committee members, Prof. Ibers, Prof. Stair, and Prof. Nguyen, for asking me challenging questions and providing valuable suggestions for my research projects.

I learned so many things from lots of people that I met in graduate school. Particularly, Dr. Liting Li, who is my mentor, not only taught me useful lab skills like how to synthesize air-sensitive compounds and how to do polymerizations, but also showed me how to design and tackle a scientific project, how to plan career goals, and how to have a meaningful life. Some of his original and insightful ideas are still inspiring the current Marks group members. Dr. Sven Schneider, a very typical German scholar, provided me with lots of interesting conversations ranging from organometallic chemistry and politics to European cultures. His strict scientific attitude helped shape my way of doing research and solving problems. Dr. Aswini Dash and Dr. Cristiano Zuccaccia always amazed me with their indefinite professional knowledge and readiness to help anybody. Dr. Bruce Yu and Dr. Hua Jiang both set very good examples for me by working over 90 hours per week.

The next bunch of people not only taught me chemistry, but also helped me improve my English and adapt to the new environment. Tryg Jensen, Sukwon Hong, Jaesang Ryu, and Bryan Stubbert demonstrated to me how hardworking graduate students should be. Tryg Jensen's

tremendous funny stories like “fresh water sushi” and “frog on a rocket” often filled the lab with laughter. Amber Kawaoka was always fun to talk to, regardless of topics. I really appreciated her forgiveness and patience whenever I made stupid mistakes in the lab. Bryan Stubbert’s literature knowledge always pushed me to read more and his “diet coke + peanut butter jelly sandwich” lunch made me realize that life could have been much simpler. Hongbo Li was always capable of getting polymerizations to work and his productiveness set a good example for me. John Roberts’ brightness and creativity constantly inspired me and it has always been a great pleasure to intellectually interact with him. Mike Salata was always ready to discuss organometallic chemistry and his question “any luck this weekend” frequently amused me. Neeraj Saraya’s expertise in cars and music benefited me a lot. Working together with Smruti Amin and Holming Yuen always reminded me how many responsibilities I should take. Special thanks to Staci Wegener for listening to me in the past year. It was these people who made graduate school more interesting and memorable.

I am also grateful to those outside the Marks group who rendered my graduate school experience more colorful and less stressful. Hai Yuan and Xiaoyu Zhang shared lots of joy and sorrow with me in the past five years. Hai’s great sense of humor is always a good way to relieve stress. Linshi Li constantly encouraged me to try my best and stick to what I think is the most important to me. Without them, graduate school life could have been totally different.

Last but certainly not least, I’d like to thank my family for their love and support throughout my whole life. From the very beginning, Mom and Dad have been making every effort to get me the best education. It is their encouragement, understanding, and forgiveness that have shaped me what I am now and what I will be in the future. It is to them that I dedicate this work.

To My Family

TABLE OF CONTENTS

Abstract.....	3
Acknowledgements.....	6
Dedication.....	8
Table of Contents.....	9
List of Schemes.....	11
List of Tables.....	12
List of Charts.....	12
List of Figures.....	13
Chapter 1. Bimetallic Effects in Homopolymerization of Styrene and Copolymerization of Ethylene and Styrenic Comonomers. Scope, Kinetics, and Mechanism.....	16
Abstract.....	17
Introduction.....	19
Experimental Section.....	26
Materials and Methods.....	26
Physical and Analytical Measurements.....	27
Styrene Homopolymerization Experiments in Toluene.....	28
Ethylene Copolymerization Experiments in Toluene.....	29
Ethylene Copolymerization Experiments in Chlorobenzene.....	29
Determination of Comonomer Content by ¹ H NMR.....	30
Solvent Fractionation of Ethylene- <i>co</i> -styrene and Polystyrene Mixtures.....	30
Synthesis of Bimetallic Metallocene Complex Ti₂Cl₄	31
Synthesis of Bimetallic Metallocene Complex Ti₂(CH₂Ph)₄	31
In Situ NMR Study of the Bimetallic Metallocene Ion Pair [Ti₂(CH₂Ph)₂]²⁺[PhCH₂B(C₆F₅)₃]₂⁻	32
X-ray Crystal Structure Determination of Ti₂(CH₂Ph)₄	33
Results.....	34
Kinetic Analyses of Ethylene + Styrene Copolymerization Mediated by Ti₂ + B₁ and Ti₁ + B₁	34
Copolymerization of Ethylene and Styrenic Comonomers.....	45
Copolymerization of Ethylene and Styrene by Mononuclear and Binuclear Organozirconium Catalysts.....	54
Homopolymerization of Styrene and End Group Analysis.....	56
Polar Solvent Effects.....	63
Synthesis, Characterization, and Activation Studies of the Model Compound Ti₂(CH₂Ph)₄	66
Molecular Structure of Model Compound Ti₂(CH₂Ph)₄	69

	10
Discussion.....	73
Bimetallic Proximity Effects in Polymerization.....	73
Comparison between CGCTi ⁺ and CGCZr ⁺ Catalytic Properties.....	74
Bimetallic Effects on Comonomer Enchainment.....	75
Solvent Polarity Effects on Polymerization.....	77
Activation Studies of Model Compound Ti ₂ (CH ₂ Ph) ₄	79
Conclusions.....	79
Chapter 2. Catalytic In Situ Synthesis of High Energy Storage Density Metal Oxide-Polyolefin Nanocomposites Using Supported Metallocenes. Systematics of Nanoparticle, Shape, and Interfacial Characteristics on Leakage Current Density, Permittivity, and Breakdown Strength.....	82
Abstract.....	83
Introduction.....	84
Experimental Section.....	88
Materials and Methods.....	88
Physical and Analytical Measurements.....	89
Electrical Measurements.....	90
Immobilization of Metallocene Catalysts on Metal Oxide Nanoparticles.....	90
Representative Synthesis of Nanocomposites via In Situ Propylene Polymerization.....	91
Results.....	91
Synthesis of Metal Oxide-Polyolefin Nanocomposites.....	92
Nanocomposites Microstructural Properties.....	99
Nanocomposite Permittivity Properties.....	99
Leakage Current Density Measurement Results.....	104
Breakdown Strength Measurements and Nanocomposite Energy Density.....	104
Discussion.....	112
Nanocomposite Synthesis and Characterization.....	112
Function of the Cocatalyst MAO.....	113
Effect of Nanoparticle Shape on Nanocomposite Permittivity.....	113
Conclusions.....	117
References.....	118
Chapter 1.....	119
Chapter 2.....	129
Curriculum Vitae.....	134

List of Schemes**Chapter 1**

- Scheme 1-1.** Proposed Mechanistic Scenario for Enhanced Comonomer Enchainment by Bimetallic Catalysts..... 21
- Scheme 1-2.** Propagation Patterns in Ethylene + Styrene Copolymerization for a First-Order Markovian Statistical Model..... 36
- Scheme 1-3.** Propagation Patterns in Ethylene + Styrene Copolymerizations for a Second-Order Markovian Statistical Model..... 40
- Scheme 1-4.** Proposed Mechanism for Styrene Insertion Regiochemistry..... 58
- Scheme 1-5.** Possible Styrene Insertion Pathways during Chain Initiation..... 60
- Scheme 1-6.** Synthetic Route to Model Compound $\text{Ti}_2(\text{CH}_2\text{Ph})_4$ 67
- Scheme 1-7.** Pathways for Styrenic Comonomer Enchainment in Bimetallic Catalyst Mediated Ethylene Copolymerization..... 76

Chapter 2

- Scheme 2-1.** Synthesis of Isotactic Polypropylene-Metal Oxide Nanocomposites..... 93

List of Tables

Chapter 1

Table 1-1.	Ethylene + Styrene Copolymerization Results for Catalysts Ti₂ and Ti₁ with Cocatalyst B₁	46
Table 1-2.	Styrene Homopolymerization Results.....	57
Table 1-3.	Copolymerization of Ethylene and Styrene in C ₆ H ₅ Cl with Cocatalyst B₁	64
Table 1-4.	Summary of Crystal Structure Data for Ti₂(CH₂Ph)₄	70
Table 1-5.	Selected Bond Distances (Å) and Bond Angles (deg) for Ti₂(CH₂Ph)₄	71
Table 1-6.	Correlation between the Bimetallic Effect (Ti₂ vs Ti₁ Comonomer Enchainment Selectivity) and <i>ipso</i> Carbon Chemical Shift of the Styrenic Comonomers.....	78

Chapter 2

Table 2-1.	XRD Linewidth Analysis Results of the Nanocomposites.....	95
Table 2-2.	Electrical Characterization Results for Metal Oxide-polypropylene Nanocomposites.....	105

List of Charts

Chapter 1

Chart 1-1.	Structures of the Catalysts and Cocatalysts.....	20
Chart 1-2.	Structures of the Styrenic Comonomers.....	25

Chapter 2

Chart 2-1.	Structures of the Metallocene Catalysts and MAO.....	87
-------------------	--	----

List of Figures

Chapter 1

- Figure 1-1.** Fineman-Ross plot for $Ti_2 + B_1$ -mediated ethylene + styrene copolymerization, F = ethylene/styrene feed ratio, f = ethylene content in copolymer in mol%/styrene content in copolymer in mol%.....37
- Figure 1-2.** Fineman-Ross plot for $Ti_1 + B_1$ -mediated ethylene + styrene copolymerization, F = ethylene/styrene feed ratio, f = ethylene content in copolymer in mol%/styrene content in copolymer in mol%.....38
- Figure 1-3.** ^{13}C NMR spectrum (100 MHz, $C_2D_2Cl_4$, 130 °C) of poly(ethylene-*co*-styrene) showing spectral assignments in the backbone region..... 41
- Figure 1-4.** Triad distribution analysis plots for $Ti_2 + B_1$ -mediated ethylene + styrene copolymerization.....43
- Figure 1-5.** Triad distribution analysis plots for $Ti_1 + B_1$ -mediated ethylene + styrene copolymerization.....44
- Figure 1-6.** ^{13}C NMR spectra (100 MHz, $C_2D_2Cl_4$, 130 °C) of the poly(ethylene-*co*-styrene) samples from Table 1-1, entries 1-3 in which catalyst nuclearity and connectivity is varied.....47
- Figure 1-7.** ^{13}C NMR spectra (100 MHz, $C_2D_2Cl_4$, 130 °C) of the poly(ethylene-*co*-4-methylstyrene) samples from Table 1-1, entries 4-5 in which catalyst nuclearity is varied.....49
- Figure 1-8.** ^{13}C NMR spectra (100 MHz, $C_2D_2Cl_4$, 130 °C) of the poly(ethylene-*co*-4-fluorostyrene) samples from Table 1-1, entries 6-7, in which the catalyst nuclearity is varied.....50
- Figure 1-9.** ^{13}C NMR spectra (100 MHz, $C_2D_2Cl_4$, 130 °C) of the poly(ethylene-*co*-4-chlorostyrene) samples from Table 1-1, entries 8-9, in which the catalyst nuclearity is varied.....52
- Figure 1-10.** ^{13}C NMR spectra (100 MHz, $C_2D_2Cl_4$, 130 °C) of the poly(ethylene-*co*-4-bromostyrene) samples from Table 1-1, entries 10-11, in which the catalyst nuclearity is varied.....53
- Figure 1-11.** Representative ^{13}C NMR spectrum (100 MHz, $C_2D_2Cl_4$, 130 °C) of the polymeric product in ethylene + styrene copolymerization mediated by CGCZr⁺ catalysts..55

	14
Figure 1-12. ^{13}C NMR end group analysis (100 MHz, $\text{C}_2\text{D}_2\text{Cl}_4$, 130 °C) of the polystyrenes from Table 1-2, entries 2-3	61
Figure 1-13. ^{13}C NMR end group analysis (100 MHz, $\text{C}_2\text{D}_2\text{Cl}_4$, 130 °C) of the polystyrenes from Table 1-2, entries 6-8	62
Figure 1-14. ^{13}C NMR spectra (100 MHz, $\text{C}_2\text{D}_2\text{Cl}_4$, 130 °C) of two poly(ethylene- <i>co</i> -styrene) samples from Table 1-4	65
Figure 1-15. The molecular structure and atom numbering scheme for the model compound $\text{Ti}_2(\text{CH}_2\text{Ph})_4$. Thermal ellipsoids are drawn at the 30% probability level	72
Chapter 2	
Figure 2-1. ^{13}C NMR spectrum of an isotactic polypropylene nanocomposite (100 MHz, $\text{C}_2\text{D}_2\text{Cl}_4$, 130 °C)	94
Figure 2-2. ^{13}C NMR spectrum of a poly(ethylene- <i>co</i> -1-octene) nanocomposite (100 MHz, $\text{C}_2\text{D}_2\text{Cl}_4$, 130 °C)	97
Figure 2-3. ^{13}C NMR spectrum of a syndiotactic-polystyrene nanocomposite (100 MHz, $\text{C}_2\text{D}_2\text{Cl}_4$, 130 °C)	98
Figure 2-4. Electron microscopic characterization of: (a) as-received pristine ZrO_2 (SEM) and (b) 7.4 vol% ZrO_2 - <i>iso</i> PP nanocomposite (TEM)	100
Figure 2-5. Electron microscopic characterization of: (a) as-received pristine TZ3Y (SEM) and (b) 31.1 wt% TZ3Y- <i>iso</i> PP nanocomposite (TEM)	101
Figure 2-6. Electron microscopic characterization of: (a) as-received pristine TZ8Y (SEM) and (b) 39.2 wt% TZ8Y- <i>iso</i> PP nanocomposite (TEM)	102
Figure 2-7. Representative C (capacitance) vs. A (electrode area) plot for a 2.6 vol% BaTiO_3 - <i>iso</i> PP nanocomposite	103
Figure 2-8. Leakage current density vs. field measurement results for the nanocomposite MIS or MIM devices (legends are for the volume fraction of the inorganic particles): (a) n^+ -Si/ BaTiO_3 -polypropylene/Au; (b) n^+ -Si/ <i>sphere</i> - TiO_2 -polypropylene/Au; (c) Al/ <i>rod</i> - TiO_2 -polypropylene/Au	106
Figure 2-9. Leakage current density vs. field measurement results for the nanocomposite MIS or MIM devices (legends are for the volume fraction of the inorganic particles (a) Al/ ZrO_2 -polypropylene/Au; (b) Al/TZ3Y-polypropylene/Au; (c) Al/TZ8Y-polypropylene/Au	109

- Figure 2-10.** Normalized effective permittivity ($\epsilon_{eff} - \epsilon_b / \epsilon_a - \epsilon_b$) for composite dielectrics of polypropylene with spherical inclusions (eq. 4), and with ellipsoidal inclusions (eq. 5)..... 115
- Figure 2-11.** Comparison of effective permittivities for spherical- and rod-shaped TiO₂ nanoparticle-polypropylene nanocomposites.....116

Chapter 1

Bimetallic Effects in the Homopolymerization of Styrene and Copolymerization of Ethylene and Styrenic Comonomers. Scope, Kinetics, and Mechanism

Abstract

This chapter describes the homopolymerization of styrene and the copolymerization of ethylene and styrenic comonomers mediated by the single-site bimetallic “constrained geometry catalysts” (CGCs), $(\mu\text{-CH}_2\text{CH}_2\text{-3,3}')\{\eta^5\text{-indenyl}[1\text{-Me}_2\text{Si}(\text{tBuN})(\text{TiMe}_2)]_2$ [EBICGC(TiMe₂)₂; **Ti₂**], $(\mu\text{-CH}_2\text{CH}_2\text{-3,3}')\{\eta^5\text{-indenyl}[1\text{-Me}_2\text{Si}(\text{tBuN})(\text{TiMe}_2)]_2$ [EBICGC(ZrMe₂)₂; **Zr₂**], $(\mu\text{-CH}_2\text{-3,3}')\{\eta^5\text{-indenyl}[1\text{-Me}_2\text{Si}(\text{tBuN})(\text{TiMe}_2)]_2$ [MBICGC(TiMe₂)₂; **C1-Ti₂**], and $(\mu\text{-CH}_2\text{-3,3}')\{\eta^5\text{-indenyl}[1\text{-Me}_2\text{Si}(\text{tBuN})(\text{TiMe}_2)]_2$ [MBICGC(ZrMe₂)₂; **C1-Zr₂**], in combination with the borate activator/cocatalyst $\text{Ph}_3\text{C}^+\text{B}(\text{C}_6\text{F}_5)_4^-$ (**B₁**). Under identical styrene homopolymerization conditions, **C1-Ti₂ + B₁** and **Ti₂ + B₁** exhibit ~ 65 and ~ 35 times greater polymerization activities, respectively, than does monometallic $[1\text{-Me}_2\text{Si}(3\text{-ethylindenyl})(\text{tBuN})\text{TiMe}_2$ (**Ti₁**) + **B₁**. **C1-Zr₂ + B₁** and **Zr₂ + B₁** exhibit ~ 8 and ~ 4 times greater polymerization activities, respectively, than does the monometallic control $[1\text{-Me}_2\text{Si}(3\text{-ethylindenyl})(\text{tBuN})\text{ZrMe}_2$ (**Zr₁**) + **B₁**. NMR analyses show that the bimetallic catalysts suppress the regiochemical insertion selectivity exhibited by the monometallic analogues. In ethylene copolymerization, **Ti₂ + B₁** enchains 15.4% more styrene (**B**), 28.9% more 4-methylstyrene (**C**), 45.4% more 4-fluorostyrene (**D**), 41.2% more 4-chlorostyrene (**E**), and 31.0% more 4-bromostyrene (**F**) than does **Ti₁ + B₁**. This observed bimetallic chemoselectivity effect follows the same general trend as the electron density on the styrenic *ipso* carbon (**D** > **E** > **F** > **C** > **B**). Kinetic studies reveal that both **Ti₂ + B₁** and **Ti₁ + B₁**-mediated ethylene + styrene copolymerizations follow second-order Markovian statistics and tend to be alternating. Moreover, calculated reactivity ratios indicate that **Ti₂ + B₁** favors styrene insertion more than does **Ti₁ + B₁**. All the organozirconium complexes (**C1-Zr₂**, **Zr₂**, and **Zr₁**) are found to be incompetent for ethylene + styrene copolymerization, yielding only mixtures of polyethylene and polystyrene. Model compound $(\mu\text{-CH}_2\text{CH}_2\text{-3,3}')\{\eta^5\text{-indenyl}[1\text{-Me}_2\text{Si}(\text{tBuN})(\text{TiMe}_2)]_2$

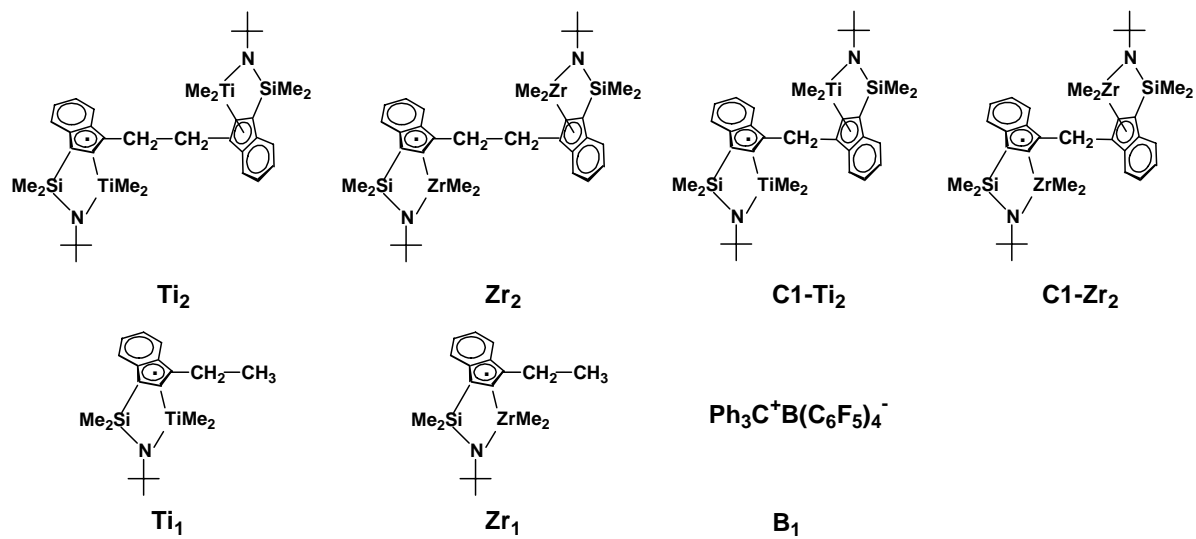
$\text{Me}_2\text{Si}(\text{tBuN})[\text{Ti}(\text{CH}_2\text{Ph})_2]\}_2$ {EBICGC[$\text{Ti}(\text{CH}_2\text{Ph})_2$] $_2$; $\text{Ti}_2(\text{CH}_2\text{Ph})_4$ } was designed, synthesized, and characterized. In situ activation studies with cocatalyst $\text{B}(\text{C}_6\text{F}_5)_3$ suggest an η^1 -coordination mode for the benzyl groups, thus supporting the proposed mechanism. For ethylene + styrene copolymerization, polar solvents are found to increase copolymerization activities and coproduce atactic polystyrene impurities in addition to ethylene-co-styrene, without diminishing the comonomer incorporation selectivity. Both homopolymerization and copolymerization results argue that substantial cooperative effects between catalytic sites are operative.

Introduction

Enzymes achieve superior reactivity and selectivity, in part due to their capability to create high local reagent concentrations and special, conformationally/dynamically advantaged active site–substrate proximities/interactions.¹ In this regard, intensive recent research efforts have focused on discovering unique/more efficient homogeneous catalytic processes benefiting from cooperative effects between adjacent active centers in multinuclear metal complexes.² For single-site olefin polymerization catalysts,³ we recently reported that $-\text{CH}_2\text{CH}_2-$ (**Ti₂**, **Zr₂**) and $-\text{CH}_2-$ (**C1-Ti₂**, **C1-Zr₂**) bridged bimetallic “constrained geometry catalysts” (CGCs)⁴ exhibit remarkable nuclearity effects in terms of chain branch formation, α -olefin comonomer enchainment selectivity, and molecular weight enhancement versus their mononuclear counterparts (**Ti₁**, **Zr₁**) (Chart 1-1).⁵ For ethylene copolymerizations, it was speculated that when the alkenyl region of the incoming comonomer binds to the first metal center, the second d^0 , highly electrophilic metal center can engage in secondary, possibly agostic interactions⁶ with sp^3 sites, leading to enhanced comonomer binding affinity/activating capacity (Scheme 1-1). Density functional theory (DFT/B3LYP) calculations reveal that this agostic interaction contributes ~ 2 kcal/mol stabilization to the coordinated bimetallic α -olefin complex.⁷ An intriguing question next arises as to whether these cooperative enchainment effects, facilitated by multinuclear catalysts, are more likely to mediate unusual polymerization patterns involving monomers with potentially stronger secondary coordinating moieties such as styrenes and dienes.

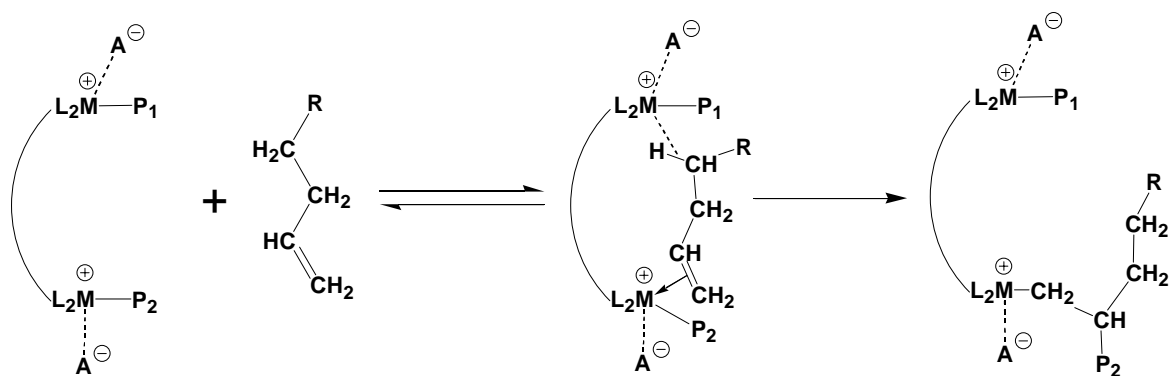
Over the past several decades, ethylene + styrene copolymers have received great attention due to their impressive viscoelastic behavior, mechanical properties, and compatibilities with a wide range of other polymeric materials, arising from the introduction of aromatic functional groups into the polyethylene backbone.⁸ Initial attempts to copolymerize ethylene and

Chart 1-1. Structures of the Catalysts and Cocatalysts.



Scheme 1-1. Proposed Mechanistic Scenario for Enhanced Comonomer Enchainment by

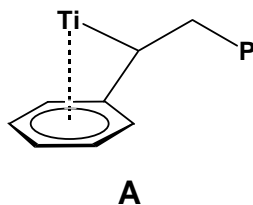
Bimetallic Catalysts



styrene via heterogeneous Ziegler-Natta processes proved largely unsuccessful, typically yielding homopolymer mixtures or copolymers with styrene incorporation < 1 mol%.⁹ The development of homogeneous single-site polymerization catalysts has led to a resurgence of interest in this field, however challenges remain.^{10,11,12} For Cp'TiXYZ-type catalysts¹⁰ (Cp' = substituted or unsubstituted η^5 -cyclopentadienyl, indenyl, fluorenyl; X, Y, Z = halogen, alkyl, alkoxy, aryloxy, ketimide, etc. ligand), substantial quantities of homopolymer contaminants are coproduced in addition to ethylene + styrene copolymers, likely due to multiple active species, and in certain cases, the presence of excess cocatalyst. *Ansa*-amido-monocyclopentadienyl Ti CGC catalysts represent another major advance in this field, producing ethylene + styrene copolymers exclusively; however styrene incorporation is invariably < 50 mol%, regardless of the styrene : ethylene feed ratio. The copolymer obtained is described as “pseudo-random”, since no head-to-tail styrene coupling is detected, even at relatively high levels of styrene incorporation.¹²

As a common, indispensable commodity plastic, polystyrene has also attracted extensive research efforts. Isotactic polystyrene was first synthesized by heterogeneous Ziegler-Natta catalysis¹³ and was recently synthesized by homogeneous catalysis.^{14,15} Thus, Cp'TiXYZ-type metallocene catalysts (Cp' = substituted or unsubstituted η^5 -cyclopentadienyl, indenyl, fluorenyl; X, Y, Z = halogen, alkyl, alkoxy, aryloxy, etc. ligand),¹⁶ and some other metallocene^{11b,17} and non-metallocene¹⁸ catalysts are known to afford syndiotactic polystyrene, however, the nature of the catalytically-active species and the mechanism of stereocontrol have not been unambiguously established. Mononuclear CGCTi⁺ catalysts exhibit marginal activity in styrene homopolymerization,^{5e,12h} which is thought due to catalyst deactivation via arene “back-biting”

coordination¹⁹ in the 2,1-insertion product (**A**). It would therefore be desirable to have a generalizable catalyst type, which, by tuning the symmetry of the ancillary ligand structure,

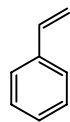


could afford polystyrene products with efficient productivity and predetermined stereochemistry.

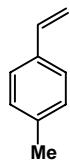
In a preliminary investigation,^{5c} we briefly communicated that **Ti₂** not only exhibits far greater activity for styrene homopolymerizations than does **Ti₁**, and installs unusual 1,2-insertion regiochemistry²⁰ (up to ~ 50%) in the initiation steps, but affords broad-range controllable styrene incorporation (0-76% at 20 °C, 1.0 atm ethylene pressure) in ethylene + styrene copolymerizations, arguing that multinuclear cooperative catalysis indeed mediates unusual styrene polymerization patterns, although neither the scope, kinetics, nor mechanism were defined. In the present contribution, we investigate ethylene and styrene reactivity ratios for both **Ti₂** and **Ti₁**-mediated copolymerizations, and extend comparative copolymerization studies to a selected variety of substituted styrenic comonomers (Chart 1-2) and to organozirconium CGC catalysts (**C1-Zr₂**, **Zr₂**, and **Zr₁**) in order to fully characterize the scope and mechanism of this bimetallic effect. We also investigate the influence of metal-metal distance on these bimetallic cooperative effects in styrene homopolymerization and ethylene + styrene copolymerizations by comparing the properties of the methylene-bridged bimetallic catalysts **C1-Ti₂** and **C1-Zr₂** to the ethylene-bridged bimetallic variants **Ti₂** and **Zr₂**. In addition, model compound (μ -CH₂CH₂-3,3') $\{(\eta^5$ -indenyl)[1-Me₂Si('BuN)][Ti(CH₂Ph)₂]₂ [**Ti₂(CH₂Ph)₄**] was designed, synthesized, characterized, and activated with the cocatalyst/activator B(C₆F₅)₃ to probe structural aspects of the proposed mechanism for the observed bimetallic enchainment effects.

Previously, it was reported that polar solvents can depress bimetallic effects in ethylene copolymerization by weakening/supplanting mechanistically important agostic interactions.^{5a,b} In the present study, we carry out detailed ethylene + styrene copolymerizations in the same polar solvent to determine whether such medium effects can weaken/displace the metal-arene interactions. It will be seen that, by manipulating the achievable metal-metal distances, styrenic comonomer substituents (**B-F**), and polymerization medium, the observed bimetallic effects can be varied dramatically.

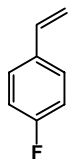
Chart 1-2. Structures of the Styrenic Comonomers.



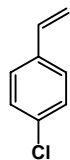
B



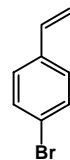
C



D



E



F

Experimental Section

Materials and Methods. All manipulations of air-sensitive materials were performed with rigorous exclusion of oxygen and moisture in flamed Schlenk-type glassware on a dual-manifold Schlenk line or interfaced to a high-vacuum line (10^{-5} Torr), or in a dinitrogen-filled Vacuum Atmospheres glove box with a high capacity recirculator (<1 ppm O_2). Argon (Matheson or Airgas, prepurified) and ethylene (Matheson or Airgas, polymerization grade) were purified by passage through a supported MnO oxygen-removal column and an activated Davison 4A molecular sieve column. Hydrocarbon solvents (toluene and pentane) were dried using an activated alumina column and Q-5 columns according to the method described by Grubbs,²¹ and were additionally vacuum transferred from Na/K alloy and stored in Teflon-valve sealed bulbs for polymerization experiments. Ether solvents (THF and Et_2O) were distilled under nitrogen from sodium benzophenone ketyl. The solvent 1,2-difluorobenzene was distilled from CaH_2 and stored over freshly activated Davison 4A molecular sieves. Deuterated solvents were purchased from Cambridge Isotope Laboratories (all ≥ 99 atom % D). Methylene chloride- d_2 was dried over CaH_2 and vacuum-transferred into J. Young NMR tubes. The solvent for polymer NMR characterization, 1,1,2,2-tetrachloroethane- d_2 , was used as received. Other deuterated solvents were distilled from Na/K alloy and stored in vacuum-tight storage tubes over freshly activated Davison 4A molecular sieves. Chlorobenzene, styrene, 4-chlorostyrene, 3-chlorostyrene, 4-methylstyrene, 4-fluorostyrene, 4-trifluoromethylstyrene (Aldrich) were dried sequentially for a week over CaH_2 and then triisobutylaluminum, and were freshly vacuum-transferred prior to polymerization experiments. The reagent $TMSCl$ was purchased from Aldrich and redistilled. The reagent $PhCH_2MgCl \cdot 0.66Et_2O$ was prepared by removing all the volatiles from $PhCH_2MgCl$ (1.0 M in Et_2O) (Aldrich). The reagent $(\mu-CH_2CH_2-3,3')\{\eta^5\text{-indenyl}\}[1-$

$\text{Me}_2\text{Si}(\text{tBuN})[\text{Ti}(\text{NMe}_2)_2]_2$ {EBICGC[$\text{Ti}(\text{NMe}_2)_2$] $_2$; $\text{Ti}_2(\text{NMe}_2)_4$ }, and the catalysts Ti_1 , Ti_2 , C1-Ti_2 , Zr_1 , Zr_2 , and C1-Zr_2 were prepared and purified according to literature procedures.^{5a,b}

Physical and Analytical Measurements. NMR spectra were recorded on a Varian Innova 400 (FT 400 MHz, ^1H ; 100 MHz, ^{13}C), Unity- or Mercury-400 (FT, 400 MHz, ^1H ; 100 MHz, ^{13}C), or Inova-500 (FT, 500 MHz, ^1H ; 125 MHz, ^{13}C) spectrometer. Chemical shifts (δ) for ^1H and ^{13}C spectra were referenced using internal solvent resonances and are reported relative to tetramethylsilane. NMR experiments on air-sensitive samples were conducted in Teflon valve-sealed sample tubes (J. Young). ^{13}C NMR assays of polymer microstructure were conducted in 1,1,2,2-tetrachloroethane- d_2 containing 0.05 M Cr(acac) $_3$ (as a relaxation reagent) at 130 °C. Resonances were assigned according to the literature for polystyrene and ethylene + styrene copolymers. Elemental analyses were performed by Midwest Microlabs, LLC, Indianapolis, Indiana.

Gel permeation chromatographic (GPC) analysis was carried out on a Waters Alliance GPCV 2000 high-temperature instrument equipped with three Polymer Laboratories 10 μm mixed B columns (three columns: Waters Styragel HT 6E, HT 4, HT 2) operating at 150 °C and a refractive index detector. A flow rate of 1.0 mL/min was used, and HPLC grade 1,2,4-trichlorobenzene was employed as the eluent. Typically, ca. 5 mg of the sample was dissolved in 7.0 mL of TCB. The hot solutions were filtered using a 0.5 μm stainless steel filter. A polystyrene relative calibration was carried out using narrow molecular weight distribution polystyrene standards from Polymer Laboratories with Ionol (4-(2,6,6-trimethyl-2-cyclohexen-1-yl)-3-buten-2-ol) added as the flow marker.²¹ Alternatively, GPC measurements were performed on a Polymer Laboratories PL-GPC 220 instrument using 1,2,4-trichlorobenzene solvent

(stabilized with 125 ppm BHT) at 150 °C. A set of three PLgel 10 μm mixed columns was used. Samples were prepared at 160 °C. Molecular weights were determined by GPC using narrow polystyrene standards and are not corrected.

Polymer glass transition temperatures and melting temperatures were measured on a TA Instruments 2920 Modulated Differential Scanning Calorimeter. Typically, ca. 10 mg samples were examined, and a ramp rate of 10 °C/min was used to measure the polymer glass transition points and melting points. To erase thermal history effects, all samples were run through at least two melt-freeze cycles. The data from the second melt-freeze cycle are presented here.

Styrene Homopolymerization Experiments in Toluene. In the glovebox, a 250 mL round-bottom three-neck Morton flask, which had been dried at 160 °C overnight and equipped with a large magnetic stirring bar and a thermocouple probe, was charged with 25 mL dry toluene and 5 mL dry styrene. The flask was then attached to a high-vacuum line (10^{-5} Torr) and equilibrated at the desired reaction temperature using an external bath. The catalytically-active species was freshly generated in 1.5 mL of dry 1,2-difluorobenzene in the nitrogen-filled glovebox. Under 1.0 atm of rigorously purified argon (pressure control using a mercury bubbler), the catalyst solution was quickly injected into the rapidly stirred flask using a gas-tight syringe equipped with a flattened spraying needle. After a measured time interval, the polymerization was quenched by the addition of 5 mL methanol, and the reaction mixture was then poured into 800 mL of methanol. The polymer was allowed to fully precipitate overnight and then collected by filtration, washed with fresh methanol, and dried on a high-vacuum line overnight to constant weight.

Ethylene Copolymerization Experiments in Toluene. In the glovebox, a 250 mL round-bottom three-neck Morton flask, which had been dried at 160 °C overnight and equipped with a large magnetic stirring bar and a thermocouple probe, was charged with 50 mL dry toluene and 10 mL dry styrene. The flask was then attached to a high-vacuum line (10^{-5} Torr), freeze-pump-thaw degassed, pre-saturated with 1.0 atm (pressure control using a mercury bubbler) of rigorously purified ethylene, and equilibrated at the desired reaction temperature using an external bath. The catalytically-active species was freshly generated in 1.5 mL of dry 1,2-difluorobenzene in the nitrogen-filled glovebox. The catalyst solution was then quickly injected into the rapidly stirred flask using a gas-tight syringe equipped with a flattened spraying needle. After a measured time interval, the polymerization was quenched by the addition of 5 mL methanol, and the reaction mixture was then poured into 800 mL of methanol. The polymer was allowed to fully precipitate overnight and then collected by filtration, washed with fresh methanol, and dried on a high vacuum line overnight to constant weight.

Ethylene Copolymerization Experiments in Chlorobenzene. In the glovebox, a 250 mL round-bottom three-neck Morton flask, which had been dried at 160 °C overnight and equipped with a large magnetic stirring bar and a thermocouple probe, was charged with 10 mL dry styrene. The flask was then attached to a high-vacuum line (10^{-5} Torr), freeze-pump-thaw degassed, and then 50 mL chlorobenzene was vacuum transferred in. The flask was pre-saturated with 1.0 atm (pressure control using a mercury bubbler) of rigorously purified ethylene, and equilibrated at the desired reaction temperature using an external bath. The catalytically-active species was freshly generated in 1.5 mL of dry 1,2-difluorobenzene in the nitrogen-filled glovebox. The catalyst solution was then quickly injected into the rapidly stirred flask using a

gas-tight syringe equipped with a flattened spraying needle. After a measured time interval, the polymerization was quenched by the addition of 5 mL methanol, and the reaction mixture was then poured into 800 mL of methanol. The polymer was allowed to fully precipitate overnight and then collected by filtration, washed with fresh methanol, and dried on a high-vacuum line overnight at 80 °C.

Determination of Comonomer Content by ^1H NMR. The solvent 1,1,2,2-tetrachloroethane- d_2 ($\text{C}_2\text{D}_2\text{Cl}_4$) was used as the deuterated solvent for polymer NMR analysis because its NMR spectral features do not overlap with any of the polymer resonances. Delay times of 20s were used to ensure the accuracy of NMR peak integration. The comonomer contents were calculated based on the integral of the aromatic region (A_{aromatic}) and the aliphatic region ($A_{\text{aliphatic}}$) according to the following equations:

$$\text{poly(ethylene-}i>co\text{-styrene)} \quad S\% = \frac{4A_{\text{aromatic}}}{A_{\text{aromatic}} + 5A_{\text{aliphatic}}}$$

$$\text{poly(ethylene-}i>co\text{-4-halostyrene)} \quad S\% = \frac{4A_{\text{aromatic}}}{A_{\text{aromatic}} + 4A_{\text{aliphatic}}}$$

$$\text{poly(ethylene-}i>co\text{-4-methylstyrene)} \quad S\% = \frac{2A_{\text{aromatic}}}{2A_{\text{aliphatic}} - A_{\text{aromatic}}}$$

Solvent Fractionation of Ethylene- co -styrene and Polystyrene Mixtures. A known amount of polymer mixture was loaded into a cellulose fiber thimble placed inside a Soxhlet extractor. Methyl ethyl ketone (MEK) was used as the solvent to extract the polystyrene. After 24 h of refluxing, the remaining insoluble copolymer was carefully collected and dried on a high vacuum line overnight at 80 °C.

Synthesis of Bimetallic Metallocene Complex Ti_2Cl_4 . The reagent $\text{Ti}_2(\text{NMe}_2)_4$ (500 mg, 0.638 mmol) was partially dissolved in 75 mL dry toluene in a 100 mL Schlenk flask and the solution was cooled down to $-78\text{ }^\circ\text{C}$. Next, Me_3SiCl (3.0 mL, 23.64 mmol) was added dropwise by syringe with stirring. The solution was then allowed to slowly warm to room temperature and to stir for 48 h. Large quantities of wine-red solids precipitated, which were separated by filtration, washed with fresh pentane, and subsequently dried on the high-vacuum line. Yield: 370 mg (77%). This product was used for the next reaction without further purification. ^1H NMR (C_6D_6 , $23\text{ }^\circ\text{C}$, 499.748 MHz): δ 7.58 (d, 2H, $^3\text{J}_{\text{H-H}} = 8.5\text{ Hz}$, Ind, C_6H_4), 7.36 (d, 2H, $^3\text{J}_{\text{H-H}} = 8.5\text{ Hz}$, Ind, C_6H_4), 7.04 (t, 2H, $^3\text{J}_{\text{H-H}} = 7.5\text{ Hz}$, Ind, C_6H_4), 6.94 (t, 2H, $^3\text{J}_{\text{H-H}} = 8.0\text{ Hz}$, Ind, C_6H_4), 6.25 (s, 2H, Ind, C_5H), 3.59 (dd, 2H, $^2\text{J}_{\text{H-H}} = 14.5\text{ Hz}$, $^3\text{J}_{\text{H-H}} = 8.5\text{ Hz}$, CH_2CH_2), 3.25 (dd, 2H, $^2\text{J}_{\text{H-H}} = 14.0\text{ Hz}$, $^3\text{J}_{\text{H-H}} = 8.0\text{ Hz}$, CH_2CH_2), 1.31 (s, 18H, NCMe_3), 0.53 (s, 6H, SiMe_2), 0.28 (s, 6H, SiMe_2). Anal. Calcd for $\text{C}_{32}\text{H}_{44}\text{N}_2\text{Si}_2\text{Cl}_4\text{Ti}_2$: C, 51.21; H, 5.92; N, 3.73. Found: C, 51.14; H, 5.84; N, 3.98.

Synthesis of Bimetallic Metallocene Complex $\text{Ti}_2(\text{CH}_2\text{Ph})_4$. Ti_2Cl_4 (150 mg, 0.200 mmol) was suspended in 75 mL dry toluene in a 100 mL Schlenk flask, and after the mixture was cooled to $-78\text{ }^\circ\text{C}$, $\text{PhCH}_2\text{MgCl}\cdot 0.66\text{Et}_2\text{O}$ (153 mg, 0.764 mmol) dissolved in 10 mL dry toluene was added dropwise by syringe with stirring. The reaction mixture was then allowed to warm to room temperature and stirring continued for 24 h. Next, the MgCl_2 precipitate was filtered off, and the red filtrate was condensed to saturation and slowly cooled to $-40\text{ }^\circ\text{C}$ to afford red crystals, which were isolated by filtration, washed with cold pentane twice, and subsequently dried on the high-vacuum line. Yield: 80 mg (41%). Spectropic and analytical data are: ^1H NMR (C_6D_6 , $23\text{ }^\circ\text{C}$, 499.748 MHz): δ 7.66 (d, 2H, $^3\text{J}_{\text{H-H}} = 8.5\text{ Hz}$, Ind, C_6H_4), 7.54 (d, 2H, $^3\text{J}_{\text{H-H}} = 8.5\text{ Hz}$, Ind, C_6H_4), 7.40-6.70 (m, Ind + TiCH_2Ph), 5.75 (s, 2H, Ind, C_5H), 3.49 (dd, 2H, $^2\text{J}_{\text{H-H}} = 14.0\text{ Hz}$, $^3\text{J}_{\text{H-H}} = 6.2$

Hz, CH_2CH_2), 3.34 (dd, 2H, $^2J_{\text{H-H}} = 14.0$ Hz, $^3J_{\text{H-H}} = 6.2$ Hz, CH_2CH_2), , 3.18 (d, 2H, $^2J_{\text{H-H}} = 10.0$ Hz, TiCH_2Ph), 2.05 (d, 2H, $^2J_{\text{H-H}} = 10.0$ Hz, TiCH_2Ph), 1.83 (d, 2H, $^2J_{\text{H-H}} = 10.5$ Hz, TiCH_2Ph), 1.49 (s, 18H, NCMe_3), 0.61 (s, 6H, SiMe_2), 0.27 (s, 6H, SiMe_2), 0.20 (d, 2H, $^2J_{\text{H-H}} = 10.0$ Hz, TiCH_2Ph). ^1H NMR (CD_2Cl_2 , 23 °C, 499.748 MHz): δ 7.83 (d, 2H, $^3J_{\text{H-H}} = 8.5$ Hz, Ind, C_6H_4), 7.60 (d, 2H, $^3J_{\text{H-H}} = 8.0$ Hz, Ind, C_6H_4), 7.52 (t, 2H, $^3J_{\text{H-H}} = 7.0$ Hz, Ind, C_6H_4), 7.18 (t, 2H, $^3J_{\text{H-H}} = 7.5$ Hz, Ind, C_6H_4), 7.025 (t, 4H, $^3J_{\text{H-H}} = 7.8$ Hz, *m*-Ph), 7.022 (t, 4H, $^3J_{\text{H-H}} = 7.5$ Hz, *m*-Ph), 6.79 (t, 4H, $^3J_{\text{H-H}} = 7.5$ Hz, *p*-Ph), 6.76 (t, 4H, $^3J_{\text{H-H}} = 7.8$ Hz, *p*-Ph), 6.71 (d, 2H, $^3J_{\text{H-H}} = 7.0$ Hz, *o*-Ph), 6.62 (d, 2H, $^3J_{\text{H-H}} = 7.0$ Hz, *o*-Ph), 5.50 (s, 2H, Ind, C_5H), 3.33 (dd, 2H, $^2J_{\text{H-H}} = 8.0$ Hz, $^3J_{\text{H-H}} = 3.5$ Hz, CH_2CH_2), 3.26 (dd, 2H, $^2J_{\text{H-H}} = 7.5$ Hz, $^3J_{\text{H-H}} = 4.0$ Hz, CH_2CH_2), 2.80 (d, 2H, $^2J_{\text{H-H}} = 10.5$ Hz, TiCH_2Ph), 1.75 (d, 2H, $^2J_{\text{H-H}} = 10.0$ Hz, TiCH_2Ph), 1.64 (2H, TiCH_2Ph , overlapping with NCMe_3), 1.62 (s, 18H, NCMe_3), 0.80 (s, 6H, SiMe_2), 0.18 (s, 6H, SiMe_2), -0.23 (d, 2H, $^2J_{\text{H-H}} = 10.5$ Hz, TiCH_2Ph). $^{13}\text{C}\{^1\text{H}\}$ NMR (CD_2Cl_2 , 23 °C, 125.674 MHz): δ 150.09 (*ipso*- TiCH_2Ph), 146.58 (*ipso*- TiCH_2Ph), 134.56 (*Ind*), 133.25 (*Ind*), 131.27 (*Ind*), 129.51 (*Ind*), 129.02 (*ortho*- TiCH_2Ph), 128.70 (*ortho*- TiCH_2Ph), 128.27 (*meta*- TiCH_2Ph), 128.11 (*Ind*), 127.03 (*meta*- TiCH_2Ph), 126.72 (*Ind*), 125.90 (*Ind*), 123.99 (*Ind*), 122.76 (*para*- TiCH_2Ph), 122.06 (*para*- TiCH_2Ph), 94.34 (*Ind*), 84.90 (TiCH_2Ph), 80.23 (TiCH_2Ph), 61.28 (NCMe_3), 34.46 (NCMe_3), 30.12 (CH_2CH_2), 4.46 (SiMe_2), 1.26 (SiMe_2). Anal. Calcd for $\text{C}_{60}\text{H}_{72}\text{N}_2\text{Si}_2\text{Ti}_2$: C, 74.04; H, 7.47; N, 2.88. Found: C, 74.80; H, 7.47; N, 2.90.

In Situ NMR Study of the Bimetallic Metallocene Ion Pair $[\text{Ti}_2(\text{CH}_2\text{Ph})_2]^{2+}[\text{CH}_2\text{PhB}(\text{C}_6\text{F}_5)_3]^-$

12. In the glove box, $\text{Ti}_2(\text{CH}_2\text{Ph})_4$ and $\text{B}(\text{C}_6\text{F}_5)_3$ in a 1:2 molar ratio were loaded into a J. Young NMR tube. The sealed tube was then removed from the glovebox, attached to the vacuum line, cooled to -78 °C, and CD_2Cl_2 was immediately transferred in. The sample was shaken vigorously

and transferred directly to the NMR spectrometer. Upon activation, the solution color changed from red to dark brown. ^1H NMR (C_6D_6 , 23 °C, 499.748 MHz): δ 7.60-6.20 (m, Ind + $\text{Ti}^+\text{CH}_2\text{Ph}$ + $\text{B}^-\text{CH}_2\text{Ph}$), 5.68 (s, 2H, Ind, C_5H), 3.62 (br, 4H, $\text{B}^-\text{CH}_2\text{Ph}$), 2.91 (d, 2H, $^2\text{J}_{\text{H-H}} = 8.5$ Hz, $\text{Ti}^+\text{CH}_2\text{Ph}$), 2.43 (d, 2H, $^2\text{J}_{\text{H-H}} = 7.5$ Hz, $\text{Ti}^+\text{CH}_2\text{Ph}$), 1.05 (s, 18H, NMe_3), 0.26 (s, 6H, SiMe_2), 0.10 (s, 6H, SiMe_2).

X-ray Crystal Structure Determination of $\text{Ti}_2(\text{CH}_2\text{Ph})_4$. Crystals of the title complex suitable for X-ray diffraction were obtained by slow diffusion of pentane into a saturated toluene solution at room temperature. Inside the glovebox, the crystals were placed on a glass slide and covered with dry Infineum V8512 oil. The crystals were then removed from the box, and a suitable crystal was selected under a microscope using plane-polarized light. The crystal was mounted on a glass fiber and transferred to a Bruker SMART 1000 CCD area detector diffractometer in a nitrogen cold stream at 153 (2) K. Diffraction data were obtained with a finefocus, sealed tube Mo $\text{K}\alpha$ radiation source ($\lambda = 0.71073$ Å) and a graphite monochromator. Twenty frames (20 s exposures, 0.3° slices) were collected in three areas of space to determine the orientation matrix. The parameters for data collection were determined by the peak intensities and widths from the 60 frames used to determine the orientation matrix. The faces of the crystal were then indexed and data collection was begun. After data collection, the frames were integrated, the initial crystal structure was solved by direct methods, the structure solution was refined through successive least-squares cycles and subjected to a face-indexed absorption correction. Crystal data, data collection, and refinement parameters are summarized in Table 1-4 and in the Crystallographic Information File (CIF, see Supporting Information).

Results

The goal of this study was to investigate the scope, kinetics, and mechanism of bimetallic enchainment cooperative effects in styrene homopolymerization and ethylene + styrene copolymerizations. Previously, we briefly communicated evidence for such bimetallic effects in the case of Ti_2 , manifested by significantly greater activity in styrene homopolymerization and enhanced comonomer incorporation in ethylene + styrene copolymerization. In this contribution, we extend the study to include organozirconium catalysts and broaden the copolymerization scope to include a variety of informative styrenic comonomers. We also design, synthesize, and characterize a bimetallic model compound to probe the coordination mode of inserted styrene to the coordinatively open and highly electrophilic single-site catalytic center. After a brief discussion of the kinetics of Ti_2 - and Ti_1 -mediated ethylene + styrene copolymerization, we discuss the effects of styrene substituents on the comonomer incorporation difference between Ti_2 and Ti_1 . Next, styrene homopolymerization will be addressed in terms of polymerization activity and insertion regiochemistry. Finally, the effect of polar solvation on the bimetallic cooperative effects is discussed.

I. Kinetic Analyses of Ethylene + Styrene Copolymerization Mediated by $\text{Ti}_2 + \text{B}_1$ and $\text{Ti}_1 + \text{B}_1$.

Previously, we reported that under identical copolymerization conditions, the catalytic system $\text{Ti}_2 + \text{B}_1$ incorporates significantly more styrene into the polyethylene backbone than does $\text{Ti}_1 + \text{B}_1$. To understand this bimetallic effect on the selectivity of monomer enchainment, kinetic analyses were carried out to determine the reactivity ratios for both monomers. A series of ethylene + styrene copolymerizations were carried out with increasing styrene : ethylene feed

ratios for both $\mathbf{Ti}_2 + \mathbf{B}_1$ and $\mathbf{Ti}_1 + \mathbf{B}_1$ -mediated copolymerizations. All the copolymerization experiments were terminated at low styrene conversions ($< 10\%$) to ensure a constant feed ratio.

First-Order Markovian Analysis. In a first-order Markovian model for ethylene + styrene copolymerization statistics, which takes into account only the influence of the last inserted monomer during chain propagation,^{23a} the reactivity ratios r_E and r_S are defined as the ratios of homopropagation rate constants to crosspropagation rate constants of ethylene and styrene, respectively ($r_E = k_{EE}/k_{ES}$, $r_S = k_{SS}/k_{SE}$, Scheme 1-2). With styrene content in the monomer feed and in the copolymer known, the reactivity ratios can be obtained from Fineman-Ross plots (Figures 1-1 and 1-2).^{23a} For $\mathbf{Ti}_2 + \mathbf{B}_1$ -mediated ethylene + styrene copolymerization, the slope and the intercept of the Fineman-Ross plot yield the values $r_E = 13.2 \pm 0.8$ and $r_S = 0.039 \pm 0.003$, respectively, while for $\mathbf{Ti}_1 + \mathbf{B}_1$, the Fineman-Ross plot gives the values $r_E = 14.5 \pm 1.0$ and $r_S = 0.014 \pm 0.003$. It can be seen that $\mathbf{Ti}_2 + \mathbf{B}_1$ possesses a significantly larger r_S and slightly smaller r_E than $\mathbf{Ti}_1 + \mathbf{B}_1$, in agreement with the NMR analytical observations that \mathbf{Ti}_2 always incorporates more styrene than \mathbf{Ti}_1 under identical reaction conditions.

Scheme 1-2. Propagation Patterns in Ethylene + Styrene Copolymerization for a First-Order Markovian Statistical Model

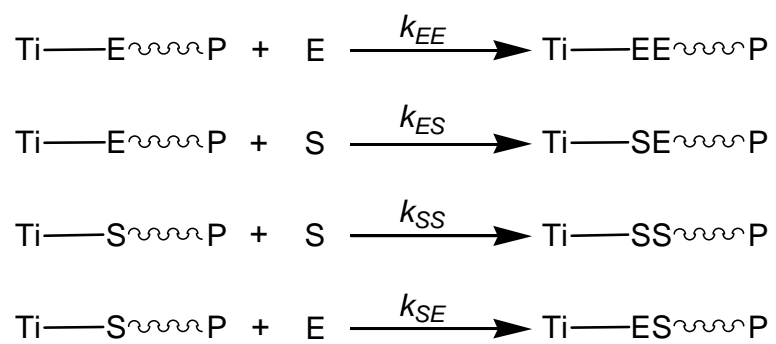


Figure 1-1. Fineman-Ross plot for $Ti_2 + B_1$ -mediated ethylene + styrene copolymerization, F = ethylene/styrene feed ratio, f = ethylene content in copolymer in mol%/styrene content in copolymer in mol%.

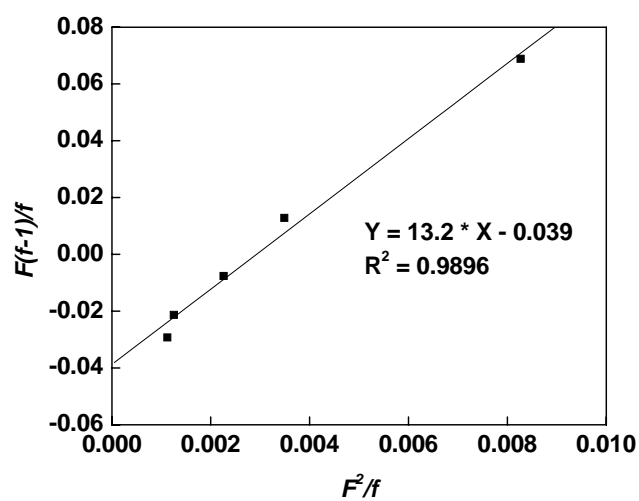
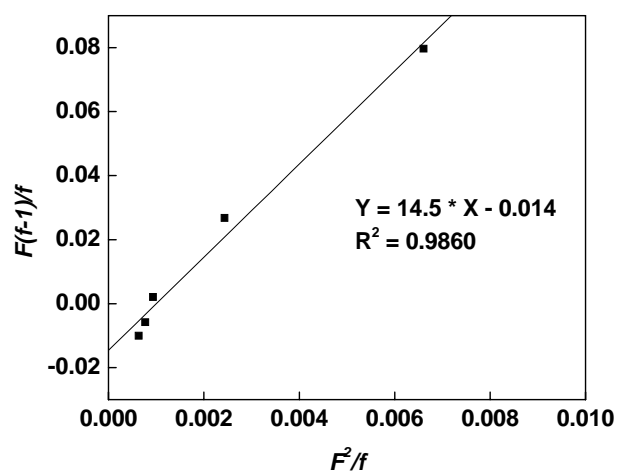


Figure 1-2. Fineman-Ross plot for $Ti_1 + B_1$ -mediated ethylene + styrene copolymerization, F = ethylene/styrene feed ratio, f = ethylene content in copolymer in mol%/styrene content in copolymer in mol%.



Second-Order Markovian Analysis. The second-order Markovian assumption takes into account the influence of the second-to-the-last inserted monomer unit on incoming monomer enchainment selectivity.^{23a} As shown in Scheme 1-3, when the last inserted monomer is ethylene, four different propagation equations can be written (eqs. 1-4). Dividing eq. 1 by eq. 2 and eq. 3 by eq. 4 yields eqs. 5 and 6, respectively, where X_E is the ethylene : styrene feed ratio. Two reactivity ratios are defined to quantify the preference of ethylene over styrene to be inserted into the Ti-polymeryl bond when the second-to-the-last inserted monomer is ethylene (r_E) or styrene (r'_E).^{23b} If r_E is inequivalent to r'_E , then the penultimate unit specifically exerts an effect on the incoming monomer enchainment selectivity. Figure 1-3 shows a typical ^{13}C NMR spectrum of an ethylene + styrene copolymer and its assignments (see more below), from which the triad distribution can be extracted (eqs. 7-9). As illustrated in Figure 1-4, for $\text{Ti}_2 + \text{B}_1$ -mediated ethylene + styrene copolymerization, plotting $[\text{EEE}]/[\text{EES}]$ and $[\text{SEE}]/[\text{SES}]$ vs X_E yields straight lines, the slopes of which afford the reactivity ratios defined above (eqs. 7 and 8). The

$$\frac{d[\text{EEE}]}{dt} = k_{EEE} [\text{Ti-EE-P}] [\text{E}] \quad (1)$$

$$\frac{d[\text{EES}]}{dt} = k_{EES} [\text{Ti-EE-P}] [\text{S}] \quad (2)$$

$$\frac{d[\text{SEE}]}{dt} = k_{SEE} [\text{Ti-ES-P}] [\text{E}] \quad (3)$$

$$\frac{d[\text{SES}]}{dt} = k_{SES} [\text{Ti-ES-P}] [\text{S}] \quad (4)$$

$$\frac{[\text{EEE}]}{[\text{EES}]} = \frac{k_{EEE} [\text{E}]}{k_{EES} [\text{S}]} = r_E X_E \quad (5)$$

$$\frac{[\text{SEE}]}{[\text{SES}]} = \frac{k_{SEE} [\text{E}]}{k_{SES} [\text{S}]} = r'_E X_E \quad (6)$$

Scheme 1-3. Propagation Patterns in Ethylene + Styrene Copolymerizations for a Second-Order Markovian Statistical Model

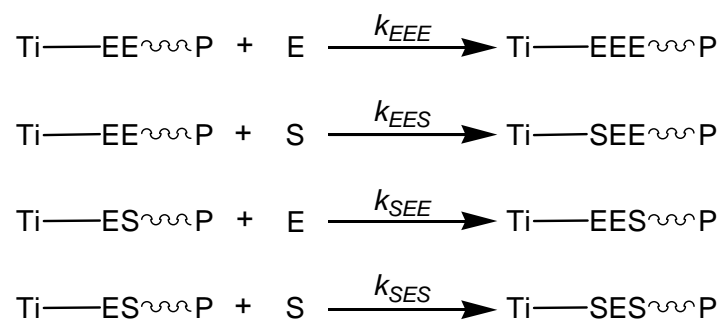
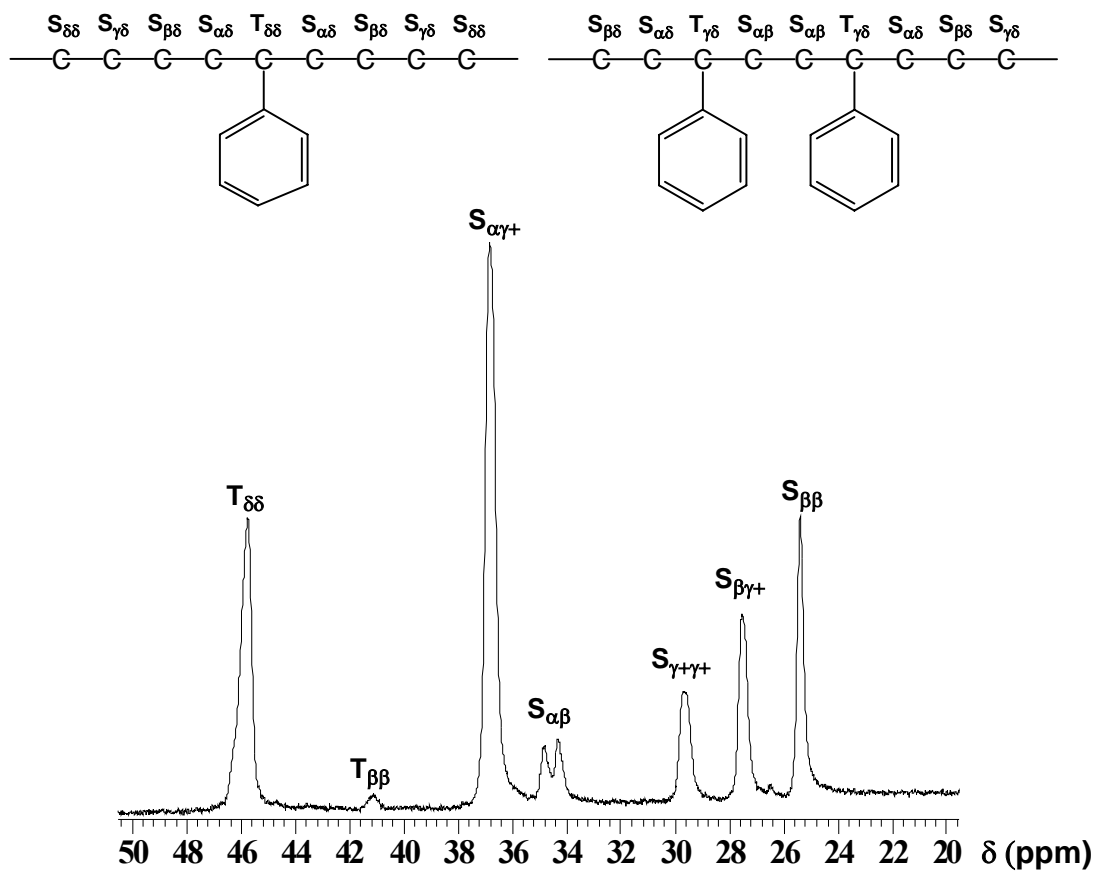


Figure 1-3. ^{13}C NMR spectrum (100 MHz, $\text{C}_2\text{D}_2\text{Cl}_4$, 130 $^\circ\text{C}$) of poly(ethylene-*co*-styrene) showing spectral assignments in the backbone region.



$$[EEE] \propto 0.5(S_{\gamma+\gamma+} - 0.5S_{\beta\gamma+}) \quad (7)$$

$$[SES] \propto S_{\beta\beta} \quad (8)$$

$$[SEE] = [EES] \propto 0.5S_{\beta\gamma+} \quad (9)$$

fact that r_E is larger than r'_E ($r_E = 7.79 \pm 1.02 > r'_E = 3.26 \pm 0.11$) indicates that the aforementioned bimetallic catalyst **Ti₂**-mediated ethylene + styrene copolymerization follows second-order Markovian statistics (penultimate model), and more interestingly, when the second-to-the-last inserted monomer is styrene and the last inserted one is ethylene, the incoming styrene is preferred over ethylene for insertion into the Ti-polymeryl bond, thereby generating SES triads. This alternating copolymerization trend is also evidenced by the product of the two reactivity ratios defined above by the first-order Markovian statistics ($r_E \times r_S = 0.51$).

For **Ti₁ + B₁** mediated ethylene + styrene copolymerization, reactivity ratios can also be obtained by plotting $[EEE]/[EES]$ and $[SEE]/[SES]$ vs X_E (Figure 1-5). Again, $r_E = 13.49 \pm 0.78$ is larger than $r'_E = 6.45 \pm 0.14$, suggesting that for the monometallic catalyst, **Ti₁**-mediated ethylene + styrene copolymerization follows second-order Markovian statistics as well. In addition, the values of both reactivity ratios for **Ti₂** are invariably smaller than the corresponding ones for **Ti₁**, demonstrating that **Ti₂** favors styrene insertion more than **Ti₁**, or in other words, **Ti₁** favors ethylene insertion more than **Ti₂**, which is in agreement to the observed bimetallic enchainment selectivity effects that under identical ethylene + styrene copolymerization conditions, bimetallic catalyst **Ti₂** incorporates styrene more efficiently than does monometallic catalyst **Ti₁**.

Figure 1-4. Triad distribution analysis plots for $Ti_2 + B_1$ -mediated ethylene + styrene copolymerization.

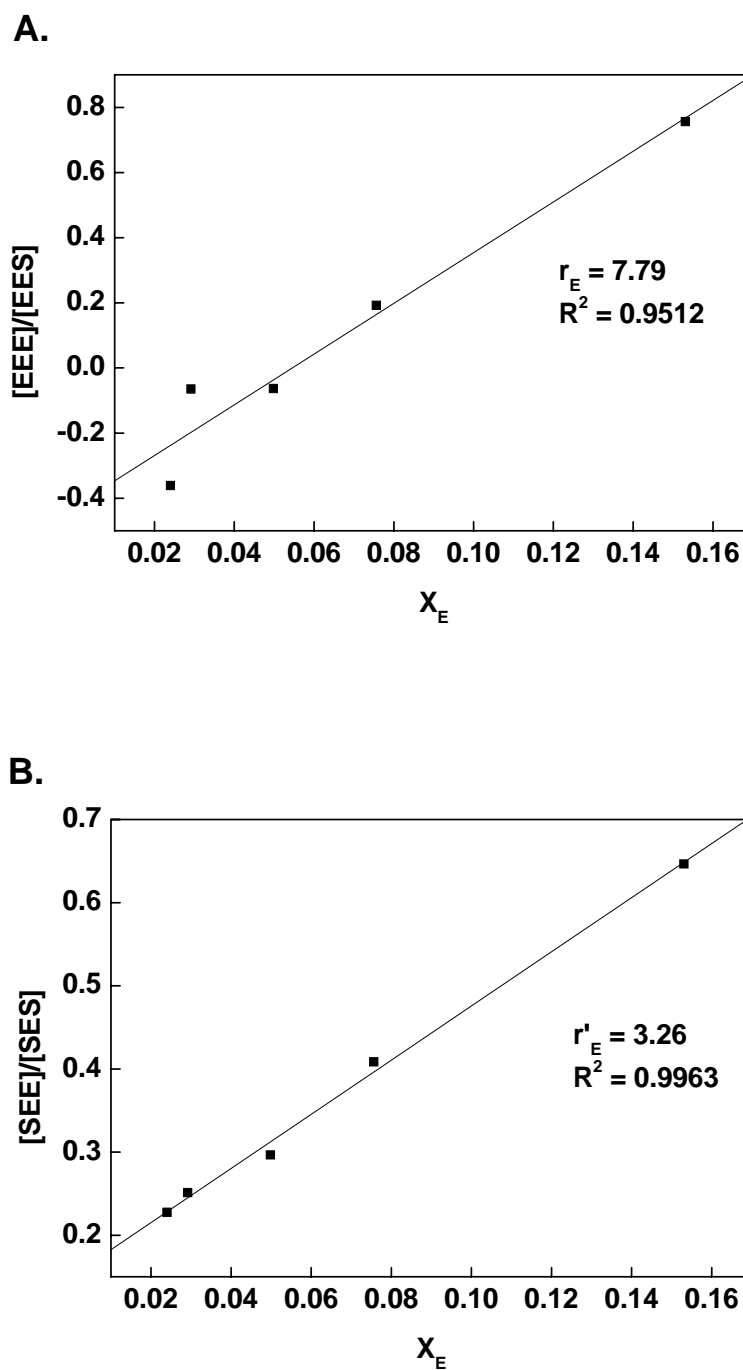
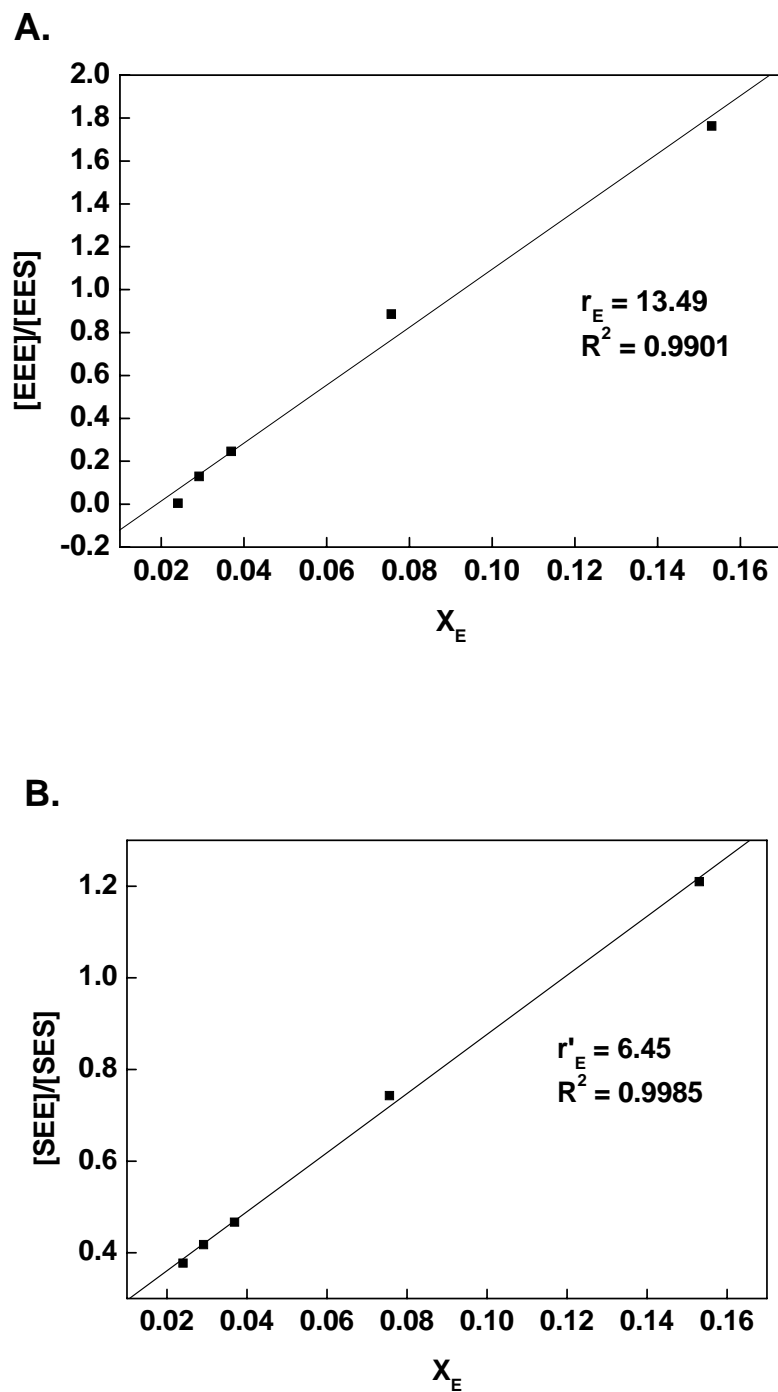


Figure 1-5. Triad distribution analysis plots for $Ti_1 + B_1$ -mediated ethylene + styrene copolymerization.



II. Copolymerization of Ethylene and Styrenic Comonomers.

Previously, we communicated that under identical copolymerization conditions, **Ti₂** incorporates significantly more styrene than does **Ti₁** in ethylene + styrene copolymerizations. To test the generality of this observed bimetallic effect, a variety of substituted styrenic comonomers with either electron-donating or electron-withdrawing substituents at the *para* positions were examined in copolymerization experiments with ethylene and the aforementioned organotitanium catalysts. For all of these styrenic comonomers, it will be seen that the bimetallic catalysts exhibit significantly enhanced comonomer enchainment selectivity versus the monometallic analogue under identical reaction conditions.

Copolymerization of Ethylene and Styrene

Figure 1-6 shows the ¹³C NMR spectra of the poly(ethylene-*co*-styrene) samples of Table 1-1, entries 1-3, and assignments made according to literature.¹⁰ The resonances at $\delta = 34.4$ and 34.9 ppm are attributed to $S_{\alpha\beta}$, which represents either a tail-to-tail coupled styrene dyad or an ethylene unit bridged head-to-head coupled styrene dyad. Other polymer resonances centered at $\delta = 25.5, 27.7, 29.8, 36.9,$ and 46.0 ppm in the aliphatic region can be assigned to $S_{\beta\beta}, S_{\beta\gamma+}, S_{\gamma+\gamma+}, S_{\alpha\gamma+},$ and $T_{\delta+\delta+}$, respectively, corresponding to SES, SEE, SEE_nS, SES + SEE, and E_nSE_n ($n \geq 1$) sequences, respectively.^{10g} The signals observed at $\delta = 146.4$ and 125.7 ppm in the aromatic region are assigned to the *ipso* carbon and *para* carbon of the phenyl ring attached to the copolymer backbone, respectively.

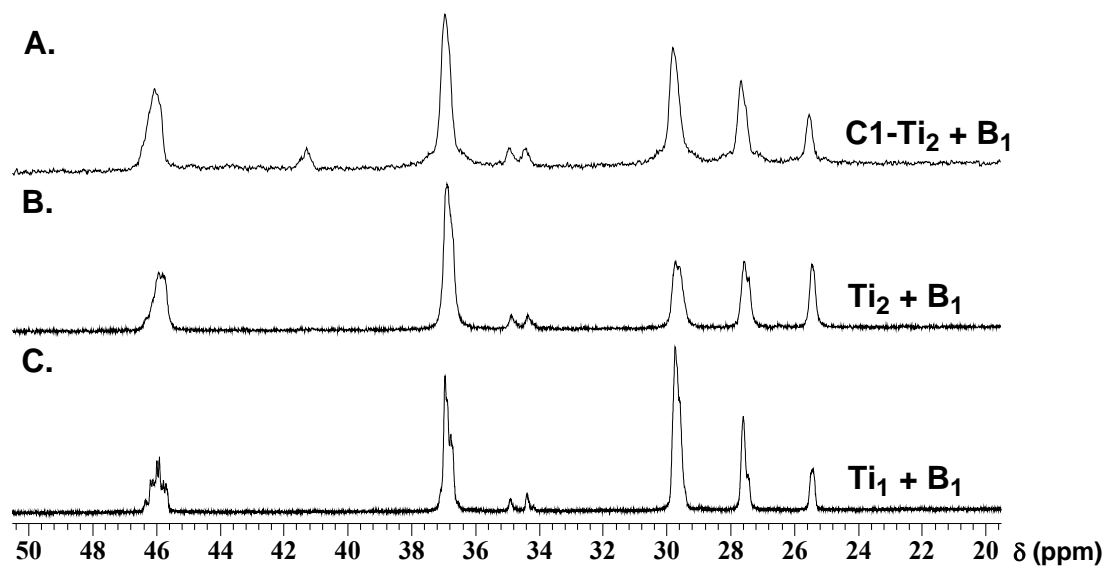
Regarding nuclearity effects, it is found that under strictly identical copolymerization conditions the **Ti₂ + B₁** combination incorporates 15.4% more styrene than the mononuclear analogue **Ti₁ + B₁** (Table 1-1, entry 2 versus entry 3). To further explore the correlation between catalyst structure and polymerization behavior, methylene-bridged **C1-Ti₂** was also employed in

Table 1-1. Ethylene + Styrene Copolymerization Results for Catalysts **Ti₂** and **Ti₁** with Cocatalyst **B₁**^a

Entry	Catalyst	Comonomer	Comonomer Concentration (M)	Activity ^b ($\times 10^6$)	T _g ^c (°C)	T _m ^c (°C)	M _w ^d ($\times 10^5$)	M _w /M _n ^d	Comonomer % ^e (mol %)
1	C1-Ti ₂	B	1.45	3.7	22.3	n. o. ^f	10.34	2.2	37.1
2	Ti ₂	B	1.45	5.8	21.7	n. o.	3.67	2.1	32.3
3	Ti ₁	B	1.45	2.2	5.8	n. o.	0.76	1.4	28.0
4	Ti ₂	C	1.26	28.8	19.0	n. o.	1.23	3.3	29.9
5	Ti ₁	C	1.26	24.7	8.0	n. o.	2.14	1.2	23.2
6	Ti ₂	D	1.40	5.9	47.2	n. o.	2.26	1.7	29.8
7	Ti ₁	D	1.40	13.1	44.8	n. o.	3.21	2.1	20.5
8	Ti ₂	E	1.39	3.1	52.7	n. o.	8.55	1.7	20.9
9	Ti ₁	E	1.39	3.1	43.1	n. o.	0.77	1.9	14.8
10	Ti ₂	F	1.27	5.2	48.4	n. o.	6.65	1.7	16.9
11	Ti ₁	F	1.27	4.4	36.0	n. o.	1.50	4.0	12.9

^a [Ti] = 10 μ mol + [B] = 10 μ mol at 20 °C, under 1.0 atm ethylene pressure. ^b Units: g polymer/(mol Ti·atm ethylene·h). ^c By DSC. ^d By GPC relative to polystyrene standards. ^e Calculated from ¹H NMR. ^f Not observed.

Figure 1-6. ^{13}C NMR spectra (100 MHz, $\text{C}_2\text{D}_2\text{Cl}_4$, 130 °C) of the poly(ethylene-*co*-styrene) samples from Table 1-1, entries 1-3 in which catalyst nuclearity and connectivity is varied.



catalytic studies. It can be seen from entry 1 versus entry 2 in Table 1-1 that **C1-Ti₂ + B₁** incorporates 14.9% more styrene than does **Ti₂ + B₁**, presumably due to the enhanced cooperative effects arising from the diminished achievable Ti-Ti distance (see more below).

All of the present ethylene + styrene copolymers are amorphous and exhibit a single glass transition temperature (T_g), suggesting the resultant copolymers have approximately homogeneous styrene distributions. Moreover, it is found that T_g increases from 5.8 °C to 16.6 °C and then to 22.3 °C as the styrene incorporation level increases from 28.0 mol% to 32.3 mol% and then to 37.1 mol%, in agreement with reported T_g values for copolymers with similar styrene contents.^{8c}

Copolymerization of Ethylene and 4-Methylstyrene

The ¹³C NMR spectra (Figure 1-7) of the ethylene + 4-methylstyrene copolymers share an almost identical pattern to the ethylene + styrene copolymers in the aliphatic region except for the additional resonance at $\delta = 20.9$ ppm, which can be assigned to the phenyl ring methyl substituent. In the aromatic region, the chemical shifts of the *ipso* carbon and *para* carbon are displaced to $\delta = 143.4$ and 134.7 ppm, respectively. As for the comonomer incorporation level, ¹H NMR spectra show that **Ti₂ + B₁** enchains 29.9 mol% 4-methylstyrene, which is 28.9 % more than does **Ti₁ + B₁** (23.2 mol%), and the copolymer T_g also increases from 8.0 °C to 19.0 °C.

Copolymerization of Ethylene and 4-Fluorostyrene

Figure 1-8 shows the ¹³C NMR spectra of representative ethylene + 4-fluorostyrene copolymers. Compared to the ethylene + styrene copolymers, the methylene and ethylene region exhibits an almost identical pattern. In the aromatic region, the *ipso* carbon shifts to $\delta = 142.1$ ppm. The phenyl ring *para* carbon appears as a doublet centered at $\delta = 161.4$ ppm, due to the

Figure 1-7. ^{13}C NMR spectra (100 MHz, $\text{C}_2\text{D}_2\text{Cl}_4$, 130 $^\circ\text{C}$) of the poly(ethylene-co-4-methylstyrene) samples from Table 1-1, entries 4-5 in which catalyst nuclearity is varied.

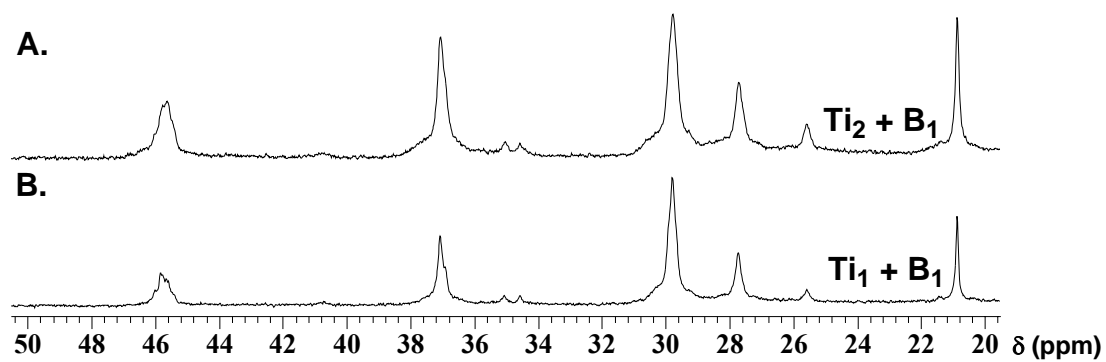
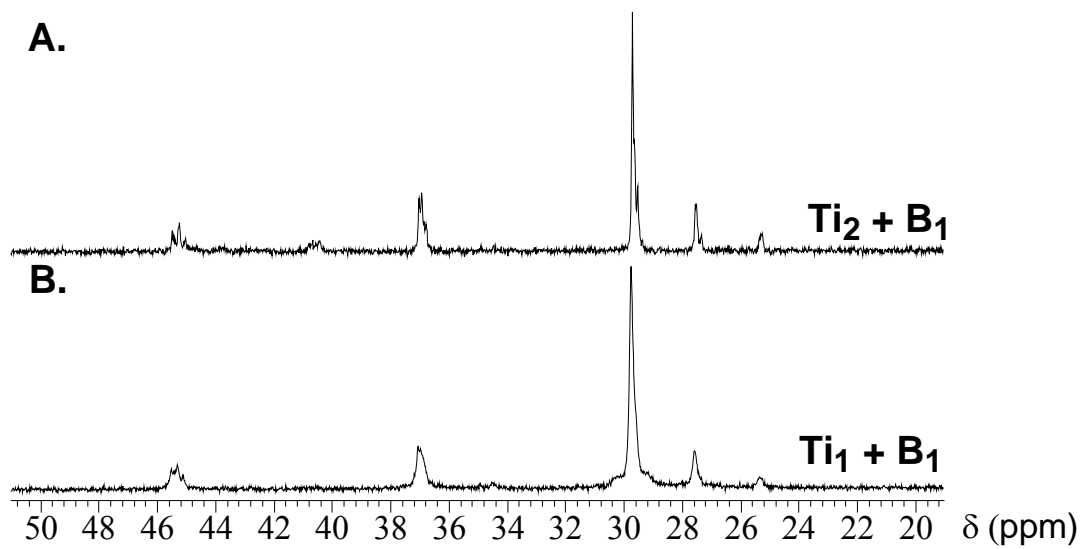


Figure 1-8. ^{13}C NMR spectra (100 MHz, $\text{C}_2\text{D}_2\text{Cl}_4$, 130 $^\circ\text{C}$) of the poly(ethylene-co-4-fluorostyrene) samples from Table 1-1, entries 6-7, in which the catalyst nuclearity is varied.



coupling to the fluoro substituent ($^1J_{C-F} = 243.4$ Hz). As for bimetallic effects in terms of comonomer incorporation level, the 1H NMR data reveal that **Ti₂ + B₁** enchains 45.4 % more 4-fluorostyrene than does **Ti₁ + B₁** (29.8 mol% vs 20.5 mol%). As a result, the copolymer T_g also increases from 44.8 °C to 47.2 °C.

Copolymerization of Ethylene and 4-Chlorostyrene

The ^{13}C NMR spectra (Figure 1-9) of the ethylene + 4-chlorostyrene copolymers also share an almost identical pattern to the ethylene + styrene copolymers in the aliphatic region. In the aromatic region, the chemical shifts of the *ipso* and *para* carbons are displaced to $\delta = 145.0$ and 131.5 ppm, respectively. Concerning the comonomer enchainment level, 1H NMR spectra indicate that **Ti₂ + B₁** enchains 20.9 mol% 4-chlorostyrene, which is 41.2 % greater than does **Ti₁ + B₁** (14.8 mol%). As a result, the T_g of the copolymers also increases from 43.1 °C to 52.7 °C.

Copolymerization of Ethylene and 4-Bromostyrene

The ^{13}C NMR spectra (Figure 1-10) of the ethylene + 4-bromostyrene copolymers share an almost identical pattern to the ethylene + styrene copolymers in the aliphatic region. In the aromatic region, the chemical shifts of the *ipso* and *para* carbons shift to $\delta = 145.3$ and 119.7 ppm, respectively. As for the comonomer incorporation level, 1H NMR spectra reveal that **Ti₂ + B₁** enchains 16.9 mol% 4-bromostyrene, which is 31.0 % more than does **Ti₁ + B₁** (12.9 mol%). As a result, the T_g of the copolymers increases from 36.0 °C to 48.4 °C.

Figure 1-9. ^{13}C NMR spectra (100 MHz, $\text{C}_2\text{D}_2\text{Cl}_4$, 130 $^\circ\text{C}$) of the poly(ethylene-co-4-chlorostyrene) samples from Table 1-1, entries 8-9, in which the catalyst nuclearity is varied.

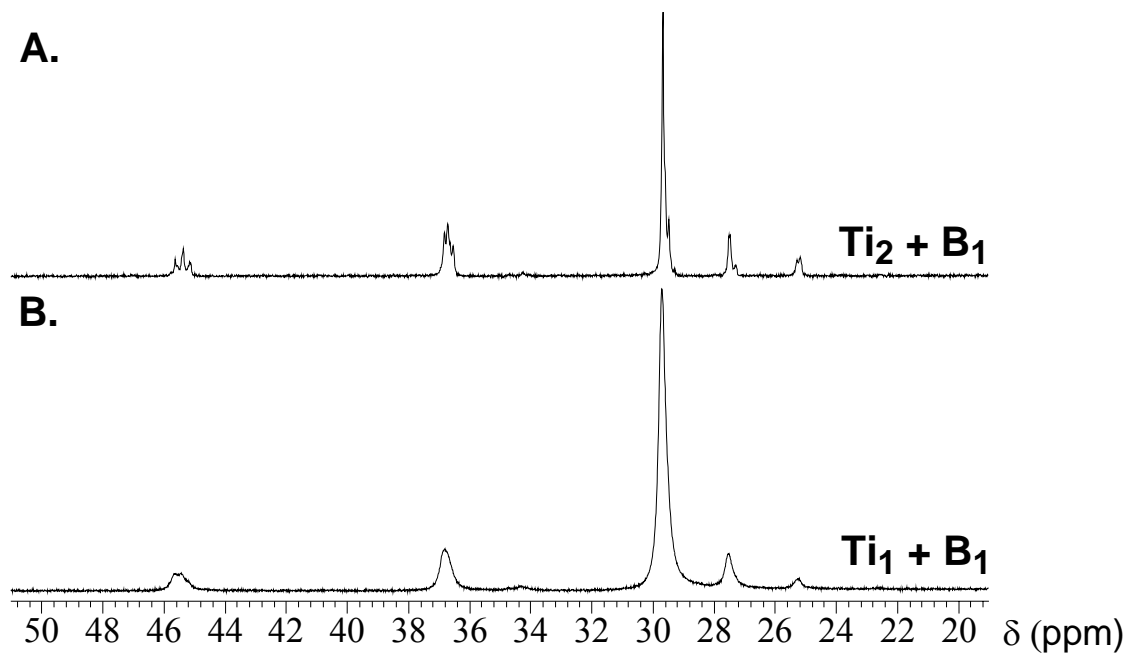
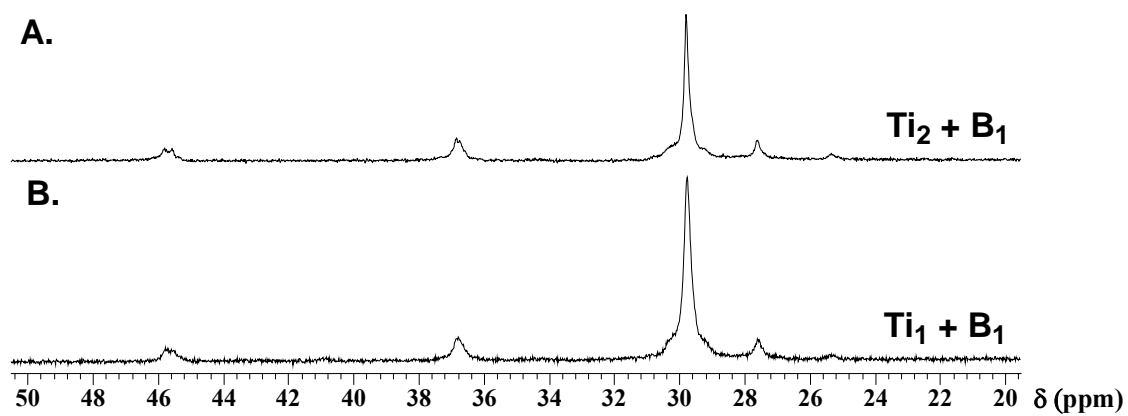


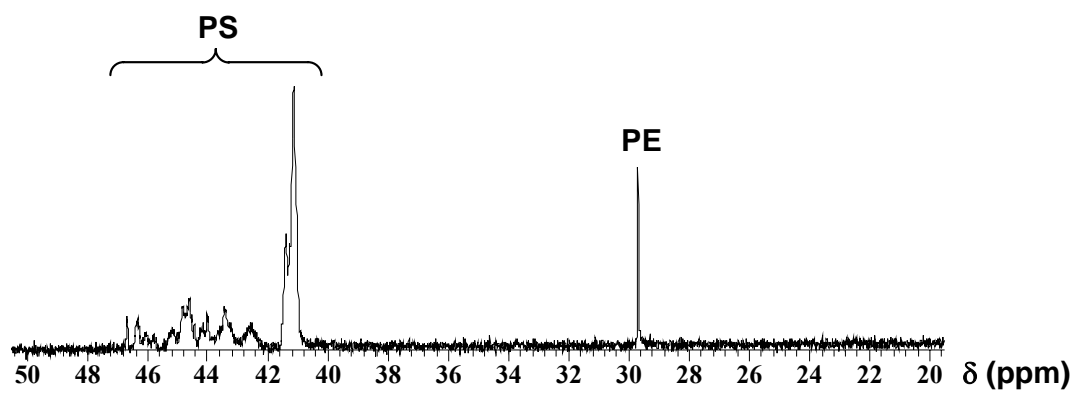
Figure 1-10. ^{13}C NMR spectra (100 MHz, $\text{C}_2\text{D}_2\text{Cl}_4$, 130 $^\circ\text{C}$) of the poly(ethylene-co-4-bromostyrene) samples from Table 1-1, entries 10-11, in which the catalyst nuclearity is varied.



III. Copolymerization of Ethylene and Styrene by Mononuclear and Binuclear Organozirconium Catalysts

Copolymerization of ethylene + styrene in the presence of organozirconium catalysts was also investigated. Although CGCZr catalysts (**Zr₁**, **Zr₂**, and **C1-Zr₂**) are competent for both ethylene^{5b,h} and styrene homopolymerizations (see more below), attempts to effect ethylene + styrene copolymerization were unsuccessful, yielding only heterogeneous polyethylene and polystyrene mixtures (Figure 1-11). In addition, with increasing styrene : ethylene feed ratios, the percentage of polystyrene in the obtained polymeric product increases accordingly. Copolymerization of ethylene and styrene at both elevated and decreased polymerization temperatures, trying to depress the homopropagation selectivity, also failed, again producing mixtures of homopolymers. This is in agreement with previous observations that CGCZr catalysts are not efficient for ethylene + methylenecycloalkane copolymerization.^{5b}

Figure 1-11. Representative ^{13}C NMR spectrum (100 MHz, $\text{C}_2\text{D}_2\text{Cl}_4$, 130 $^\circ\text{C}$) of the polymeric product in ethylene + styrene copolymerization mediated by CGCZr^+ catalysts.



IV. Homopolymerization of Styrene and End Group Analysis

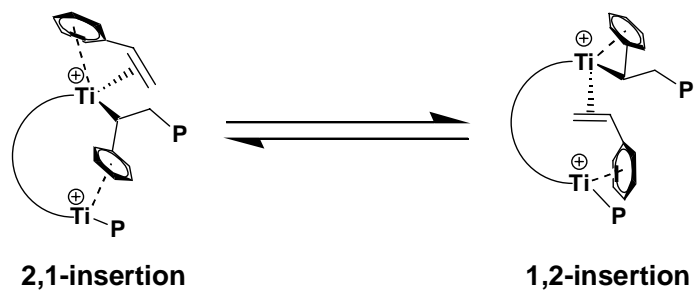
Previously, we communicated that under identical styrene homopolymerization conditions, bimetallic catalyst \mathbf{Ti}_2 exhibits ~ 50 times greater activity than the analogous monometallic catalyst \mathbf{Ti}_1 , and end group analysis suggests that unusual 1,2-regiochemistry is installed in $\sim 50\%$ of the initiation steps. Here, we extended our studies to the methylene-bridged bimetallic catalyst $\mathbf{C1-Ti}_2$ and the organozirconium analogues $\mathbf{C1-Zr}_2$, \mathbf{Zr}_2 , and \mathbf{Zr}_1 to study the effects of metal-metal proximity on the cooperative bimetallic effect. As illustrated in Table 1-2, under identical styrene polymerization conditions, $\mathbf{C1-Ti}_2 + \mathbf{B}_1$ and $\mathbf{Ti}_2 + \mathbf{B}_1$ exhibit ~ 65 and ~ 50 times greater homopolymerization activities than does monometallic $\mathbf{Ti}_1 + \mathbf{B}_1$, respectively. Furthermore, $\mathbf{C1-Zr}_2 + \mathbf{B}_1$ and $\mathbf{Zr}_2 + \mathbf{B}_1$ exhibit ~ 8 and ~ 4 times greater activities, respectively, than does monometallic $\mathbf{Zr}_1 + \mathbf{B}_1$. The monomodal GPC traces together with polydispersities ~ 2 and end group analyses (see more below) suggest that all of the polystyrene homopolymers are produced exclusively via a coordinative/insertive single-site pathway. The marginal activity of mononuclear catalyst \mathbf{Ti}_1 is thought to arise from the “back-biting” of the last inserted styrene (**A**), which prevents incoming monomer coordination and enchainment, while mononuclear \mathbf{Zr}_1 exhibits respectable styrene polymerization activity. This disparity in styrene homopolymerization activity argues that more open coordination sphere of Zr here is better able to overcome the “back-biting”. The aforementioned trends in styrene homopolymerization activities for both organotitanium and organozirconium catalysts ($\mathbf{C1-M}_2 > \mathbf{M}_2 > \mathbf{M}_1$) most likely reflect enhanced intramolecular cooperative effects with increased metal-metal proximity as the second metal center is poised to disrupt styrene “back-biting” to the first metal center (Scheme 1-4). Interestingly, the molecular weights and glass transition temperatures of the product polystyrenes exhibit the opposite trend from activities: $\mathbf{C1-M}_2 < \mathbf{M}_2 < \mathbf{M}_1$, suggesting

Table 1-2. Styrene Homopolymerization Results ^a

Entry	Cat. + Cocat.	Time (hr)	Yield (g)	Activity ^b ($\times 10^5$)	T _g ^c (°C)	T _m ^c (°C)	M _w ^e ($\times 10^4$)	M _w /M _n ^e
1	Ti ₁ + B ₁	3	0.08	0.03	104.6	n.o. ^d	1.96	1.9
2	Ti ₂ + B ₁	3	3.13	1.04	96.4	n.o. ^d	1.04	1.6
3	C1-Ti ₂ + B ₁	2	3.93	1.96	94.6	n.o. ^d	0.64	2.6
4	Ti ₁ + B ₂	3	0.06	0.02	100.5	n.o. ^d	1.21	1.7
5	Ti ₂ + B ₂	3	3.36	1.12	89.2	n.o. ^d	0.80	1.5
6	Zr ₁ + B ₁	2	1.09	0.54	101.2	n.o. ^d	1.30	1.6
7	Zr ₂ + B ₁	2	3.91	1.96	94.2	n.o. ^d	1.02	1.6
8	C1-Zr ₂ + B ₁	1	4.07	4.07	93.1	n.o. ^d	0.70	2.7

^a [M] = 10 μ mol + [B] = 10 μ mol, 5 mL styrene + 25 mL toluene at 20 °C. ^b Units: g polymer/(mol metal·h). ^c DSC. ^d Not observed. ^e GPC relative to polystyrene standards.

Scheme 1-4. Proposed Mechanism for Styrene Insertion Regiochemistry



functionally different propagation/termination kinetics (Table 1-2). Furthermore, organozirconium catalysts always exhibit greater activities than the corresponding organotitanium catalysts of the same nuclearity and afford comparable molecular weight polystyrene, in sharp contrast to ethylene homopolymerizations, where organotitanium catalysts exhibit far greater activities and afford much higher molecular weight polyethylenes than produced by the corresponding organozirconium catalysts.

Regarding styrene insertion regiochemistry,²⁰ Scheme 1-5 depicts all possible end groups produced during the initiation steps in styrene homopolymerization. As can be seen from Figure 1-12,²⁶ **C1-Ti₂** and **Ti₂** share very similar end group distributions, installing 1,2-insertion regiochemistry in ~ 50% of all initiations. Interestingly, when the CGCZr-based catalysts are changed from **Zr₁** to **Zr₂** and **C1-Zr₂**, an increasing percentage of 2,1-insertion regiochemistry is installed (Figure 1-13). This is in agreement with the proposed mechanism, that is, although mononuclear catalysts have strongly preferred styrene insertion regiochemistries (2,1-insertion for organotitanium,^{20a,d,e} 1,2-insertion for organozirconium^{26a}), the bimetallic catalytic environments tend to moderate the opposite Ti vs Zr selectivities in insertion regiochemistry.

Scheme 1-5. Possible Styrene Insertion Pathways during Chain Initiation

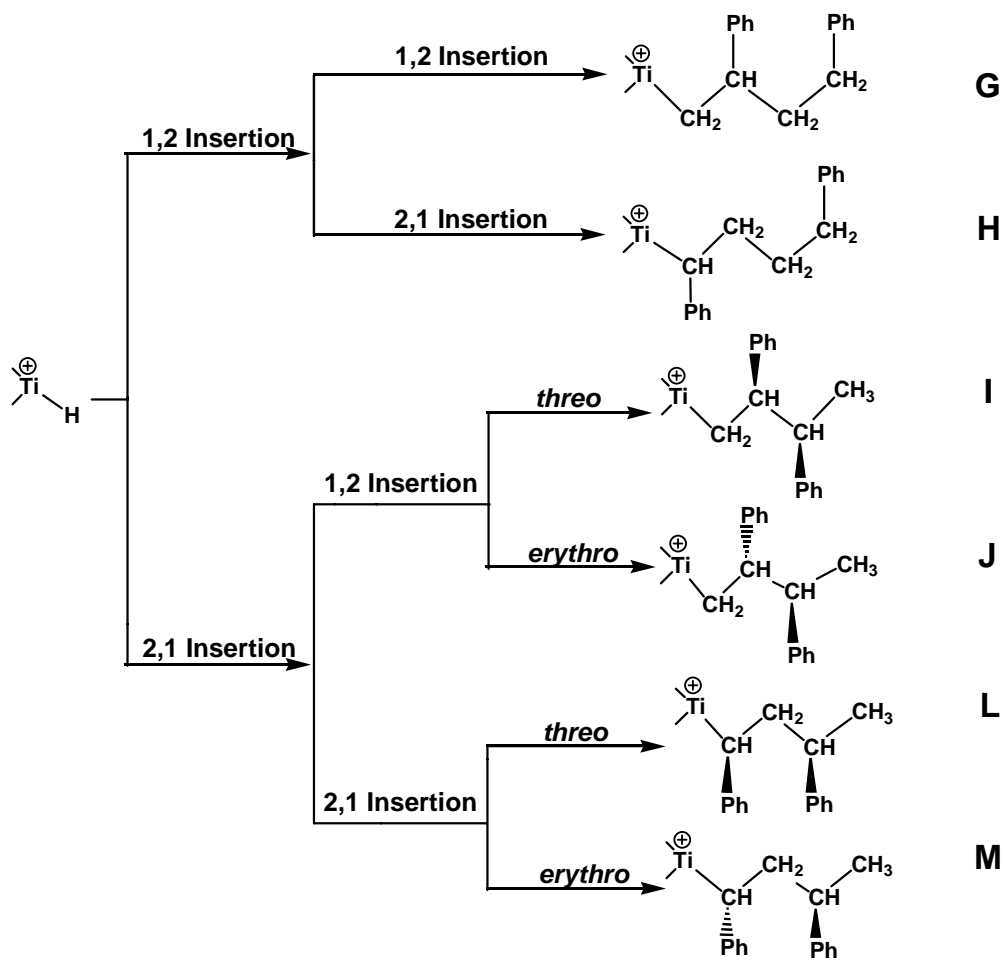


Figure 1-12. ^{13}C NMR end group analysis (100 MHz, $\text{C}_2\text{D}_2\text{Cl}_4$, 130 $^\circ\text{C}$) of the polystyrenes from Table 1-2, entries 2-3.

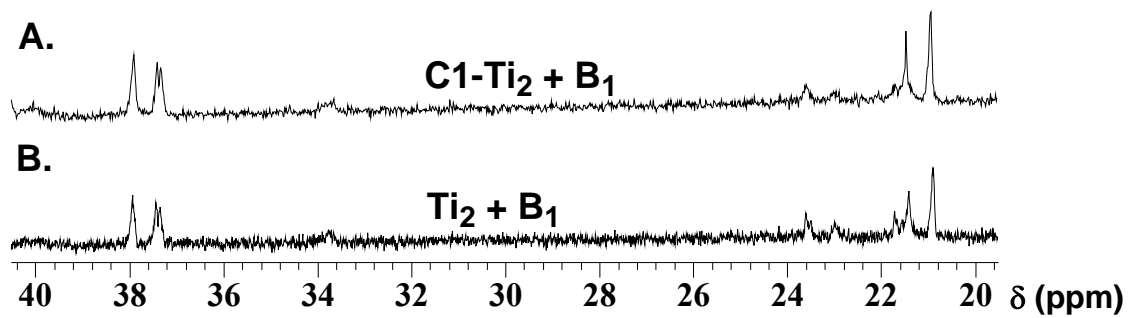
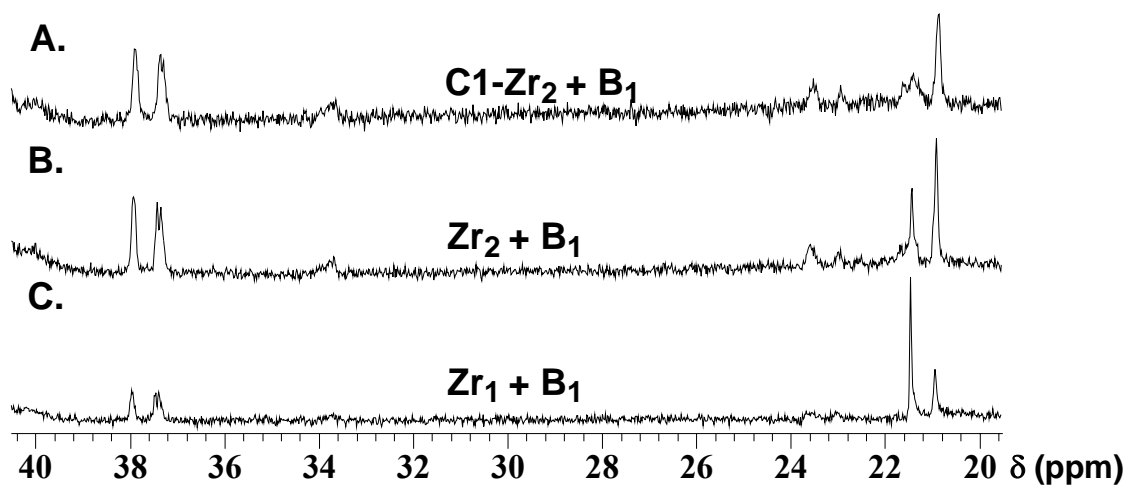


Figure 1-13. ^{13}C NMR end group analysis (100 MHz, $\text{C}_2\text{D}_2\text{Cl}_4$, 130 °C) of the polystyrenes from Table 1-2, entries 6-8.



V. Polar Solvent Effects

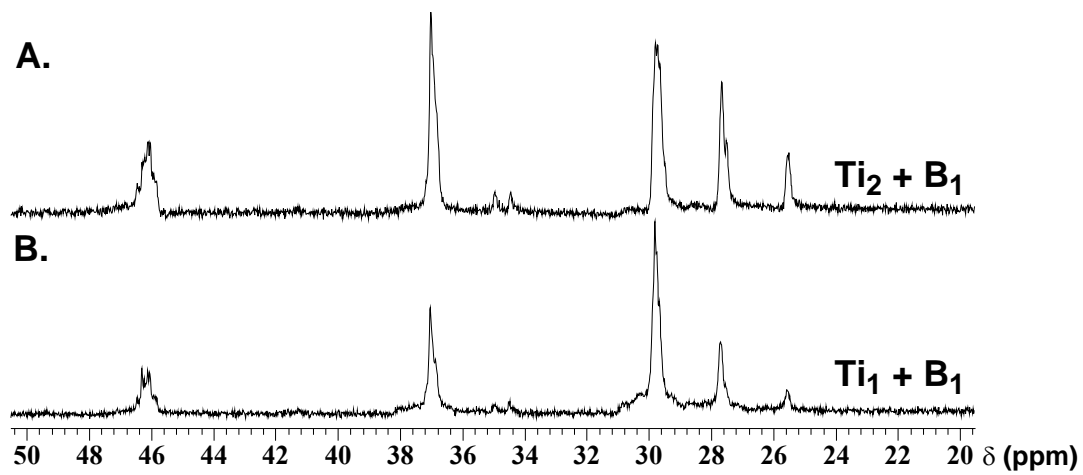
Previously reported **Ti₁**, **Ti₂** ethylene + α -olefin copolymerization results^{5a,b} in a more polar, ion pair weakening medium suggested that the proposed agostic interactions can be suppressed by polar C₆H₅Cl ($\epsilon_r = 5.68$ vs $\epsilon_r = 2.38$ for toluene),²⁹ as evidenced by the diminished comonomer enchainment efficiency of **Ti₂**. However, such polar solvent effects might not be suppressed in the present styrene polymerizations since the metal-arene interactions in the proposed mechanistic scenario may be stronger than the C-H agostic interactions in α -olefin polymerizations. As shown in Table 1-3, the data on ethylene + styrene copolymerizations mediated by both **Ti₂** and **Ti₁** in C₆H₅Cl reveal that substantial amounts of atactic polystyrene are coproduced in addition to poly(ethylene-*co*-styrene), in sharp contrast to copolymerization results carried out in toluene where only copolymers are obtained. After removing the atactic polystyrene via solvent fractionation with methylethyl ketone (MEK), ¹³C NMR data (Figure 1-14) reveal that the styrene incorporation levels for both **Ti₂** and **Ti₁** are significantly depressed in comparison to the copolymerization results in toluene, largely due to the decreased styrene : ethylene feed ratio arising from the coproduction of atactic polystyrene (depletion of styrene). Note that there are negligible solubility differences for ethylene in toluene and chlorobenzene under the present polymerization conditions³⁰. Interestingly, although the effective styrene : ethylene feed ratio for **Ti₂** is lower than that for **Ti₁**, since the former produces more atactic polystyrene, **Ti₂** still incorporates 31.3% more styrene than **Ti₁**, while in toluene **Ti₂** only enchains 15.4% more styrene than **Ti₁**. It can therefore be seen that this bimetallic selectivity effect is actually enhanced in the polar solvent, arguing that any C₆H₅Cl coordination cannot compete with the metal-arene interaction.

Table 1-3. Copolymerization of Ethylene and Styrene in C₆H₅Cl with Cocatalyst **B₁**^a

Entry	Cat.	Time (min)	Yield (g)	PS wt% ^b	Activity ^c (×10 ⁶)	T _g ^d (°C)	T _m ^d (°C)	M _w ^f (×10 ⁵)	M _w /M _n ^f	Styrene% ^g (mol%)
1	Ti ₂	40	4.85	79.7	1.4	9.2	n.o. ^e	3.49	2.4	28.5
2	Ti ₁	18	3.06	55.4	2.0	-3.9	n.o.	4.62	1.8	21.7

^a [Ti] = 5 μmol + [B] = 5 μmol, 10 mL styrene + 50 mL chlorobenzene at 20 °C. ^b Determined from solvent fractionation. ^c Units: g polymer/(mol Ti·atm ethylene·h). ^d By DSC. ^e Not observed. ^f By GPC relative to polystyrene standards. ^g Calculated from ¹H NMR.

Figure 1-14. ^{13}C NMR spectra (100 MHz, $\text{C}_2\text{D}_2\text{Cl}_4$, 130°C) of two poly(ethylene-*co*-styrene) samples from Table 1-4.



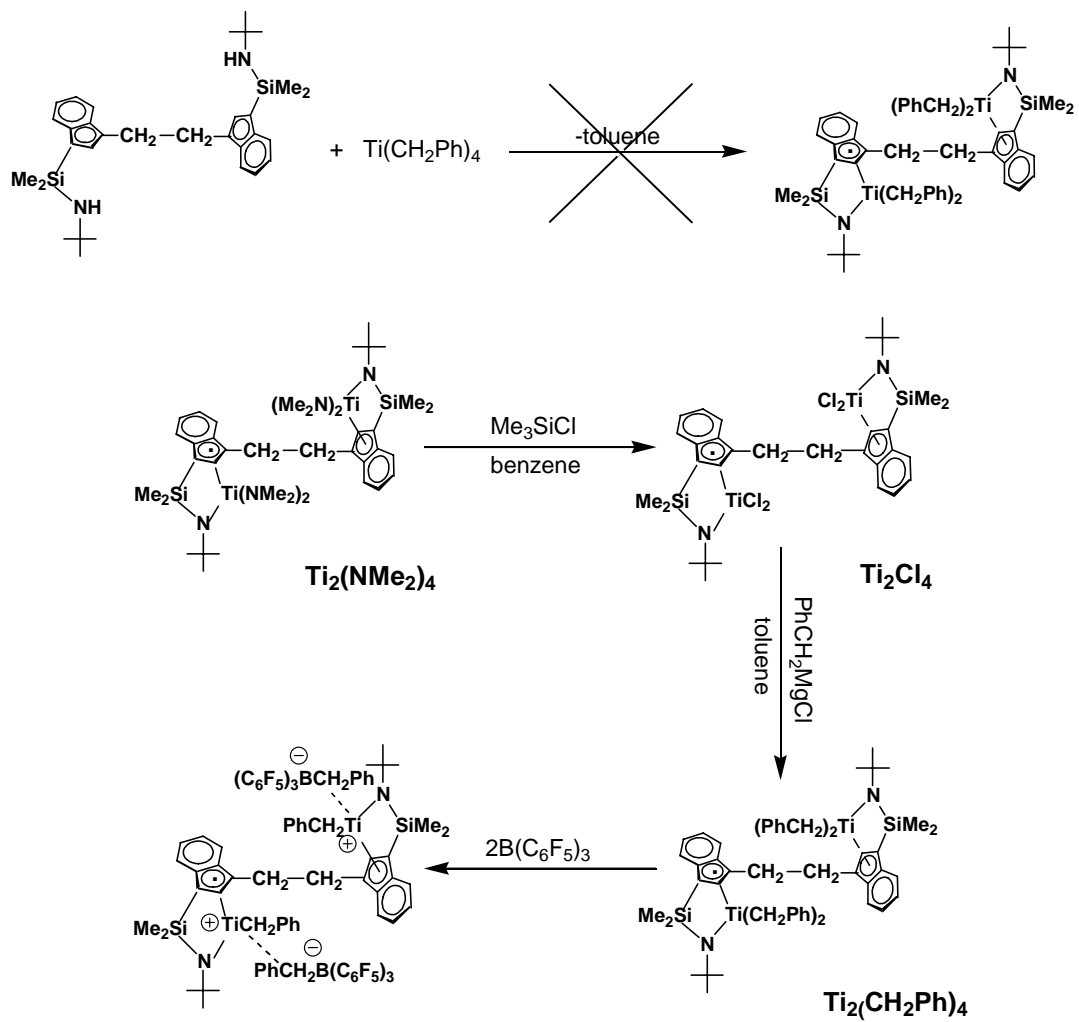
VI. Synthesis, Characterization, and Activation Studies of the Model Compound

$\text{Ti}_2(\text{CH}_2\text{Ph})_4$

To further probe the proposed enchainment mechanism in **C1-Ti₂** and **Ti₂**-mediated styrene homopolymerization involving one cationic metal center interacting with the phenyl ring of the last inserted styrene on the other cationic metal center, thus preventing “back-biting” and deactivation of the electrophilic metal center, model compound **Ti₂(CH₂Ph)₄** was designed to simulate bimetallic Ti-polymeryl species after cocatalyst alkyl abstraction. Initial attempts to synthesize the title complex via direct protonolytic alkane elimination³¹ were unsuccessful, presumably due to the sterically demanding environment of the bimetallic CGC ligand structure (Scheme 1-6). Thus, more conventional methodology was employed.^{32,33} As illustrated in Scheme 1-6, reaction of known **Ti₂(NMe₂)₄**^{5a} with excess Me₃SiCl at room temperature cleanly affords the tetrachloro complex **Ti₂Cl₄**. Subsequent reaction with PhCH₂MgCl affords the tetrabenzyl complex **Ti₂(CH₂Ph)₄**, which was characterized by standard spectroscopic and analytical techniques, as well as by X-ray diffraction (vide infra).

In the ¹H NMR spectrum of **Ti₂(CH₂Ph)₄**, the methylene protons of the two magnetically non-equivalent diastereotopic benzyl proton pairs appear as two AB spin patterns with ²J_{H-H} coupling constants ~ 10.5 Hz. The *ortho* protons of the benzyl groups exhibit normal resonances at δ = 6.71 and 6.62 ppm, respectively.^{19d,33a,c} The ¹³C{¹H} NMR spectrum reveals two distinct signals at δ = 84.90 and 80.23 ppm, respectively, corresponding to the two non-equivalent methylene carbons of the magnetically non-equivalent benzyl groups. Furthermore, the *ipso* carbons of the benzyl groups are found to exhibit normal chemical shifts at δ = 150.09 and 146.58 ppm, respectively. Unlike those reported for some neutral multihapto metal-benzyl

Scheme 1-6. Synthetic Route to Model Compound $\text{Ti}_2(\text{CH}_2\text{Ph})_4$



complexes,³³ the aforementioned NMR spectroscopic evidence as well as the solid state structural data (see more below) suggest that for **Ti₂(CH₂Ph)₄**, all of the benzyl groups engage in an η^1 -coordination mode both in solution and in the solid state.

Although mixing **Ti₂(CH₂Ph)₄** and two equiv. B(C₆F₅)₃ in benzene-d₆ immediately results in the formation of dark red solids, and ¹H NMR spectroscopy indicates clean double-benzyl abstraction by the cocatalyst/activator, attempts to isolate the pure crystalline bimetallic ion pair complex were unsuccessful, most likely due to rapid thermal decomposition within hours, as monitored by ¹H NMR spectroscopy. Interestingly, among the three possible diastereomeric double benzyl abstraction products, only one of the two C₂-symmetric ion pair complexes could be identified, since only a single set of upfield-shifted ligand resonances was observed. This preferential reactivity of B(C₆F₅)₃ with one of the two inequivalent benzyl groups is in sharp contrast to parallel activation studies of **Ti₁**, where both possible ion pair complex isomers are observed in solution.^{5a} The diastereotopic benzylic proton pairs of the two isomeric cationic Ti centers still exhibit AB spin patterns, evidenced by two sets of doublets centered at $\delta = 2.91$ and 2.43 ppm with an average ${}^2J_{\text{H-H}} \sim 8.0$ Hz. This decrease in the chemical shift difference between the two benzylic hydrogens ($\Delta\delta = 0.48$ after activation vs $\Delta\delta = 1.63$ before activation) provides evidence for η^1 -PhCH₂Ti⁺ coordination mode, since η^n -PhCH₂Ti⁺ bonding should plausibly make the two benzylic protons more magnetically inequivalent and therefore increase the chemical shift difference.^{19d} The reduction in coupling constant (c.f., **Ti₂(CH₂Ph)₄**: ${}^2J_{\text{H-H}} = 10.5$ Hz) most likely reflects an α -agostic interaction between the electrophilic Ti center and a benzylic C-H bond, which is thought to stabilize cationic metal centers during olefin polymerization.^{6c,34} More importantly, this ${}^2J_{\text{H-H}}$ reduction as well as normal Ti⁺CH₂Ph *ortho* proton chemical shifts^{19d,33a,c} also argue against the possibility of dominant η^n -PhCH₂Ti⁺

coordination, which is expected to increase the sp^2 character of the benzylic carbon and thus increase $^2J_{\text{H-H}}$.³³ The fact that only one broad ^1H resonance at $\delta = 3.62$ ppm is observed for the BCH_2Ph protons and that no signal in the range of $\delta = 5-6$ ppm is observed for the BCH_2Ph *ortho* protons argues that $\eta^1\text{-PhCH}_2\text{B}(\text{C}_6\text{F}_5)_3^-$ bonding also predominates.³¹

VII. Molecular Structure of Model Compound $\text{Ti}_2(\text{CH}_2\text{Ph})_4$

A summary of crystal structure data for the complex $\text{Ti}_2(\text{CH}_2\text{Ph})_4$ is presented in Table 1-4, and selected bond distances and angles for $\text{Ti}_2(\text{CH}_2\text{Ph})_4$ are summarized in Table 1-5. Similar to the previously reported molecular structure of $\text{Ti}_2(\text{NMe}_2)_4$, the crystal structure of $\text{Ti}_2(\text{CH}_2\text{Ph})_4$ (Figure 1-15) reveals an inversion center with a CGCTi moiety located on either side of the ethylenebis(indenyl) fragment and with the two π -coordinated indenyl rings in a diastereomeric relationship. As can be seen from Figure 1-15, the crystal consists of a single diastereomer (*SR*, *RS*). The bond angles $\text{C}(15)\text{-C}(14)\text{-Ti}(1) = 126.12(18)^\circ$ and $\text{C}(8)\text{-C}(7)\text{-Ti}(1) = 117.79(18)^\circ$ suggest that all of the benzyl groups exhibit an η^1 -coordination mode, since $\eta^n\text{-PhCH}_2\text{Ti}$ coordination would bend the phenyl moiety close to the metal center and consequently afford substantially smaller bond angles ($< 90^\circ$).^{19a,b,c,f,i,j,k} The sum of the bond angles around nitrogen atom N(1) is 359.91° , indicating that the formal hybridization of nitrogen atom N(1) is sp^2 . The $^t\text{BuN-Ti}$ bond distance ($\text{Ti}(1)\text{-N}(1)$) is $1.931(2)$ Å, substantially shorter than the one reported for $\text{Ti}_2(\text{NMe}_2)_4$ ($1.994(4)$ Å), largely due to increased π donation from the N formal lone pair electrons to the empty Ti^{4+} d orbitals since no additional nitrogen atoms are engaged in π donation. The sum of bond angles around indenyl ring carbon atom C(23) is 351.2° , indicating that the $\text{C}(23)\text{-Si}(1)$ bond deviates appreciably from the indenyl ring plane because of the constrained geometry. The carbon atoms of the Cp ring do not exhibit equal bonding distances to the Ti center. The average bond lengths of $\text{Ti}(1)\text{-C}(22)/\text{Ti}(1)\text{-C}(23)$ and $\text{Ti}(1)\text{-C}(21)/\text{Ti}(1)\text{-}$

Table 1-4. Summary of Crystal Structure Data for **Ti₂(CH₂Ph)₄**

Empirical formula	C _{62.50} H ₇₆ N ₂ Si ₂ Ti ₂
Formula weight	1007.23
Crystal Color, habit	red, block
Crystal dimensions (mm)	0.520 x 0.424 x 0.374
Crystal system	triclinic
Space group	<i>P</i> $\bar{1}$
<i>a</i> , Å	12.299(2)
<i>b</i> , Å	16.117(3)
<i>c</i> , Å	16.873(3)
α , deg	97.363(3)
β , deg	101.480(3)
γ , deg	112.119(2)
<i>V</i> , Å ³	2959.5(8)
<i>Z</i>	2
<i>d</i> (calcd), g/cm ³	1.130
μ , mm ⁻¹	0.348
<i>T</i> _{min} – <i>T</i> _{max}	0.8481-0.8912
Measured reflections	15176
Independent reflections	15176
Reflections > 2 σ (<i>I</i>)	12744
<i>R</i> _{int}	0.0000
<i>R</i> [<i>F</i> ² > 2 σ (<i>F</i> ²)]	0.0655
<i>wR</i> (<i>F</i> ²)	0.1894
<i>S</i>	1.038
No. of parameters	653

Conditions: CCD area detector diffractometer; ψ and ω scans; temperature for data collection

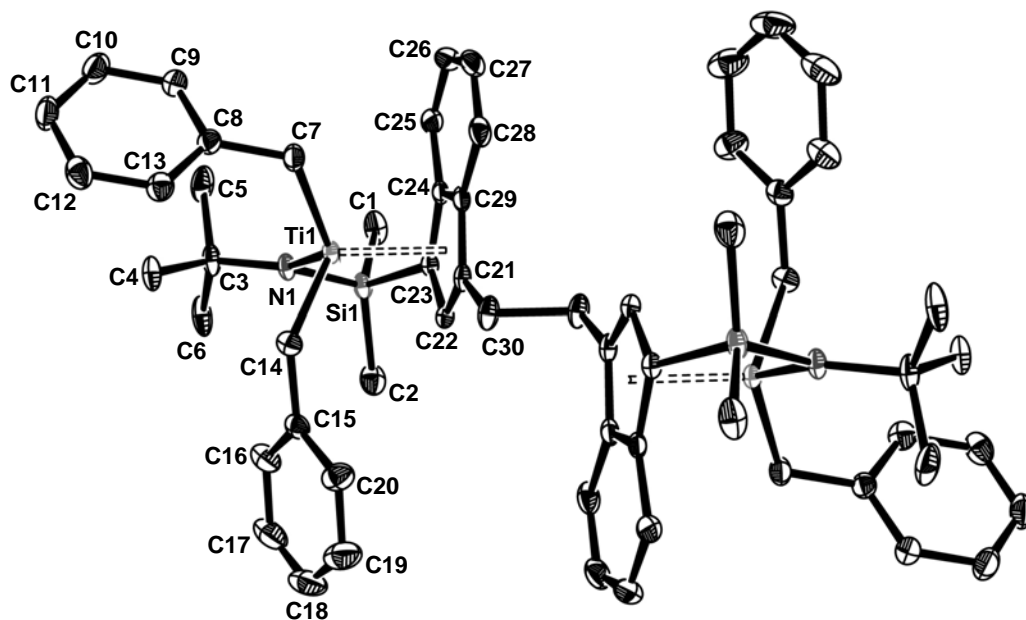
153(2) K; Mo K α radiation; λ = 0.71073 Å.

Table 1-5. Selected Bond Distances (Å) and Bond Angles (deg) for **Ti₂(CH₂Ph)₄**

Bond Distances			
Ti(1)-C(21)	2.498(3)	C(14)-C(15)	1.493(4)
Ti(1)-C(22)	2.341(2)	Ti(1)-N(1)	1.931(2)
Ti(1)-C(23)	2.271(2)	Si(1)-N(1)	1.753(2)
Ti(1)-C(24)	2.413(2)	Si(1)-C(1)	1.870(3)
Ti(1)-C(29)	2.564(3)	Si(1)-C(2)	1.853(3)
Ti(1)-C(7)	2.154(3)	Si(1)-C(23)	1.854(3)
Ti(1)-C(14)	2.132(3)	N(1)-C(3)	1.486(3)
C(7)-C(8)	1.480(4)		
Bond Angles			
N(1)-Ti(1)-C(14)	106.42(10)	N(1)-Si(1)-C(23)	93.54(10)
N(1)-Ti(1)-C(7)	117.39(10)	C(2)-Si(1)-C(1)	108.26(15)
C(14)-Ti(1)-C(7)	99.55(11)	C(1)-Si(1)-C(23)	112.45(13)
C(15)-C(14)-Ti(1)	126.12(18)	C(2)-Si(1)-C(23)	110.22(13)
C(8)-C(7)-Ti(1)	117.79(18)	C(3)-N(1)-Si(1)	124.59(17)
N(1)-Si(1)-C(1)	116.89(13)	C(3)-N(1)-Ti(1)	133.74(17)
N(1)-Si(1)-C(2)	114.77(12)	Si(1)-N(1)-Ti(1)	101.58(10)
C(15)-C(14)-Ti(1)	126.12(18)	C(8)-C(7)-Ti(1)	117.79(18)

Figure 1-15. The molecular structure and atom numbering scheme for the model compound

$\text{Ti}_2(\text{CH}_2\text{Ph})_4$. Thermal ellipsoids are drawn at the 30% probability level.



C(24)/Ti(1)–C(29) are 2.306(2) and 2.492(3) Å, respectively. The difference is 0.186(5) Å, 0.018(14) Å greater than the value reported for the Cp ligand in $\text{Ti}_2(\text{NMe}_2)_4$ [2.542(5)–2.374(4) = 0.168(9) Å],^{5a} and 0.055 Å greater than that value found for the more symmetrical Cp ligand in $[(\eta^5\text{-C}_5\text{Me}_4)\text{SiMe}_2(\text{tBuN})]\text{TiCl}_2$, which is 2.436 – 2.305 = 0.131 Å,³⁵ indicating a substantially more “slipped” coordination of the Cp ligand in $\text{Ti}_2(\text{CH}_2\text{Ph})_4$.

Discussion

I. Bimetallic Proximity Effects in Polymerization.

From the polymerization results outlined above, the enhanced styrene incorporation in C1-Ti_2 - vs Ti_2 -mediated ethylene + styrene copolymerizations, and the significantly enhanced activities in C1-M_2 - vs M_2 -mediated styrene homopolymerizations (M = Ti and Zr), suggest that C1-M_2 structures exhibit enhanced metal-metal cooperativity effects compared to M_2 . It is known that in the single crystal structure of C_1 -symmetric C1-Zr_2 ,^{5b} the two indenyl rings are locked (estimated rotation barrier > 63 kcal/mol, Spartan 2002, MP3 level) into a twisted conformation by the methylene bridge, constraining the two metal centers to the same side of the molecule,^{5b} whereas in the solid state structure of C_1 -symmetric Zr_2 , the two Zr atoms reside on opposite sides of the molecule but with minimal estimated barriers to accessing other conformations. As a result, the minimum accessible Zr...Zr distance in C1-Zr_2 (7.392 Å) is ~ 1.28 Å shorter than that in Zr_2 (8.671 Å).^{5b} Therefore, the locked and shorter accessible metal-metal distance in the case of C1-M_2 would enable more efficient binuclear metal-styrene binding (Scheme 1-4), hence affording more efficient comonomer enchainment and greater styrene homopolymerization activity than M_2 . A similar trend has been reported for ethylene + 1-hexene copolymerizations, where C1-Zr_2 incorporates more 1-hexene than does Zr_2 under identical reaction conditions.^{5b}

II. Comparison between CGCTi⁺ and CGCZr⁺ Catalytic Properties.

In the aforementioned styrene homopolymerization studies, CGCZr⁺-based catalysts exhibit far greater activities than do CGCTi⁺-based catalysts having the same nuclearity and afford polymeric products with comparable molecular weights. In contrast, for polymerizations involving ethylene, organotitanium catalysts generally exhibit far greater activities and afford much higher molecular weight polyethylenes than do analogous organozirconium catalysts. It is known that for ethylene polymerizations, coordination of ethylene to the cationic metal center in the presence of the counteranion is usually the rate-determining step for each ethylene insertion,³⁶ while for styrene polymerizations, insertion of the coordinated styrene to the metal-polymeryl bond is thought to be the rate-determining step.^{24b} Theoretical studies regarding ethylene + styrene copolymerizations^{27a,c,e} as well as experimental results^{23b} also reveal that ethylene has lower complexation energy than styrene while the latter has a significantly higher insertion barrier than the former. DFT calculations suggest that solvent molecules are much more likely to compete with ethylene for coordination to CGCZr⁺ than to CGCTi⁺,³⁷ and therefore, CGCTi⁺ is expected to have more efficient ethylene coordination and subsequent insertion. Moreover, tighter ion pairing in CGCZr⁺ versus CGCTi⁺³⁸ also makes ethylene coordination to CGCZr⁺ by displacing the counteranion more energetically demanding. On the other hand, insertion of styrene into the metal-polymeryl bond is a sterically more sensitive process, and thus CGCZr⁺ with a larger ionic radius should promote more rapid enchainment, all other factors being equal. This trend is similar to that observed for organolanthanide-catalyzed intramolecular aminoalkene hydroamination/cyclization, where the cyclization rate increases with increasing lanthanide radius since olefin insertion is turnover-limiting.²⁸

Unlike their CGCTi⁺ counterparts which are competent for efficient ethylene + styrene

copolymerization, under the reaction conditions investigated, all of the three CGCZr⁺ catalysts (C₁-Zr₂, C₂-Zr₂, and Zr₁) fail to produce ethylene + styrene copolymers although both monomers can be homopolymerized at these Zr centers. As a matter of fact, very few zirconium-based catalysts^{9j, 21b} are reported in the literature to efficiently copolymerize ethylene + styrene. This difference in the catalytic comonomer incorporation selectivity was previously observed in our work on isobutene, methylenecyclopentane, and methylenecyclohexane copolymerizations with ethylene: CGCTi⁺ catalysts incorporate significant quantities of sterically encumbered comonomers into polyethylene backbones, while CGCZr⁺ catalysts do not. One plausible explanation is that tighter ion pairing in CGCZr⁺ versus CGCTi⁺ structures leads to lower reactivity in terms of comonomer enchainment.³⁸

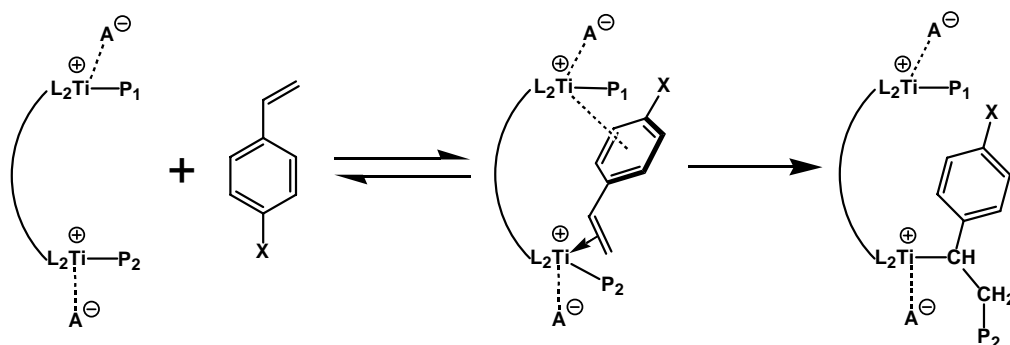
III. Bimetallic Effects on Comonomer Enchainment.

For all five styrenic comonomers investigated having various *para* substituents, under identical copolymerization conditions, binuclear catalyst **Ti₂** + **B₁** invariably incorporates far greater levels of comonomer than does the mononuclear **Ti₁** + **B₁** analogue, demonstrating the generality of the bimetallic effect previously observed only with styrene.^{5e} It is proposed that coordination of the styrenic comonomer to a cationic metal center is stabilized by interactions between the π -system of the substituted/unsubstituted phenyl ring with the proximate cationic metal center, which may facilitate/stabilize comonomer capture/binding and enhance the subsequent enchainment probability (Schemes 1-4 and 1-7). The bimetallic effect, which is defined here as the relative comonomer enchainment selectivity difference between **Ti₂** and **Ti₁** (eq. 10), is found to depend strongly on the arene substituent and, all other factors being equal in

$$\text{Bimetallic Effect} = \frac{\% \text{Styrenic}(\text{Ti}_2) - \% \text{Styrenic}(\text{Ti}_1)}{\% \text{Styrenic}(\text{Ti}_1)} \times 100\% \quad (10)$$

the proposed model, would be expected to increase as the interaction between the arene π -system

Scheme 1-7. Pathways for Styrenic Comonomer Enchainment in Bimetallic Catalyst-Mediated Ethylene Copolymerization



and the electrophilic metal center increased. Since all the styrenic comonomers possess almost identical steric characteristics, it is reasonable to assume that the π -electron density on the phenyl ring would dominate the metal-arene interaction.

It is known that such metal-benzyl arene interactions primarily involve the benzylic *ipso* carbon,^{19,33} and therefore, the bimetallic effect should track the *ipso* carbon π -electron density of the styrenic comonomer. As shown in Table 1-6, the observed bimetallic effect parallels the same trend as the electron density on the styrenic comonomer *ipso* carbon atom as qualitatively assayed by the ¹³C NMR chemical shifts.³⁹ Although reactivity ratio data are not available for direct comparison due to the lack of ethylene solubility data in some comonomers, the general observed trend is informative, and the results are consistent with the mechanistic picture proposed: the stronger the metal-arene interaction, the more efficiently **Ti₂** enchains the styrenic comonomer vs **Ti₁**.

IV. Solvent Polarity Effects on Polymerization.

It was reported previously^{5a,b} that for ethylene copolymerizations carried out in polar C₆H₅Cl as the solvent, the comonomer enchainment level difference between bimetallic **M₂** catalysts and monometallic **M₁** catalysts (M = Ti for ethylene + methylenecyclopentane copolymerization;^{5a} M = Zr for ethylene + 1-hexene copolymerization^{5b}) diminishes since the polar solvent can compete for/coordinate to the electrophilic metal centers and weaken/replace agostic interactions,²⁹ which were proposed to be mechanistically central to the observed binuclear enchainment effects. The present copolymerization results in the same polar solvent argue that, operationally, the metal-arene interaction remains largely intact in C₆H₅Cl since the significant disparity of styrene incorporation levels between **Ti₂** and **Ti₁** remain almost unchanged. Indeed, it has been reported that the η^2 -bonding mode of d^0 metal-benzyl species

Table 1-6. Correlation between the Bimetallic Effect (\mathbf{Ti}_2 vs \mathbf{Ti}_1 Comonomer Enchainment Selectivity) and *ipso* Carbon Chemical Shift of the Styrenic Comonomers

Substituent	F	Cl	Br	Me	H
Bimetallic Effect	45.4%	41.2%	31.0%	28.9%	15.4%
δ_{ipso} (ppm)	136.34	136.62	136.99	137.93	138.29

remains largely undisturbed in polar solvents such as 1,1,2,2-tetrachloroethane^{19h} ($\epsilon_r = 8.2$) and methylene chloride¹⁹ⁱ ($\epsilon_r = 9.1$).

V. Activation Studies of Model Compound $\text{Ti}_2(\text{CH}_2\text{Ph})_4$.

The design of the model compound $\text{Ti}_2(\text{CH}_2\text{Ph})_4$ is to simulate the growing polystyrene chain with the last styrene installed in a 2,1 fashion. Upon alkyl abstraction by the cocatalyst/activator $\text{B}(\text{C}_6\text{F}_5)_3$, the resulting bimetallic ion pair $[\text{Ti}_2(\text{CH}_2\text{Ph})_2]^{2+}[\text{PhCH}_2\text{B}(\text{C}_6\text{F}_5)_3]^-$ should perfectly resemble the bimetallic Ti-polymeryl propagating species. Although some neutral metal-benzyl complexes are reported to exhibit an η^n -coordination mode ($n > 1$) of the benzyl groups,³³ the model compound $\text{Ti}_2(\text{CH}_2\text{Ph})_4$ ' benzyl groups, however, engage in an η^1 -coordination mode both in solution and in the solid state, largely due to lack of coordinative unsaturation around the metal center. The significant styrene homopolymerization activity disparity between Ti_2 and Ti_1 most likely arises from, as proposed above, the preferential coordination of the phenyl ring of the last inserted styrene to the second metal center. Although definitive solution structural data (chemical shifts of the benzylic *ipso* carbons and $^1\text{J}_{\text{C-H}}$) as well as solid state structure for the bimetallic ion pair are not available to confirm the interaction of the benzylic arene to the second metal center, the present polymerization results as well as spectroscopic evidence argue at least that, in the presence of a second electrophilic metal center, minimal monometallic "back-biting" of the last inserted styrene to the parent cationic metal center occurs.

Conclusions

The results of the present study significantly expand the scope of applicable comonomers in binuclear CGC olefin polymerization catalysis. In styrene homopolymerizations, bimetallic organotitanium catalysts $(\mu\text{-CH}_2\text{-3,3'})\{(\eta^5\text{-indenyl})[1\text{-Me}_2\text{Si}(\text{tBuN})](\text{TiMe}_2)\}_2$

[MBICGC(TiMe₂)₂; **C1-Ti₂**] + Ph₃C⁺B(C₆F₅)₄⁻ (**B₁**) and (μ -CH₂CH₂-3,3') $\{\eta^5$ -indenyl)[1-Me₂Si(^tBuN)](TiMe₂)₂] [EBICGC(TiMe₂)₂; **Ti₂**] + **B₁** exhibit ~ 65 and ~ 35 times greater activities, respectively, than does monometallic [1-Me₂Si(3-ethylindenyl)(^tBuN)]TiMe₂ (**Ti₁**) + **B₁**. Bimetallic organozirconium catalysts (μ -CH₂-3,3') $\{\eta^5$ -indenyl)[1-Me₂Si(^tBuN)](ZrMe₂)₂] [MBICGC(ZrMe₂)₂; **C1-Zr₂**] + **B₁** and (μ -CH₂CH₂-3,3') $\{\eta^5$ -indenyl)[1-Me₂Si(^tBuN)](ZrMe₂)₂] [EBICGC(ZrMe₂)₂; **Zr₂**] + **B₁** exhibit ~ 8 and ~ 4 times higher activities, respectively, than does monometallic [1-Me₂Si(3-ethylindenyl)(^tBuN)]ZrMe₂ (**Zr₁**) + **B₁**. The binuclear catalysts exhibit significantly greater activities than the corresponding mononuclear catalysts, and more interestingly, as the minimum accessible distance between the adjacent metal centers decreases, this observed cooperative nuclearity effect increases in the following order: **C1-M₂** > **M₂** > **M₁** (M = Ti and Zr). In situ activation studies of model compound **Ti₂(CH₂Ph)₄** suggest that under polymerization conditions, minimal monometallic “back-biting” of the last inserted styrene to the parent cationic metal center occurs.

Increases in styrenic comonomer enchainment selectivity into the polyethylene microstructure for variously *para*-substituted styrenes are observed with binuclear catalyst **Ti₂** + **B₁** versus the corresponding mononuclear catalyst **Ti₁** + **B₁** under identical polymerization conditions. The relative magnitude of this bimetallic effect approximately mirrors the π -electron density at the *ipso* carbon: 4-fluorostyrene > 4-chlorostyrene > 4-bromostyrene > 4-methylstyrene > styrene. Polar solvation is found to play a significant role in binuclear ion pairing, affording different polymeric products while not diminishing the bimetallic effect.

The results of this study indicate that multinuclear single-site polymerization catalysts can effect unusual cooperative enchainment processes involving comonomers which possess

additional coordinating moieties and hence offer the potential of creating new macromolecular architectures which conventional monometallic catalysts can not offer.

Acknowledgement. Financial support from NSF (Grant No. CHE-0415407) is gratefully acknowledged. We thank Dr. E. Szuromi and Prof. R. F. Jordan of University of Chicago for generous help with the GPC measurements. N. G. thanks Dr. L. Li and Dr. H. Li for helpful discussions.

Chapter 2

Catalytic In Situ Synthesis of High Energy Storage Density Metal Oxide-Polyolefin Nanocomposites Using Supported Metallocenes. Systematics of Nanoparticle, Shape, and Interfacial Characteristics on Leakage Current Density, Permittivity, and Breakdown Strength

Abstract

A series of 0-3 metal oxide-polyolefin nanocomposites is synthesized via in situ olefin polymerization using the metallocene catalysts C_2 -symmetric dichloro[*rac*-ethylenebisindenyl]zirconium(IV) (EBIZrCl₂), Me₂Si(^{*t*}BuN)(η^5 -C₅Me₄)TiCl₂ (CGCTiCl₂), and (η^5 -C₅Me₅)TiCl₃ (Cp*TiCl₃) immobilized on methylaluminoxane (MAO)-treated barium titanate (BaTiO₃), zirconium dioxide (ZrO₂), 3 mol% yttria-stabilized zirconia (TZ3Y), 8 mol% yttria-stabilized zirconia (TZ8Y), *sphere*-shaped titanium dioxide (TiO₂), and *rod*-shaped TiO₂ nanoparticles. The resulting composite materials are characterized by X-ray diffraction (XRD), scanning electron microscopy (SEM), transmission electron microscopy (TEM), ¹³C nuclear magnetic resonance (NMR) spectroscopy, and differential scanning calorimetry (DSC). It is shown by TEM that the nanoparticles are well-dispersed in the polymer matrix and each individual nanoparticle is surrounded by polymer. Electrical measurements reveal that most of the nanocomposites have leakage current densities $\sim 10^{-8}$ - 10^{-6} A/cm², and the relative permittivities of the nanocomposites increase as the nanoparticle volume fraction increases, with measured values as high as 6.1. At the same volume fraction, *rod*-shaped TiO₂ nanoparticle-polypropylene nanocomposites exhibit greater relative permittivities than the corresponding *sphere*-shaped TiO₂ nanoparticle-polypropylene nanocomposites. The energy densities of these nanocomposites are estimated to be as high as 9.4 J/cm³.

Introduction

Future pulsed-power and power electronic capacitors will require dielectric materials ultimately having energy storage densities $> 30 \text{ J/cm}^3$, with operating voltages $> 10 \text{ kV}$, and $m\text{sec}-\mu\text{sec}$ charge/discharge times with reliable operation near the dielectric breakdown limit. Importantly, at 2 J/cm^3 and 0.2 J/cm^3 , respectively, the operating characteristics of current state-of-the-art pulsed power and power electronic capacitors, which utilize either ceramics or polymers as dielectric materials, remain significantly short of this goal.¹ An order of magnitude improvement in energy density will require development of revolutionary new materials that substantially increase intrinsic dielectric energy densities while operating reliably near the dielectric breakdown limit. For simple linear response dielectric materials, energy density is defined in eq. 1, where ϵ_r is relative dielectric permittivity, E is the dielectric breakdown strength, and ϵ_0 is the vacuum permittivity. Generally, inorganic metal oxides exhibit high permittivities, however, they suffer from low breakdown fields. While organic materials (e.g., polymers) can provide high breakdown strengths, their generally low permittivities have limited their application.

$$U_e = \frac{1}{2}\epsilon_r\epsilon_0E^2 \quad (1)$$

Recently, inorganic-polymer nanocomposite materials have attracted great interest due to their potential for high energy density. By integrating the complementary properties of their constituents, such materials can simultaneously derive high permittivity from the inorganic inclusions and high breakdown strength, mechanical flexibility, facile processability, light weight, and properties tunability (molecular weight, comonomer incorporation, thermal properties, etc.) from the polymer host matrix.² Additionally, there are good reasons to believe

that the large inclusion-matrix interfacial areas will afford higher polarization levels, dielectric response, and breakdown strength.³

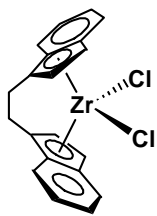
Although inorganic-polymer nanocomposites can be prepared via mechanical blending,⁴ solution mixing,⁵ in situ radical polymerization,⁶ and in situ nanoparticle synthesis,⁷ host-guest incompatibilities frequently result in nanoparticle aggregation and phase separation,⁸ which is detrimental to the electrical properties.⁹ Covalently grafting polymer chains to inorganic nanoparticle surfaces has also proven promising, leading to more effective dispersion and enhanced properties,¹⁰ however, such processes may not be cost-effective and nor easily scaled up.

In the large-scale heterogeneous or slurry olefin polymerizations practiced on a huge industrial scale, SiO₂ is generally used as the catalyst support.^{11d} Very large local hydraulic pressures arising from the growing polyolefin chains are known to effect extensive SiO₂ particle fracture and lead to SiO₂-polyolefin composites.¹¹ We therefore envisioned that in situ polymerization using metallocene catalysts supported on metal oxide nanoparticles might disrupt ubiquitous and problematic nanoparticle agglomeration to afford homogeneously dispersed ceramic nanoparticles within the matrix of a processable, high-strength commodity polymer, already used extensively in energy storage capacitors.¹²

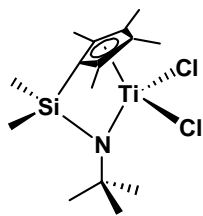
In a preliminary communication, we demonstrated that high energy density BaTiO₃- and TiO₂-isotactic polypropylene nanocomposites could be prepared via in situ metallocene polymerization.¹³ The resulting nanocomposites were found to have effective nanoparticle dispersion and to possess energy densities as high as 9.4 J/cm³, as determined from relative permittivities and dielectric breakdown measurements. In this contribution, we significantly extend the inorganic inclusion scope to include a broad variety of nanoparticles, to investigate

the effects of nanoparticle identity and shape on the electrical/dielectric properties of the resulting nanocomposites. We also extend the scope of metallocene polymerization catalysts and olefinic monomers (Chart 2-1) with the goal of achieving nanocomposites with greater processability and thermal stability. We present here a full discussion of the synthesis, structural, and electrical characterization of these nanocomposites. It will be seen that nanoparticle coating with methylaluminoxane (MAO) and subsequent in situ polymerization are crucial to achieving effective dispersion, and that breakdown strengths as high as 6.0 MV/cm, permittivities as high as 6.1, and energy storage densities as high as 9.4 J/cm³, can be realized.

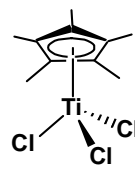
Chart 2-1. Structures of the Metallocene Catalysts and MAO



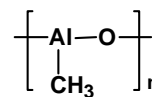
EBIZrCl₂



CGCTiCl₂



Cp*TiCl₃



MAO

Experimental Section

Materials and Methods. All manipulations of air-sensitive materials were performed with rigorous exclusion of oxygen and moisture in flamed Schlenk-type glassware on a dual-manifold Schlenk line or interfaced to a high-vacuum line (10^{-5} Torr), or in a dinitrogen-filled Vacuum Atmospheres glove box with a high capacity recirculator (<1 ppm O_2 and H_2O). Propylene (Matheson, polymerization grade) was purified by passage through a supported MnO oxygen-removal column and an activated Davison 4\AA molecular sieve column. Toluene was dried using an activated alumina column and Q-5 columns according to the method described by Grubbs,¹⁴ and was additionally vacuum-transferred from Na/K alloy and stored in Teflon-valve sealed bulbs for polymerization manipulations. $BaTiO_3$ and TiO_2 nanoparticles were kindly provided by Prof. Fatih Dogan (University of Missouri, Rolla) and Prof. Thomas Shrout (Penn State University), respectively. ZrO_2 nanoparticles were purchased from Aldrich. The reagents 3 mol% yttria-stabilized zirconia (TZ3Y) and 8 mol% yttria-stabilized zirconia (TZ8Y) nanoparticles were purchased from Tosoh, Inc. TiO_2 nanorods were purchased from Reade Advanced Materials, Riverside, RI. All of the nanoparticles were dried on a high vacuum line (10^{-5} Torr) at $80\text{ }^\circ\text{C}$ overnight to remove the surface-bound water, known to adversely affect the dielectric breakdown performance.¹⁵ The deuterated solvent 1,1,2,2-tetrachloroethane- d_2 was purchased from Cambridge Isotope Laboratories (≥ 99 atom % D) and used as received. Methylaluminoxane (MAO; Aldrich) was purified by removing all the volatiles in vacuo from a 1.0 M solution in toluene. The reagent dichloro[*rac*-ethylenebisindenyl]zirconium (IV) (**EBIZrCl₂**) was purchased from Aldrich and used as received. n^+ -Si wafers (rms roughness ≈ 0.5 nm) were obtained from Montco Silicon Tech (Spring City, PA) and cleaned according to standard procedures.¹⁶

Aluminum substrates were purchased from McMaster-Carr (Chicago, IL) and cleaned according to standard procedures.

Physical and Analytical Measurements. NMR spectra were recorded on a Varian Inova 400 (FT 400 MHz, ^1H ; 100 MHz, ^{13}C) spectrometer. Chemical shifts (δ) for ^{13}C spectra were referenced using internal solvent resonances and are reported relative to tetramethylsilane. ^{13}C NMR assays of polymer microstructure were conducted in 1,1,2,2-tetrachloroethane- d_2 containing 0.05 M $\text{Cr}(\text{acac})_3$ at 130 °C. Resonances were assigned according to the literature for stereoregular polypropylenes. Elemental analyses were performed by Midwest Microlabs, LLC, Indianapolis, Indiana. Inductively coupled plasma-optical emission spectroscopy (ICP-OES) analyses were performed by Galbraith Laboratories, Inc., Knoxville, Tennessee. The thickness of the dielectric film was measured with a Tencor P-10 step profilometer and used to calculate the dielectric constant and breakdown strength of the sample. X-ray powder diffraction patterns were recorded on a Rigaku DMAX-A diffractometer with Ni-filtered $\text{Cu K}\alpha$ radiation (1.54184 Å). Pristine ceramic nanoparticles and composite microstructures were examined with a FEI Quanta sFEG environmental scanning electron microscope with an accelerating voltage of 30 kV. Transmission electron microscopy was performed on a Hitachi H-8100 TEM with an accelerating voltage of 200 kV. Composite melting temperatures were measured on a TA Instruments 2920 temperature modulated differential scanning calorimeter. Typically, ca. 10 mg samples were examined, and a ramp rate of 10 °C/min was used to measure the melting point. To erase thermal history effects, all samples were subjected to two melt-freeze cycles. The data from the second melt-freeze cycle are presented here.

Electrical Measurements. Gold electrodes for metal-insulator-semiconductor (MIS) devices were vacuum-deposited through shadow masks at $(3-4) \times 10^{-6}$ Torr (500 Å, 0.2-0.5 Å/s). Direct current MIS leakage current measurements were performed using Keithley 6430 sub-femtoamp remote source meter and a Keithley 2400 source meter using a locally written LABVIEW program and general purpose interface bus communication. A digital capacitance meter (Model 3000, GLK Instruments, San Diego) was used for capacitance measurements. All measurements were performed under ambient conditions. Dielectric breakdown strength measurements were carried out with a high-voltage amplifier (TREK 30/20A, TREK, Inc., Medina, New York), and the experimental parameters were: ramp rate, 1,000 V/S; peak voltage, 30,000 V; ext. amplifier, 3,000; temperature, room temperature.

Immobilization of Metallocene Catalysts on Metal Oxide Nanoparticles. In the glovebox, 2.0 g nanoparticles, 200 mg MAO, and 50 mL dry toluene were loaded into a predried 100 mL Schlenk flask. Upon stirring, the mixture turned into a very fine slurry. The slurry was next subjected to alternating sonication and vigorous stirring for 2 days with constant removal of evolving CH₄. Next, the nanoparticles were collected by filtration and washed with fresh toluene (50 mL \times 4) to remove any residual MAO. Then, 200 mg metallocene catalyst was loaded in the flask with 50 mL toluene. The color of the nanoparticles immediately turned purple. The slurry mixture was again subjected to alternating sonication and vigorous stirring overnight. The nanoparticles were then collected by filtration and washed with fresh toluene until the color of the toluene remained colorless. The nanoparticles were dried on the high-vacuum line overnight and stored in the glovebox at -40 °C.

Representative Synthesis of Nanocomposites via In Situ Propylene Polymerization. In the glovebox, a 250 mL round-bottom three-neck Morton flask, which had been dried at 160 °C overnight and equipped with a large magnetic stirring bar, was charged with 50 mL dry toluene, 200 mg functionalized nanoparticles, and 50 mg MAO. The assembled flask was removed from the glovebox and the contents were subjected to sonication for 30 min with vigorous stirring. The flask was then attached to a high vacuum line (10^{-5} Torr), freeze-pump-thaw degassed, equilibrated at the desired reaction temperature using an external bath, and saturated with 1.0 atm (pressure control using a mercury bubbler) of rigorously purified propylene while vigorously stirring. After a measured time interval, the polymerization was quenched by the addition of 5 mL methanol, and the reaction mixture was then poured into 800 mL of methanol. The composite was allowed to fully precipitate overnight and was then collected by filtration, washed with fresh methanol, and dried on the high vacuum line overnight to constant weight.

Results

The goal of this study is to synthesize well-dispersed polyolefin-based nanocomposite dielectric materials via in situ supported metallocene polymerization catalysis and to investigate the effect of nanoparticle identity, loading, and shape on the electrical/dielectric properties of the resulting nanocomposites. In the first part of the Results section, we demonstrate that diverse nanocomposites can be synthesized from a variety of olefin monomers using identical in situ polymerization methodologies. Next, we present the microstructural studies of the nanocomposites, illustrating that nanoparticle agglomeration can be satisfactorily disrupted with the in situ approach. In the remaining parts of the section, we discuss the effect of nanoparticle

identity, volume fraction, and shape on the nanocomposite leakage current density, relative permittivity, breakdown strength, and energy storage density.

I. Synthesis of Metal Oxide-Polyolefin Nanocomposites

As one of the most commonly used polymers in large-scale power capacitors, isotactic polypropylene offers greater stiffness, lower shrinkage, and less deterioration of the dielectric properties at higher temperatures than other grade polypropylenes.¹² Therefore, the C_2 -symmetric metallocene catalyst dichloro[*rac*-ethylenebisindenyl]zirconium(IV) (EBIZrCl₂), known for highly isospecific olefin polymerization, was selected for immobilization on the surfaces of MAO-treated metal oxide nanoparticles, to synthesize metal oxide-isotactic polypropylene nanocomposites (Scheme 2-1).

The resulting nanocomposites were characterized by a full complement of spectroscopic and analytical methodologies. X-ray diffraction (XRD) linewidth analyses using the Scherrer equation¹⁷ indicate that the microstructures and coherence lengths of the individual nanoparticles remain largely unchanged upon deagglomeration (Table 2-1). ¹³C NMR spectroscopy (Figure 2-1) shows that the present polypropylenes are highly isotactic, as evidenced by the isotacticity index ($[mmmm] = 83\%$).¹⁸ DSC confirms the absence of extensive amorphous regions in the composites since only isotactic polypropylene melting features (142-147 °C) are detected.¹⁹ XRD data for the nanocomposites also reveal the presence of monoclinic α phase crystalline isotactic polypropylene ($2\theta = 14.2, 17.0, 18.6, \text{ and } 21.8^\circ$).²⁰ Interestingly, it is found that the melting temperatures of the nanocomposites generally increase as the nanoparticle loading increases (Table 2-2), likely due to attractive interactions between the nanoparticles and the crystalline regions of the isotactic polypropylene.²¹

Scheme 2-1. Synthesis of Isotactic Polypropylene-Metal Oxide Nanocomposites

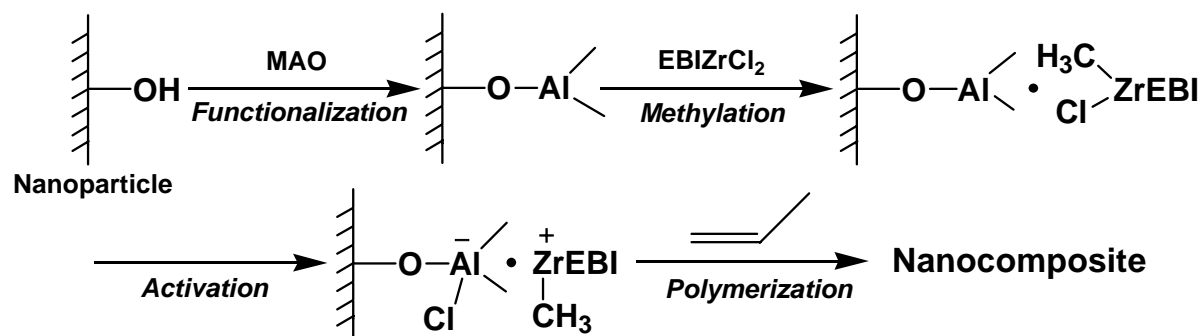


Figure 2-1. ^{13}C NMR spectrum of an isotactic-polypropylene nanocomposite (100 MHz, $\text{C}_2\text{D}_2\text{Cl}_4$, 130 °C).

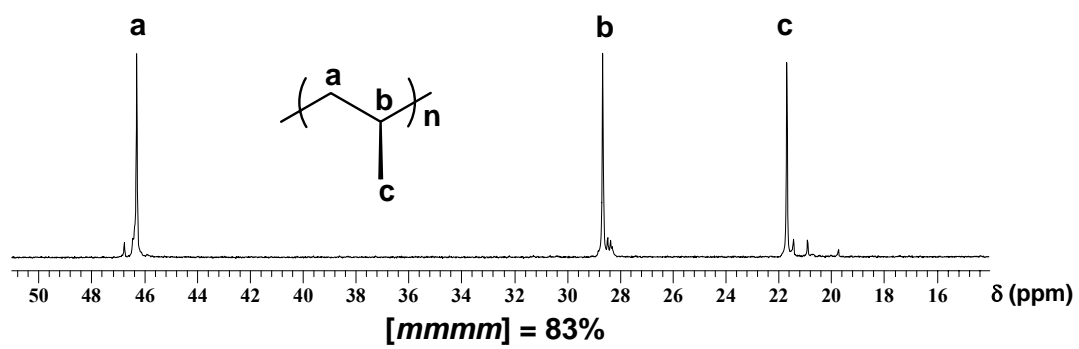


Table 2-1. XRD Linewidth Analysis Results of the Nanocomposites

Powder	2θ (deg)	FWHM (deg)	Crystallite Size (nm)
BaTiO ₃ -polypropylene	31.649	0.271	32.8
BaTiO ₃	31.412	0.254	35.6
TiO ₂ -polypropylene	25.358	0.361	23.5
TiO ₂	25.360	0.317	27.1

Crystallite size (L) is calculated using the Scherrer equation $L = 0.9\lambda/B\cos\theta_B$ (λ = x-ray wavelength, B = full-width-at-half maximum (FWHM) of the diffraction peak, and θ_B = Bragg angle).

Linear low-density polyethylene (LLDPE) is another polymer that is widely used in power capacitors. Compared to isotactic polypropylene, the chain branching in the LLDPE affords better processability.²² Therefore, the sterically open constrained geometry catalyst $\text{Me}_2\text{Si}(\text{tBuN})(\eta^5\text{-C}_5\text{Me}_4)\text{TiCl}_2$ (CGCTiCl₂)²³ is utilized in the present study to synthesize BaTiO₃-LLDPE nanocomposites via in situ ethylene + 1-octene copolymerization.²³ Figure 2-2 presents a representative ¹³C NMR spectrum of the nanocomposite, with the 1-octene incorporation level calculated to be 25.0 mol%.²⁴ DSC measurements also confirms the formation of LLDPE, which has a typical melting temperature of 125.3 °C.²²

Syndiotactic polystyrene has greater heat resistance²⁵ than isotactic polypropylene, which can only operate below 85 °C when incorporated into film capacitors.¹² Employing the same protocol as EBIZrCl₂, the half-metallocene catalyst Cp*TiCl₃²⁵ was immobilized on MAO-treated ZrO₂ nanoparticles. Subsequent in situ styrene polymerization affords ZrO₂-syndiotactic polystyrene nanocomposites. A representative ¹³C NMR spectrum is shown in Figure 2-3. The characteristic single resonance near $\delta = 145.6$ ppm for the *ipso* phenyl carbon atom confirms the production of syndiotactic polystyrene,²⁵ which is further substantiated by the melting temperature (267.0 °C) as measured by DSC.²⁵

Figure 2-2. ^{13}C NMR spectrum of a poly(ethylene-*co*-1-octene) nanocomposite (100 MHz, $\text{C}_2\text{D}_2\text{Cl}_4$, 130 °C).

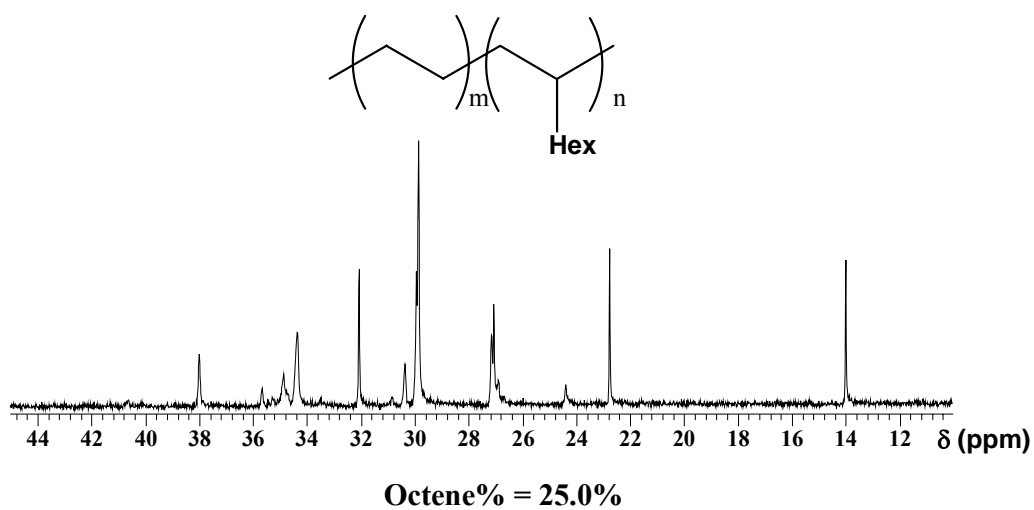
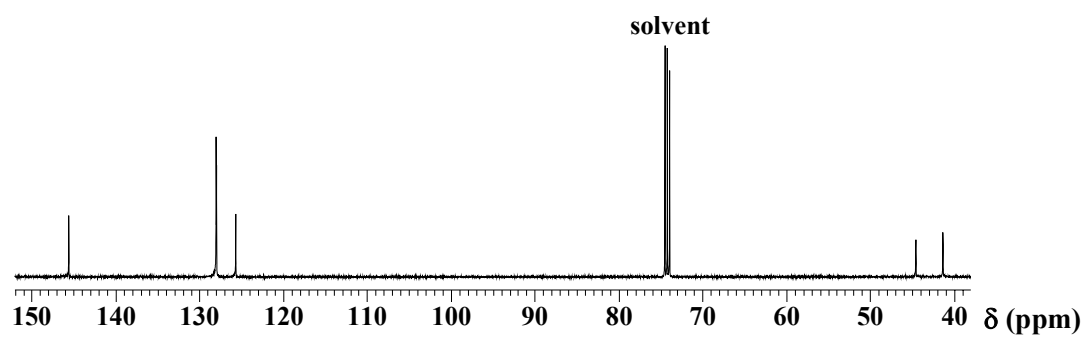


Figure 2-3. ^{13}C NMR spectrum of a syndiotactic-polystyrene nanocomposite (100 MHz, $\text{C}_2\text{D}_2\text{Cl}_4$, 130 °C).



II. Nanocomposite Microstructural Properties

During the course of in situ metallocene polymerization, the polymer chains propagating at the nanoparticle-immobilized metallocene catalytic centers are expected to create large local hydrostatic pressures¹¹ and thus help to disrupt the nanoparticle agglomeration. This is confirmed by the comparative electron microscopic characterization of the as-received pristine nanoparticles and the resulting nanocomposites. As can be seen from Figures 2-4, 2-5, and 2-6, the as-received pristine nanoparticles evidence very high levels of agglomeration, however, for the polyolefin nanocomposites, the agglomeration of the nanoparticles is shown to be disrupted and each individual nanoparticle is surrounded by a layer of matrix polymer.

III. Nanocomposite Permittivity Properties

Metal-insulator-metal (MIM) or metal-insulator-semiconductor (MIS) devices for nanocomposite electrical measurements were fabricated by first doctor-blading nanocomposite films onto aluminum or n⁺-Si substrates, followed by vacuum-depositing top gold electrodes through shadow masks. The capacitances were measured at 1 kHz, a sufficiently high frequency to avoid the complications arising from conduction and interfacial polarization effects.²⁶ After the capacitance was measured at multiple locations on the nanocomposite film surface using different electrode areas, the relative permittivity (ϵ_r) of the nanocomposite was derived using eq. 2, where C is the capacitance, A is the electrode area, ϵ_0 is the vacuum permittivity (8.8542×10^{-12} F/m), ϵ_r is relative permittivity, and d is the nanocomposite film thickness. Figure 2-7 shows a representative capacitance vs. electrode area plot, the linearity of which indicates the good dielectric *uniformity* of the nanocomposite film.

$$C = \frac{\epsilon_0 \epsilon_r A}{d} \quad (2)$$

Figure 2-4. Electron microscopic characterization of: (a) as-received pristine ZrO_2 (SEM) and (b) 7.4 vol% ZrO_2 -*iso*PP nanocomposite (TEM).

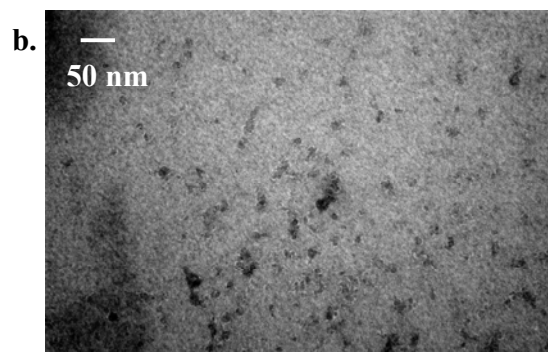
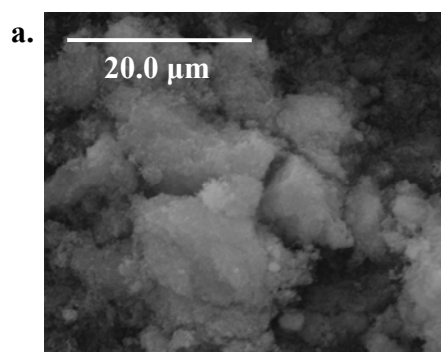


Figure 2-5. Electron microscopic characterization of: (a) as-received pristine TZ3Y (SEM) and (b) 31.1 wt% TZ3Y-*iso*PP nanocomposite (TEM).

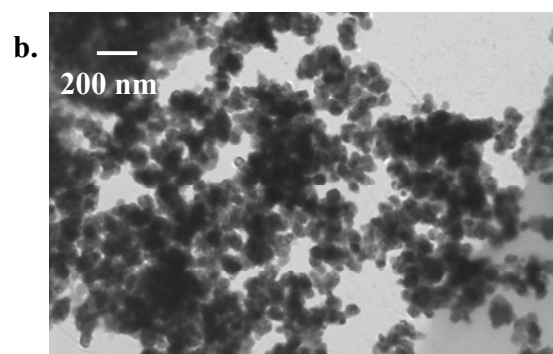
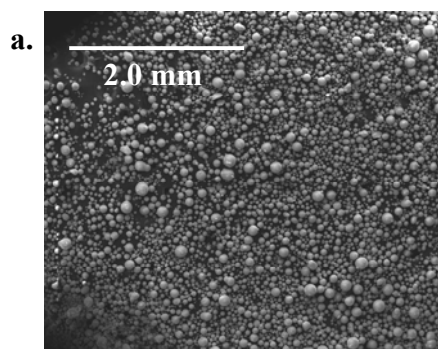


Figure 2-6. Electron microscopic characterization of: (a) as-received pristine TZ8Y (SEM) and (b) 39.2 wt% TZ8Y-*iso*PP nanocomposite (TEM).

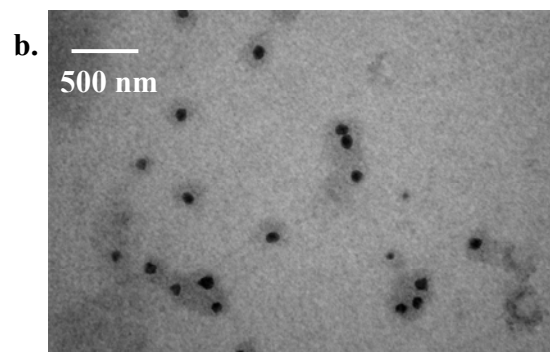
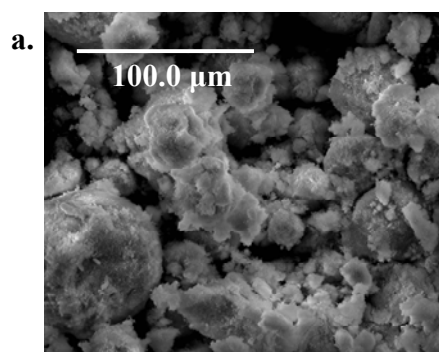


Figure 2-7. Representative C (capacitance) vs. A (electrode area) plot for a 2.6 vol% BaTiO₃-^{iso}PP nanocomposite.

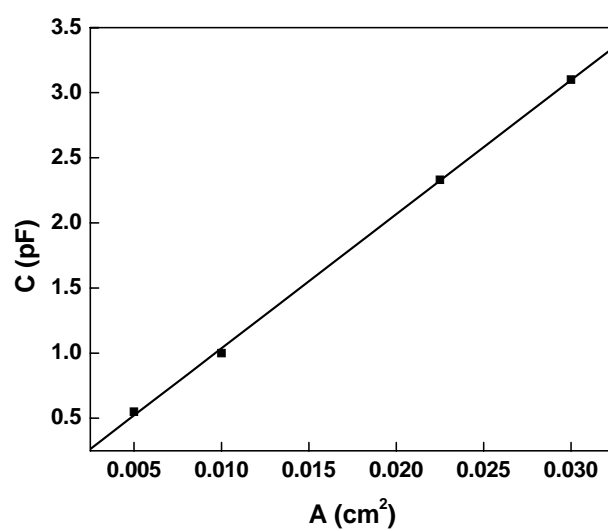


Table 2-2 summarizes the relative permittivity measurement results for the present nanocomposites. As the nanoparticle loading increases, the relative permittivity of the nanocomposites also increases as predicted by the effective medium approximation (see more below).²⁷ More interestingly, at the same volume fraction, *rod*-shaped TiO₂-polypropylene nanocomposites exhibit significantly greater relative permittivities than those prepared with *sphere*-shaped TiO₂ nanoparticles (compare entries 1-4 versus 11-13) under identical reaction conditions. This shape effect is thought to arise from the different depolarization factors for different inclusion particle geometries (see more below).

IV. Leakage Current Density Measurement Results

The leakage current densities of all the nanocomposite films prepared in this investigation (Figures 2-8 and 2-9) are mostly within the range $10^{-8} - 10^{-6}$ A/cm² at 100 V, indicating that the aforementioned nanocomposites are all excellent insulators. As the nanoparticle loading increases, most of the nanocomposites exhibit lower leakage current densities, presumably a result of modified charge transport and interruption of the crystalline conduction pathways within the composite structure (see more below).²⁸ However, at the highest nanoparticle loadings, the nanocomposites have the largest leakage current densities, simply because the weight percentages of the nanoparticles have reached the respective percolation thresholds. Notably, increasing the relative permittivity of the nanocomposite by changing the shape of the inclusion does not compromise the good insulating properties of these composites.

V. Breakdown Strength Measurements and Nanocomposite Energy Density

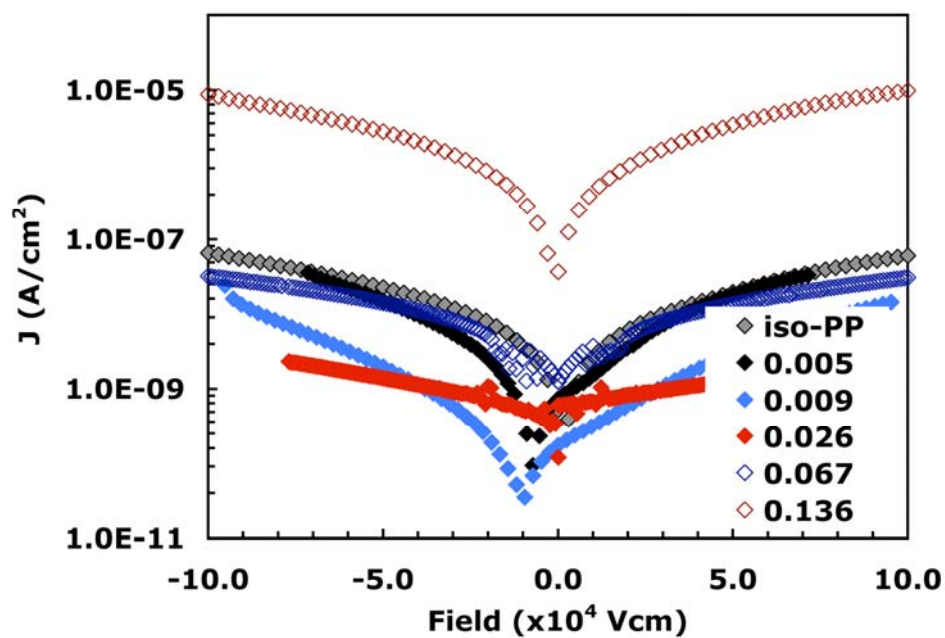
Table 2-2. Electrical Characterization Results for Metal Oxide-polypropylene Nanocomposites^a

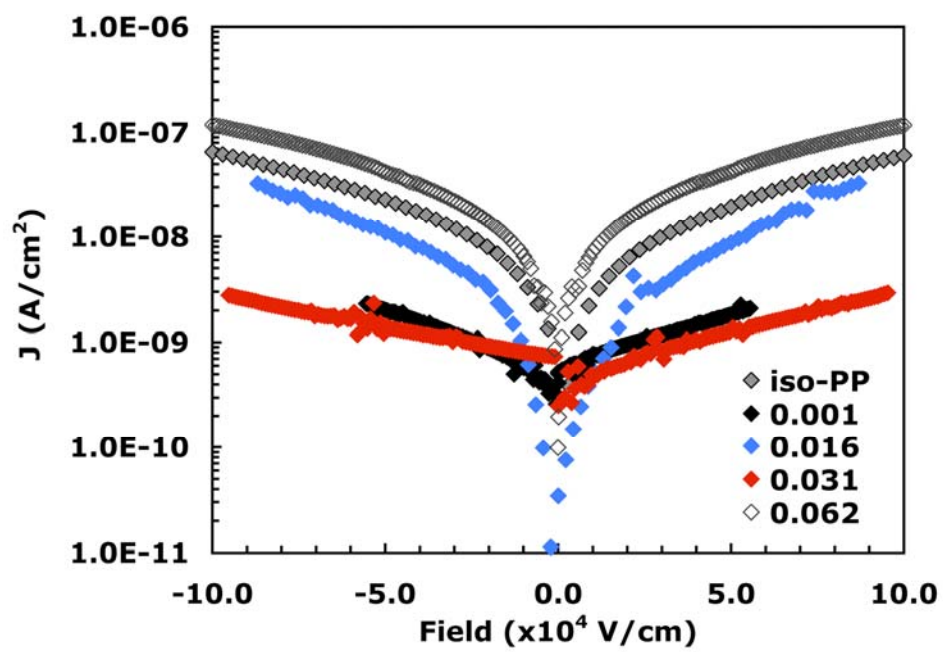
Entry	Composite	Nanoparticle wt % ^b	T _m ^c (°C)	Permittivity ^d	Breakdown Field (kV)	Film Thickness ^e (μm)	Energy Density ^f (J/cm ³)
1	<i>iso</i> PP- <i>s</i> TiO ₂	0.4 %	135.2	2.2 ± 0.1	> 10.0	36	>0.8 ± 0.1
2	<i>iso</i> PP- <i>s</i> TiO ₂	7.0 %	142.4	2.8 ± 0.2	9.5	23	2.1 ± 0.2
3	<i>iso</i> PP- <i>s</i> TiO ₂	12.6 %	142.6	2.8 ± 0.1	7.5	27	1.0 ± 0.1
4	<i>iso</i> PP- <i>s</i> TiO ₂	22.9 %	144.8	3.0 ± 0.2	9.3	20	2.8 ± 0.2
5	<i>iso</i> PP-BaTiO ₃	2.9 %	136.8	2.7 ± 0.1	8.8	28	1.2 ± 0.1
6	<i>iso</i> PP-BaTiO ₃	5.4 %	142.8	3.1 ± 1.2	> 10.0	21	>4.0 ± 0.6
7	<i>iso</i> PP-BaTiO ₃	14.3 %	142.1	2.7 ± 0.2	9.8	25	1.8 ± 0.2
8	<i>iso</i> PP-BaTiO ₃	25.7 %	145.6	2.9 ± 1.0	8.2	30	1.0 ± 0.3
9	<i>iso</i> PP-BaTiO ₃	30.8 %	144.8	5.1 ± 1.7	9.0	22	3.7 ± 1.2
10	<i>iso</i> PP-BaTiO ₃	50.8 %	144.8	6.1 ± 0.9	> 10.0	17	>9.4 ± 1.3
11	<i>iso</i> PP- <i>r</i> TiO ₂	6.1%	139.7	3.4 ± 0.3			
12	<i>iso</i> PP- <i>r</i> TiO ₂	12.8%	142.4	4.1 ± 0.7			
13	<i>iso</i> PP- <i>r</i> TiO ₂	19.4%	143.7	4.9 ± 0.4			
14	<i>iso</i> PP-ZrO ₂	9.0%	142.9	1.7 ± 0.3			
15	<i>iso</i> PP-ZrO ₂	19.5%	145.2	2.0 ± 0.4			
16	<i>iso</i> PP-ZrO ₂	32.3%	144.9	4.8 ± 1.1			
17	<i>iso</i> PP-ZrO ₂	9.4%	144.4	5.1 ± 1.3			
18	<i>iso</i> PP-TZ3Y	6.7%	142.9	1.1 ± 0.1			
19	<i>iso</i> PP-TZ3Y	16.8%	143.5	1.8 ± 0.2			
20	<i>iso</i> PP-TZ3Y	22.0%	143.8	2.0 ± 0.2			
21	<i>iso</i> PP-TZ3Y	31.1%	144.9	2.7 ± 0.2			
22	<i>iso</i> PP-TZ8Y	5.9%	142.9	1.4 ± 0.1			
23	<i>iso</i> PP-TZ8Y	15.3%	143.2	1.8 ± 0.1			
24	<i>iso</i> PP-TZ8Y	21.3%	143.2	2.0 ± 0.2			
25	<i>iso</i> PP-TZ8Y	39.2%	146.2	2.4 ± 0.4			

^a Polymerizations carried out in 50 mL of toluene under 1.0 atm of propylene at 20 °C. ^b From elemental analysis. ^c From differential scanning calorimetry. ^d Derived from capacitance measurement. ^e Film thicknesses measured using profilometry. ^f Energy density (U) calculated from $U = 0.5\epsilon_0\epsilon_r E_b^2$ (ϵ_0 , vacuum permittivity; ϵ_r , relative permittivity; and E_b , breakdown field (MV/cm) calculated by dividing breakdown voltage by film thickness).

Figure 2-8. Leakage current density vs. field measurement results for the nanocomposite MIS or MIM devices (legends are for the volume fraction of the inorganic particles): (a) n^+ -Si/BaTiO₃-polypropylene/Au; (b) n^+ -Si/*sphere*-TiO₂-polypropylene/Au; (c) Al/*rod*-TiO₂-polypropylene/Au.

a.



b.

c.

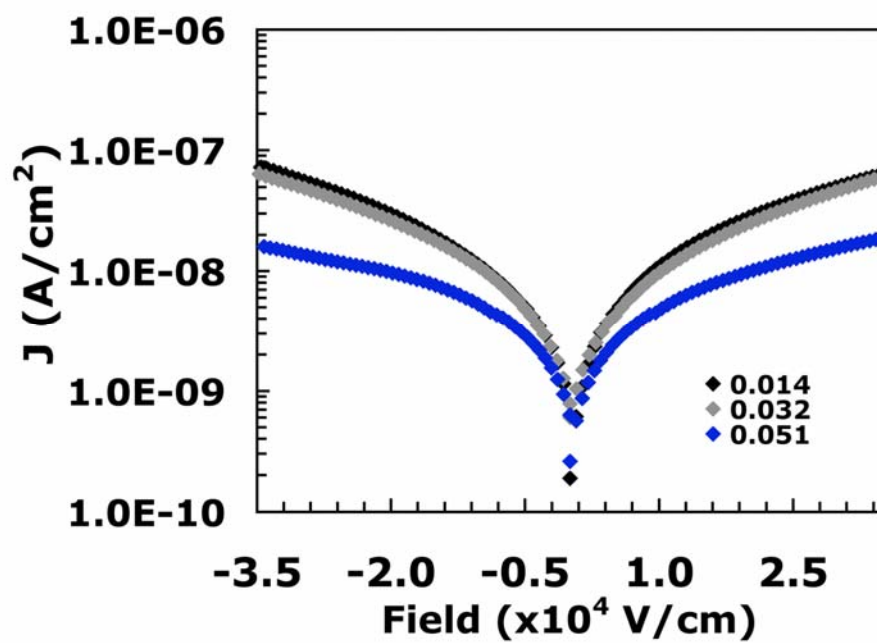
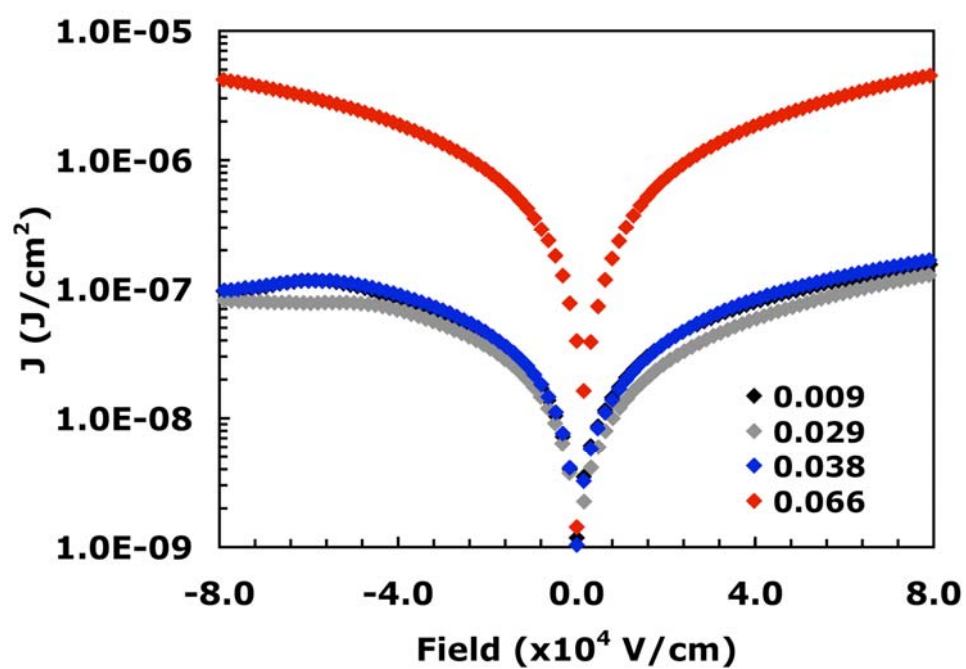
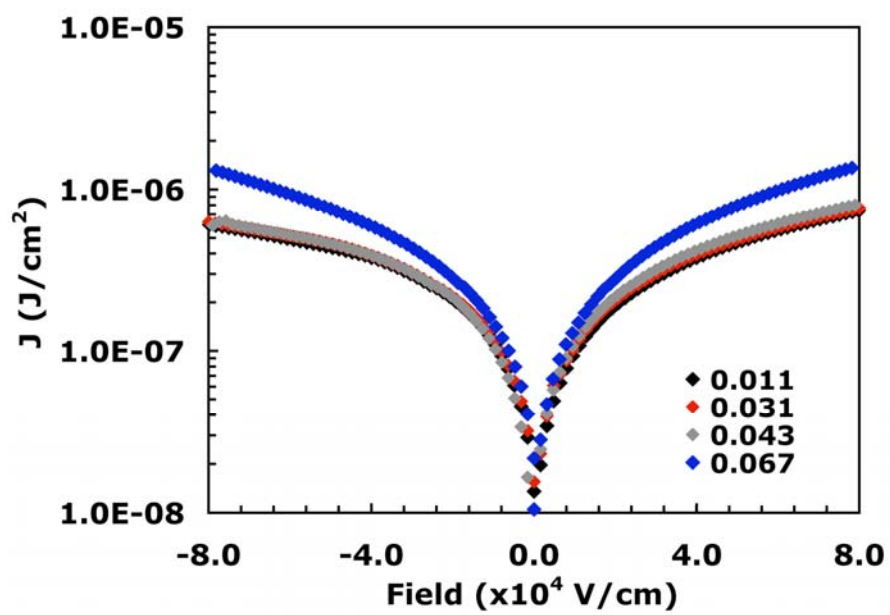


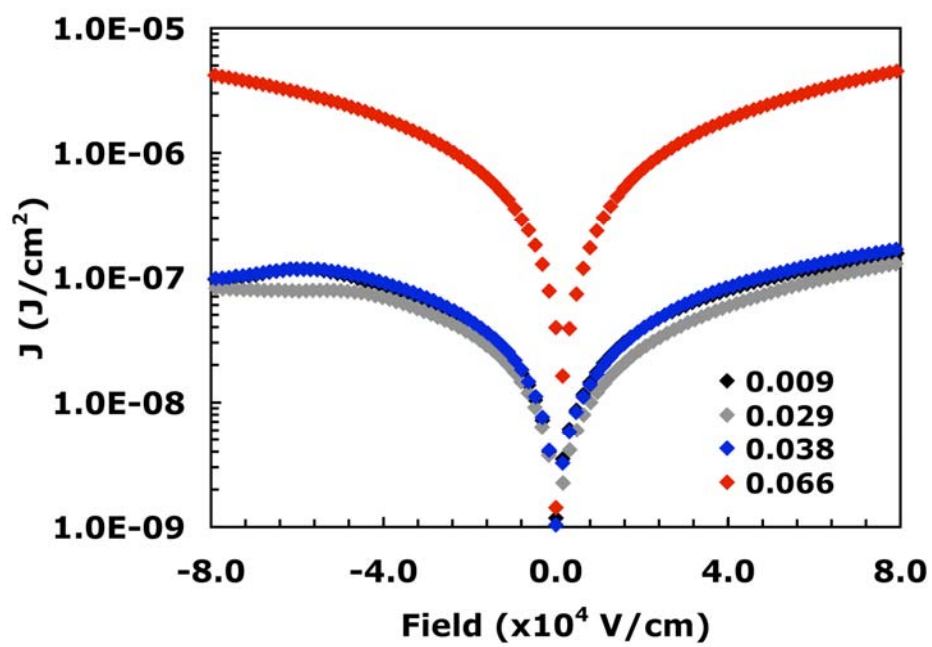
Figure 2-9. Leakage current density vs. field measurement results for the nanocomposite MIS or MIM devices (legends are for the volume fraction of the inorganic particles): (a) Al/ZrO₂-polypropylene/Au; (b) Al/TZ3Y-polypropylene/Au; (c) Al/TZ8Y-polypropylene/Au.

a.



b.

c.



The present measured breakdown strengths for some of the nanocomposites are invariably $\sim 3\text{-}6$ MV/cm, indicating that metal oxide nanoparticle inclusion does not significantly depress the polymer dielectric breakdown strength. We speculate that, in a well-dispersed nanoparticle composite, interfaces between the ceramic nanoparticles and polymer phases create effective electron scatterers and trapping centers, thus reducing the breakdown probability (see more in the Discussion section).²⁹ Moreover, well-dispersed ceramic nanoparticles should block degradation tree growth and thus increase the long-term breakdown strength.³⁰ Energy densities of the present nanocomposites are estimated to be as high as 9.4 J/cm^3 , which rivals or exceeds those reported for conventional ceramic,³¹ polymer,³² and composite³³ dielectrics.

Discussion

I. Nanocomposite Synthesis and Characterization

A key challenge in the preparation of inorganic metal oxide-polyolefin nanocomposites is the general phase incompatibility between inorganic polar metal oxide inclusions and the non-polar organic host materials. For example, ferroelectric metal oxides are highly hydrophilic, while isotactic polypropylene is highly hydrophobic. Simple admixing of the two constituents negligibly disrupts the extensive nanoparticle agglomeration nor affects the *um*-scale or larger phase separation, which can lead to local dielectric breakdown and degrade the nanocomposite electrical properties.⁹ In contrast, the present in situ supported metallocene polymerization approach minimizes these deficiencies by achieving homogeneous nanoscale dispersion of the metal oxide phase: each individual nanoparticle is surrounded by polymer chains propagating in situ from the surface-immobilized metallocenium catalyst centers, and thus offers improved dielectric properties (energy densities as high as 9.4 J/cm^3).

II. Function of the Cocatalyst MAO

In nanocomposites having very large contrasts in relative permittivities between host and guest materials, this leads to a large disparity in the electric fields within the constituent phases, thus preventing the realization of maximum energy densities for both constituents simultaneously. For BaTiO₃-polypropylene nanocomposites, however, the achieved energy density is as high as 9.4 J/cm³ although the materials permittivity ratio approaches ~ 1000:1. We speculate that, the Al₂O₃ ($\epsilon_r \approx 10$) layer (thickness ~ 1 nm, estimated from ICP-OES analysis) evolving from ambient exposure of the MAO coating, acts as a dielectric buffer layer between the high permittivity BaTiO₃ nanoparticles ($\epsilon_r \approx 2000$) and low permittivity polypropylene ($\epsilon_r \approx 2.2$).

III. Effect of Nanoparticle Shape on Nanocomposite Permittivity

The most common effective medium models are derived for the simple case of a spherical dielectric inclusion embedded in a sphere of the host material. However, most materials do not occur naturally as spheres, and therefore effective medium models for other shapes have also been developed.^{34,35} Simple analytical solutions for the effective permittivity (ϵ_{eff}) can be derived only for ellipsoids, whereas all other shapes require numerical solutions. Depolarization factors along each semi-axis of the ellipsoid (N_x, N_y, N_z), where $N_x = N_y = N_z = 1$, are used to estimate geometrical effects. The depolarization factors are calculated from integrals, e.g., eq. 3, where a_x, a_y, a_z are the semi-axes of the ellipsoid. For spheres, all three depolarization factors are

$$N_x = \frac{a_x a_y a_z}{2} \int_0^\infty \frac{1}{(s + a_x^2) \sqrt{(s + a_x^2)(s + a_y^2)(s + a_z^2)}} ds \quad (3)$$

equal (1/3, 1/3, 1/3), however, for ellipsoids the depolarization factors are, 0, 1/2, 1/2, respectively and for discs, 1, 0, 0, respectively. Since the dielectric energy is a stationary

functional of the electric field, the result is that permittivities arising from spherical inclusions are the lowest and any deviation from the spherical shape results in an increase in the effective permittivity of the mixture at the same volume fraction. These observations³⁶ motivated the present study of TiO₂-isotactic polypropylene nanocomposites with different inclusion shapes.

In Figure 2-10 we compare the calculated effective permittivities of the nanocomposites containing spherical inclusions to the nanocomposites with ellipsoidal inclusions. For the case of spherical inclusions, the effective permittivities are calculated using the Maxwell-Garnett

$$\varepsilon_{eff} = \varepsilon_b \frac{\varepsilon_a + 2\varepsilon_b + 2f_a(\varepsilon_a - \varepsilon_b)}{\varepsilon_a + 2\varepsilon_b - f_a(\varepsilon_a - \varepsilon_b)} \quad (4)$$

$$\varepsilon_{eff} = \varepsilon_b + \frac{f_a}{3}(\varepsilon_a - \varepsilon_b) \sum_{j=x,y,z} \frac{\varepsilon_{eff}}{\varepsilon_{eff} + N_j(\varepsilon_a - \varepsilon_{eff})} \quad (5)$$

effective medium theory (eq. 4),³⁷ and for the case of ellipsoidal inclusions, the effective permittivities are calculated using the Polder-Van Santen formalism (eq. 5), where ε_a is the relative permittivity of the TiO₂ inclusions, ε_b is the relative permittivity of isotactic polypropylene, f_a is the volume fraction of TiO₂ in the polymer, and N_j is for the depolarization factors.²⁷ As expected, the effective medium theory predicts that composites containing ellipsoidal inclusions will have larger effective permittivities at low volume loadings than composites containing spherical inclusions.

The experimental results are plotted in Figure 2-11. Remarkably, the effective permittivities for spherical inclusions remain constant over a small range of volume fractions, exactly as the Maxwell-Garnett equation predicts (Figure 2-10). In marked contrast, the effective permittivity of composites having inclusions with ellipsoidal shapes increases rapidly with increasing inclusion volume fraction, which is again similar to trend predicted for ellipsoidal

Figure 2-10. Normalized effective permittivity ($\epsilon_{eff} - \epsilon_b / \epsilon_a - \epsilon_b$) for composite dielectrics of polypropylene with spherical inclusions (eq. 4), and with ellipsoidal inclusions (eq. 5).

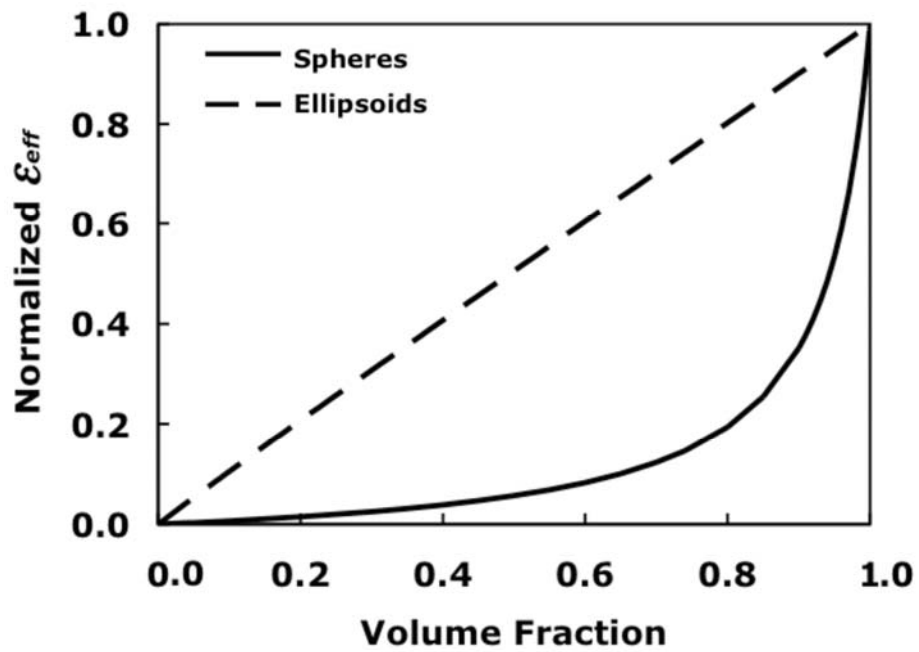
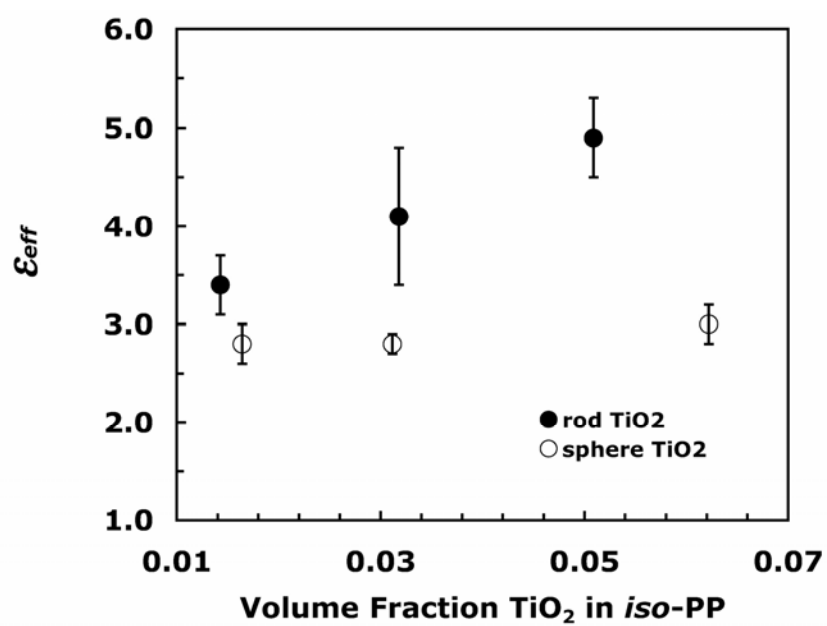


Figure 2-11. Comparison of effective permittivities for spherical- and rod-shaped TiO₂ nanoparticle-polypropylene nanocomposites.



inclusions using eq. 5 (Figure 2-10).

Conclusions

We have synthesized and microstructurally/electrically characterized a series of well-dispersed metal oxide-polyolefin nanocomposites via a scalable, in situ supported metallocene olefin polymerization process. Leakage current densities $\sim 10^{-8}$ - 10^{-6} A/cm² suggest that the nanocomposites are excellent insulators. The relative permittivity of the nanocomposites increases as the nanoparticle fraction increases. At the same inclusion loading, *rod*-shaped TiO₂ nanoparticle-polypropylene nanocomposites exhibit significantly greater relative permittivities than *sphere*-shaped TiO₂ nanoparticle-polypropylene nanocomposites. Energy densities of the BaTiO₃-polypropylene nanocomposites are found to be as high as 9.4 J/cm³. This versatile approach offers effective control over composite composition and ready scalability. That is, simply by varying nanoparticle identity as well as their sizes, shapes, and the metallocene catalysts used, a wide array of nanocomposites with desired dielectric and mechanical properties can thus be catalytically synthesized in situ.

Acknowledgement. This research was supported by ONR (N00014-05-1-0766) and made use of Central Facilities supported by the MRSEC program of the National Science Foundation (DMR-0520513) at the Materials Research Center of Northwestern University. The SEM and TEM analyses were performed in the EPIC facility of the NUANCE Center at Northwestern University. The NUANCE Center is supported by NSF-NSEC, NSF-MRSEC, Keck Foundation, the State of Illinois, and Northwestern University. We thank Mr. M. Russell for assistance in SEM measurements. We also thank Dr. A. Facchetti for helpful discussions.

REFERENCES AND NOTES

Chapter 1

- (1) (a) Collman, J. P.; Boulatov, R.; Sunderland, C. J.; Fu, L. *Chem. Rev.* **2004**, *104*, 561-588. (b) Krishnan, R.; Voo, J. K.; Riordan, C. G.; Zahkarov, L.; Rheingold, A. L. *J. Am. Chem. Soc.* **2003**, *125*, 4422-4423. (c) Bruice, T. C. *Acc. Chem. Res.* **2002**, *35*, 139-148. (d) Bruice, T. C.; Benkovic, S. J. *Biochemistry* **2000**, *39*, 6267-6274 and references therein. (e) O'Brien, D. P.; Entress, R. M. N.; Matthew, A. C.; O'Brien, S. W.; Hopkinson, A.; Williams, D. H. *J. Am. Chem. Soc.* **1999**, *121*, 5259-5265. (f) Carazo-Salas, R. E.; Guarguaglini, G.; Gruss, O. J.; Segref, A.; Karsenti, E.; Mattaj, L. W. *Nature* **1999**, *400*, 178-181. (g) Menger, F. M. *Acc. Chem. Res.* **1993**, *26*, 206-212 and references therein. (h) Page, M. I. In *The Chemistry of Enzyme Action*; Page, M. I., Ed.; Elsevier: New York, 1984; pp 1-54.
- (2) (a) Sammis, G. M.; Danjo, H.; Jacobsen, E. N. *J. Am. Chem. Soc.* **2004**, *126*, 9928-9929. (b) Moore, D. R.; Cheng, M.; Lobkovsky, E. B.; Coates, G. W. *J. Am. Chem. Soc.* **2003**, *125*, 11911-11924. (c) Trost, B. M.; Mino, T. *J. Am. Chem. Soc.* **2003**, *125*, 2410-2411. (d) Jacobsen, E. N. *Acc. Chem. Res.* **2000**, *33*, 421-431. (e) Molenveld, P.; Engbersen, J. F. J.; Reinhoudt, D. N. *Chem. Soc. Rev.* **2000**, *29*, 75-86. (f) Konsler, R. G.; Karl, J.; Jacobsen, E. N. *J. Am. Chem. Soc.* **1998**, *120*, 10780-10781. (g) Molenveld, P.; Kapsabelis, S.; Engbersen, J. F. J.; Reinhoudt, D. N. *J. Am. Chem. Soc.* **1997**, *119*, 2948-2949. (h) Mathews, R. C.; Howell, D. H.; Peng, W.-J.; Train, S. G.; Treleaven, W. D.; Stanley, G. G. *Angew. Chem., Int. Ed. Engl.* **1996**, *35*, 2253-2256. (i) Sawamura, M.; Sudoh, M.; Ito, Y. *J. Am. Chem. Soc.* **1996**, *118*, 3309-3310.
- (3) For recent reviews of single-site olefin polymerization, see: (a) Marks, T. J. *Proc. Natl. Acad. Sci. U.S.A* **2006**, *103* (Special Feature on Polymerization). (b) Li, H.; Marks, T. J.

- Proc. Natl. Acad. Sci. U.S.A* **2006**, *103*, 15295-15302. (c) Severn, J. R.; Chadwick, J. C.; Duchateau, R.; Friederichs, N. *Chem. Rev.* **2005**, *105*, 4073-4147. (d) Kaminsky, W. *J. Polym. Sci., Part A: Polym. Chem.* **2004**, *42*, 3911-3921. (e) Gibson, V. C.; Spitzmesser, S. K. *Chem. Rev.* **2003**, *103*, 283-316. (f) Pédeutour, J.-N.; Radhakrishnan, K.; Cramail, H.; Deffieux, A. *Macromol. Rapid Commun.* **2001**, *22*, 1095-1123. (g) Gladysz, J. A. *Chem. Rev.* **2000**, *100*, (special issue on Frontiers in Metal-Catalyzed Polymerization). (h) Marks, T. J.; Stevens, J. C. *Top. Catal.* **1999**, *15*, and references therein. (i) Britovsek, G. J. P.; Gibson, V. C.; Wass, D. F. *Angew. Chem. Int. Ed.* **1999**, *38*, 428-447. (j) Kaminsky, W.; Arndt, M. *Adv. Polym. Sci.* **1997**, *127*, 144-187. (k) Bochmann, M. *J. Chem. Soc., Dalton Trans.* **1996**, 255-270. (l) Brintzinger, H.-H.; Fischer, D.; Mülhaupt, R.; Rieger, B.; Waymouth, R. M. *Angew. Chem. Int. Ed.* **1995**, *34*, 1143-1170. (m) *Catalyst Design for Tailor-Made Polyolefins*; Soga, K., Terano, M., Eds.; Elsevier: Tokyo, **1994**. (n) Marks, T. J. *Acc. Chem. Res.* **1992**, *25*, 57-65.
- (4) For constrained-geometry catalysts, see: (a) Iedema, P. D.; Hoefsloot, H. C. J. *Macromolecules* **2003**, *36*, 6632-6644. (b) Klosin, J.; Kruper, W. J., Jr.; Nickias, P. N.; Roof, G. R.; De Waele, P.; Abboud, K. A. *Organometallics* **2001**, *20*, 2663-2665. (c) McKnight, A. L.; Waymouth, R. M. *Chem. Rev.* **1998**, *98*, 2587-2598. (d) Lai, S. Y.; Wilson, J. R.; Knight, G. W.; Stevens, J. C. *WO-93/08221*, **1993**.
- (5) (a) Li, H.; Li, L.; Schwartz, D. J.; Metz, M. V.; Marks, T. J.; Liable-Sands, L.; Rheingold, A. L. *J. Am. Chem. Soc.* **2005**, *127*, 14756-14768. (b) Li, H.; Stern, C. L.; Marks, T. J. *Macromolecules* **2005**, *38*, 9015-9027. (c) Li, H.; Li, L.; Marks, T. J. *Angew. Chem. Int. Ed.* **2004**, *37*, 4937-4940. (d) Wang, J.; Li, H.; Guo, N.; Li, L.; Stern, C. L.; Marks, T. J. *Organometallics* **2004**, *23*, 5112-5114. (e) Guo, N.; Li, L.; Marks, T. J. *J. Am. Chem. Soc.*

- 2004**, *126*, 6542-6543. (f) Li, H.; Li, L.; Marks, T. J.; Liable-Sands, L.; Rheingold, A. L. *J. Am. Chem. Soc.* **2003**, *125*, 10788-10789. (g) Abramo, G. P.; Li, L.; Marks, T. J. *J. Am. Chem. Soc.* **2002**, *124*, 13966-13967. (h) Li, L.; Metz, M. V.; Li, H.; Chen, M.-C.; Marks, T. J.; Liable-Sands, L.; Rheingold, A. L. *J. Am. Chem. Soc.* **2002**, *124*, 12725-12741.
- (6) (a) Scherer, W.; McGrady, G. S. *Angew. Chem. Int. Ed.* **2004**, *43*, 1782-1806. (b) Prosenc, M. H.; Brintzinger, H. H. *Organometallics* **1997**, *16*, 3889-3894. (c) Grubbs, R. H.; Coates, G. W. *Acc. Chem. Res.* **1996**, *29*, 85-93. (d) Prosenc, M. H.; Janiak, C.; Brintzinger, H. H. *Organometallics* **1992**, *11*, 4036-4041. (e) Cotter, W. D.; Bercaw, J. E. *J. Organomet. Chem.* **1991**, *417*, C1-C6. (f) Krauledat, H.; Brintzinger, H. H. *Angew. Chem. Int. Ed. Engl.* **1990**, *29*, 1412-1413. (g) Piers, W. E.; Bercaw, J. E. *J. Am. Chem. Soc.* **1990**, *112*, 9406-9407. (h) Brookhart, M.; Green, M. L. H.; Wong, L. L. *Prog. Inorg. Chem.* **1988**, *36*, 1-124. (i) Clawson, L.; Soto, J.; Buchwald, S. L.; Steigerwald, M. L.; Grubbs, R. H. *J. Am. Chem. Soc.* **1985**, *107*, 3377-3378.
- (7) Motta, A.; Fragala, I. L.; Marks, T. J. "Theoretical Investigation of Proximity Effects in Binuclear Catalysts for Olefin Polymerization" Poster Presentation at *the International Symposium on Relationships between Heterogeneous and Homogeneous Catalysis XIII*, Berkeley, CA July 16-20, 2007 and manuscript in preparation.
- (8) (a) Chum, P. S.; Kruper, W. J.; Guest, M. J. *Adv. Mater.* **2000**, *12*, 1759-1767. (b) Cheung, Y. W.; Guest, M. J. *J. Polym. Sci.: Part B: Polym. Phys.* **2000**, *38*, 2976-2987. (c) Chen, H.; Guest, M. J.; Chum, S.; Hiltner, A.; Baer E. *J. Appl. Polym. Sci.* **1998**, *70*, 109-119.

- (9) (a) Aaltonen, P.; Seppälä, J.; Matilainen, L.; Leskelä, M. *Macromolecules* **1994**, *27*, 3136-3138. (b) Mani, P.; Burns, C. M. *Macromolecules* **1991**, *24*, 5475-5477. (c) Soga, K.; Lee, D. H.; Yanagihara, H. *Polym. Bull.* **1988**, *20*, 237-241.
- (10) (a) Zhang, H.; Nomura, K. *Macromolecules* **2006**, *39*, 5266-5274. (b) Zhang, H.; Nomura, K. *J. Am. Chem. Soc.* **2005**, *127*, 9364-9365. (c) Nomura, K.; Okumura, H.; Komatsu, T.; Naga, N. *Macromolecules* **2002**, *35*, 5388-5395. (d) Nomura, K.; Komatsu, T.; Imanishi, Y. *Macromolecules* **2000**, *33*, 8122-8124. (e) Lee, D. H.; Yoon, K. B.; Kim, H. J.; Woo, S. S.; Noh, S. K. *J. Appl. Polym. Sci.* **1998**, *67*, 2187-2198. (f) Wu, Q.; Ye, Z.; Gao, Q.; Lin, S. *Macromol. Chem. Phys.* **1998**, *199*, 1715-1720. (g) Xu, G.; Lin, S. *Macromolecules* **1997**, *30*, 685-693. (h) Pellecchia, C.; Pappalardo, D.; D'Arco, M.; Zambelli, A. *Macromolecules* **1996**, *29*, 1158-1162. (i) Oliva, L.; Mazza, S.; Longo, P. *Macromol. Chem. Phys.* **1996**, *197*, 3115-3122. (j) Oliva, L.; Izzo, L.; Longo, P. *Macromol. Rapid Commun.* **1996**, *17*, 745-748. (k) Aaltonen, P.; Seppala, J. *Eur. Polym. J.* **1995**, *31*, 79-83. (l) Aaltonen, P.; Seppala, J. *Eur. Polym. J.* **1994**, *30*, 683-687. (m) Longo, P.; Grassi, A.; Oliva, L. *Macromol. Chem. Phys.* **1990**, *191*, 2387-2396.
- (11) (a) Capacchione, C.; Proto, A.; Ebeling, H.; Mülhaupt, R.; Okuda, J. *J. Polym. Sci., Part A: Polym. Chem.* **2006**, *44*, 1908-1913. (b) Luo, Y.; Baldamus, J.; Hou, Z. *J. Am. Chem. Soc.* **2004**, *126*, 13910-13911. (c) Sernetz, F. G.; Mülhaupt, R.; Fokken, S.; Okuda, J. *Macromolecules* **1997**, *30*, 1562-1569.
- (12) (a) Arriola, D. J.; Bokota, M.; Campbell, R. E., Jr.; Klosin, J.; LaPointe, R. E.; Redwine, O. D.; Shankar, R. B.; Timmers, F. J.; Abboud, K. A. *J. Am. Chem. Soc.* **2007**, *129*, 7065-7076. (b) Noh, S. K.; Lee, M.; Kum, D. H.; Kim, K.; Lyoo, W. S.; Lee, D. H. *J. Polym. Sci., Part A: Polym. Chem.* **2004**, *42*, 1712-1723. (c) Noh, S. K.; Yang, Y.; Lyoo, W. S. *J.*

- Appl. Polym. Sci.* **2003**, *90*, 2469-2474. (d) Sukhova, T. A.; Panin, A. N.; Babkina, O. N.; Bravaya, N. M. *J. Polym. Sci., Part A: Polym. Chem.* **1999**, *37*, 1083-1093. (e) Xu, G. *Macromolecules* **1998**, *31*, 2395-2402. (f) Sernetz, F. G.; Mülhaupt, R.; Amor, F.; Eberle, T.; Okuda, J. *J. Polym. Sci., Part A: Polym. Chem.* **1997**, *35*, 1571-1578. (g) Timmers, F. J. *US Patent 5703187*, **1997**. (h) Sernetz, F. G.; Mülhaupt, R.; Waymouth, R. M. *Macromol. Chem. Phys.* **1996**, *197*, 1071-1083. (i) Stevens, J. C.; Timmers, F. J.; Wilson, D. R.; Schmidt, G. F.; Nickias, P. N.; Rosen, R. K.; Knight, G. W.; Lai, S. Y. *Eur. Pat. Appl.* **1991**, *58*, EP 0 416 815 A2
- (13) (a) Kern, R. J.; Hurst, H. G.; Richard, W. R. *J. Polym. Sci.* **1960**, *45*, 195-204. (b) Overberger, C.; Ang, F.; Mark, H. *J. Polym. Sci.* **1959**, *35*, 381-389. (c) Natta, G.; Pino, P.; Corradini, P.; Danusso, F.; Mantica, E.; Mazzanti, G.; Moraglio, G. *J. Am. Chem. Soc.* **1955**, *77*, 1708-1710.
- (14) For examples of anionic isospecific styrene polymerization, see: (a) Makino, T.; Hogen-Esch, T. E. *Macromolecules* **1999**, *32*, 5712-5714. (b) Cazzaniga, L.; Cohen, R. E. *Macromolecules* **1989**, *22*, 4125-4128.
- (15) (a) De Carlo, F.; Capacchione, C.; Schiavo, V.; Proto, A. *J. Polym. Sci., Part A: Polym. Chem.* **2006**, *44*, 1486-1491. (b) Beckerle, K.; Manivannan, R.; Spaniol, T. P.; Okuda, J. *Organometallics* **2006**, *25*, 3019-3026. (c) Capacchione, C.; Manivannan, R.; Barone, M.; Beckerle, K.; Centore, R.; Oliva, L.; Proto, A.; Tuzi, A.; Spaniol, T. P.; Okuda, J. *Organometallics* **2005**, *24*, 2971-2982. (d) Capacchione, C.; Proto, A.; Ebeling, H.; Mülhaupt, R.; Möller, K.; Spaniol, T. P.; Okuda, J. *J. Am. Chem. Soc.* **2003**, *125*, 4964-4965.
- (16) (a) Knjazhanski, S. Y.; Cadenas, G.; García, M.; Pérez, C. M.; Nifant'ev, I. E.; Kashulin, I.

- A.; Ivchenko, P. V.; Lyssenko, K. A. *Organometallics* **2002**, *21*, 3094-3099. (b) Nomura, K.; Komatsu, T.; Imanishi, Y. *Macromolecules* **2000**, *33*, 8122-8124. (c) Kaminsky, W.; Lenk, S.; Scholz, V.; Roesky, H. W.; Herzog, A. *Macromolecules* **1997**, *30*, 7647-7650. (d) Foster, P. F.; Chien, J. C. W.; Rausch, M. D. *Organometallics* **1996**, *15*, 2404-2409. (e) Pellecchia, C.; Longo, P.; Proto, A.; Zambelli, A. *Makromol.Chem., Rapid Commun.* **1992**, *13*, 265-268. (f) Ishihara, N.; Kuramoto, M.; Uoi, M. *Macromolecules* **1988**, *21*, 3356-3360.
- (17) (a) Chen, J.; Li, Y.; Wu, J.; Hu, N. *J. Mol. Cat. A: Chem.* **2005**, *232*, 1-7. (b) Kim, Y.; Han, Y.; Hwang, J.; Kim, M. W.; Do, Y. *Organometallics* **2002**, *21*, 1127-1135.
- (18) Zambelli, A.; Oliva, L.; Pellecchia, C. *Macromolecules* **1989**, *22*, 2129-2130.
- (19) For examples of phenyl ring "back-biting" to d^0 Ti or Zr, see: (a) Manke, D. R.; Nocera, D. G. *Inorg. Chim. Acta* **2003**, *345*, 235-240. (b) Cotton, F. A.; Murillo, C. A.; Petrukhina, M. A. *J. Organomet. Chem.* **1999**, *573*, 78-86. (c) Warren, T. H.; Schrock, R. R.; Davis, W. M. *Organometallics* **1996**, *15*, 562-569. (d) Bochmann, M.; Lancaster, S. J.; Hursthouse, M. B.; Malik, K. M. A. *Organometallics* **1994**, *13*, 2235-2243. (e) Pellecchia, C.; Grassi, A.; Zambelli, A. *Organometallics* **1994**, *13*, 298-302. (f) Pellecchia, C.; Grassi, A.; Immirzi, A. *J. Am. Chem. Soc.* **1993**, *115*, 1160-1162. (g) Pellecchia, C.; Immirzi, A.; Grassi, A.; Zambelli, A. *Organometallics* **1993**, *12*, 4473-4478. (h) Bochmann, M.; Lancaster, S. J. *Organometallics* **1993**, *12*, 633-640. (i) Jordan, R. F.; LaPointe, R. E.; Bajgur, C. S.; Echols, S. F.; Willett, R. *J. Am. Chem. Soc.* **1987**, *109*, 4111-4113. (j) Stoeckli-Evans, H. *Helv. Chim. Acta* **1974**, *57*, 684-689. (k) Bassi, I. W.; Allegra, G.; Scordamaglia, R.; Chioccola, G. *J. Am. Chem. Soc.* **1971**, *93*, 3787-3788.

- (20) For studies of styrene insertion regiochemistry, see: (a) Capacchione, C.; Proto, A.; Ebeling, H.; Mulhaupt, R.; Möller, K.; Spaniol, T. P.; Okuda, J. *J. Am. Chem. Soc.* **2003**, *125*, 4964-4965. (b) Izzo, L.; Napoli, M.; Oliva, L. *Macromolecules* **2003**, *36*, 9340-9345. (c) Caporaso, L.; Izzo, L.; Zappile, S.; Oliva, L. *Macromolecules* **2000**, *33*, 7275-7282. (d) Pellecchia, C.; Pappalardo, D.; Oliva, L.; Zambelli, A. *J. Am. Chem. Soc.* **1995**, *117*, 6593-6594. (e) Zambelli, A.; Longo, P.; Pellecchia, C.; Grassi, A. *Macromolecules* **1987**, *20*, 2035-2037. (f) Pellecchia, C.; Longo, P.; Grassi, A.; Ammendola, P.; Zambelli, A. *Makromol. Chem., Rapid Commun.* **1987**, *8*, 277-279.
- (21) Pangborn, A. B.; Giardello, M. A.; Grubbs, R. H.; Rosen, R. K.; Timmers, F. J. *Organometallics* **1996**, *15*, 1518-1520.
- (22) Protivova, J.; Pospisil, J.; Zikmund, L. *J. Polym. Sci. Polym. Symposia* **1973**, *40* 233-243.
- (23) (a) Fink, G.; Richter, W. J. In *Polymer Handbook*, 4th ed.; Brandup, J., Immergut, E. H., Grulke, E. A., Eds.; John Wiley & Sons: New York, **1999**; Vol. II; pp 329-337. (b) Oliva, L.; Longo, P.; Izzo, L.; Di Serio, M. *Macromolecules* **1997**, *30*, 5616-5619.
- (24) For theoretical studies on styrene homopolymerization, see: (a) Yang, S. H.; Huh, J.; Jo, W. H. *Organometallics* **2006**, *25*, 1144-1150. (b) Yang, S. H.; Huh, J.; Yang, J. S.; Jo, W. H. *Macromolecules* **2004**, *37*, 5741-5751. (c) Nifant'ev, I. E.; Ustynyuk, L. Y.; Besedin, D. V. *Organometallics* **2003**, *22*, 2619-2629. (d) Minieri, G.; Corradini, P.; Guerra, G.; Zambelli, A.; Cavallo, L. *Macromolecules* **2001**, *34*, 5379-5385. (e) Minieri, G.; Corradini, P.; Zambelli, A.; Guerra, G.; Cavallo, L. *Macromolecules* **2001**, *34*, 2459-2468.
- (25) For studies of styrene coordination with cationic metal center, see: (a) Kaminsky, W.; Lenk, S.; Scholtz, V.; Roesky, H. W.; Herzog, A. *Macromolecules* **1997**, *30*, 7647-7650.

- (b) Flores, J. C.; Wood, J. S.; Chien, J. C.W.; Rausch, M. D. *Organometallics* **1996**, *15*, 4944-4950. (c) Grassi, A.; Zambelli, A.; Laschi, F. *Organometallics* **1996**, *15*, 480-482.
- (26) For polystyrene end group analysis, see: (a) Caporaso, L.; Izzo, L.; Sisti, I.; Oliva, L. *Macromolecules* **2002**, *35*, 4866-4870. (b) Zambelli, A.; Longo, P.; Pellicchia, C.; Grassi, A. *Macromolecules*, **1987**, *20*, 2035-2037. (c) Sato, H.; Tanaka Y. *Macromolecules* **1984**, *17*, 1964-1966.
- (27) For theoretical studies on monomer insertion in ethylene + styrene copolymerizations, see: (a) Ramos, J.; Muñoz-Escalona, A.; Martínez, S.; Martínez-Salazar, J.; Cruz, V. *J. Chem. Phys.* **2005**, *122*, 074901/1-074901/4. (b) Yokota, K.; Kohsaka, T.; Ito, K.; Ishihara, N. *J. Polym. Sci., Part A: Polym. Chem.* **2005**, *43*, 5041-5048. (c) Martínez, S.; Exposito, M. T.; Ramos, J.; Cruz, V.; Martínez, M. C.; López, M.; Muñoz-Escalona, A.; Martínez-Salazar, J. *J. Polym. Sci., Part A: Polym. Chem.* **2005**, *43*, 711-725. (d) Martínez, S.; Cruz, V.; Muñoz-Escalona, A.; Martínez-Salazar, J. *Polymer* **2003**, *44*, 295-306. (e) Yang S. H.; Jo, W. H.; Noh, S. K. *J. Chem. Phys.* **2003**, *119*, 1824-1837. (f) Muñoz-Escalona, A.; Cruz, V.; Mena, N.; Martínez, S.; Martínez-Salazar, J. *Polymer* **2002**, *43*, 7017-7026. (g) Oliva, L.; Caporaso, L.; Pellicchia, C.; Zambelli, A. *Macromolecules* **1995**, *28*, 4665-4667.
- (28) (a) Hong, S.; Marks, T. J. *Acc. Chem. Res.* **2004**, *37*, 673-686. (b) Gagne, M. R.; Stern, C. L.; Marks, T. J. *J. Am. Chem. Soc.* **1992**, *114*, 275-294.
- (29) (a) Bouwkamp, M. W.; de Wolf, J.; del Hierro Morales, I.; Gercama, J.; Meetsma, A.; Troyanov, S. I.; Hessen, B.; Teuben, J. H. *J. Am. Chem. Soc.* **2002**, *124*, 12956-12957. (b) Kawabe, M.; Murata, M. *Macromol. Chem. Phys.* **2001**, *202*, 2440-2446. (c) Rybtchinski,

- B.; Konstantinovsky, L.; Shimon, L. J. W.; Vigalok, A.; Milstein, D. *Chem. Eur. J.* **2000**, *6*, 3287-3292. (d) Carr, N.; Mole, L.; Orpena, A. G.; Spencer, G. L. *J. Chem. Soc., Dalton Trans.* **1992**, *18*, 2653-2662. (e) Peng, T. S.; Gladysz, J. A. *J. Am. Chem. Soc.* **1992**, *114*, 4174-4181. (f) Agbossou, S. K.; Bodner, G. S.; Patton, A. T.; Gladysz, J. A. *Organometallics* **1990**, *9*, 1184-1191. (g) Schmidt, G. F.; Brookhart, M. *J. Am. Chem. Soc.* **1985**, *107*, 1443-1444.
- (30) The solubility of ethylene is reported to be 0.117 mol/L in toluene^{30a} and 0.118 mol/L in chlorobenzene^{30b} under the present polymerization conditions (25 °C, 1.0 atm): (a) Atiqullah, M.; Hammawa, H.; Hamid, H. *Eur. Polym. J.* **1998**, *34*, 1511-1520. (b) Sahgal, A.; La, H. M.; Hayduk, W. *Can. J. Chem. Eng.* **1978**, *56*, 354-357.
- (31) Chen, Y. X.; Marks, T. J. *Organometallics* **1997**, *16*, 3649-3657.
- (32) (a) Amor, F.; Butt, A.; du Plooy, K. E.; Spaniol, T. P.; Okuda, J. *Organometallics* **1998**, *17*, 5836-5849. (b) Amor, F.; Okuda, J. *J. Organomet. Chem.* **1996**, *520*, 245-248.
- (33) (a) Latesky, S. L.; McMullen, A. K.; Niccolai, G. P.; Rothwell, I. P.; Huffman, J. C. *Organometallics* **1985**, *4*, 902-908. (b) Lubben, T. V.; Wolczanski, P. T.; Van Duyne, G. D. *Organometallics* **1984**, *3*, 977-983. (c) Mintz, E. A.; Moloy, K. G.; Marks, T. J.; Day, V. W. *J. Am. Chem. Soc.* **1982**, *104*, 4692-4695. (d) Wolczanski, P. T.; Bercaw, J. E. *Organometallics* **1982**, *1*, 793-799.
- (34) (a) Mashima, K.; Nakamura, A. *J. Organomet. Chem.* **1992**, *428*, 49-58. (b) Brookhart, M.; Green, M. L. H. *J. Organomet. Chem.* **1983**, *250*, 395-408.
- (35) Carpenetti, D. W.; Kloppenburg, L.; Kupec, J. T.; Petersen, J. L. *Organometallics* **1996**, *15*, 1572-1581.
- (36) (a) Motta, A.; Fragalà, I. L.; Marks, T. J. *J. Am. Chem. Soc.* **2007**, *129*, 7327-7338. (b)

- Xu, Z.; Vanka, K.; Ziegler, T. *Organometallics* **2004**, *23*, 104-116. (c) Nifant'ev, I. E.; Ustynyuk, L. Y.; laikov, D. N. *Organometallics* **2001**, *20*, 5375-5393.
- (37) Chan, M. S. W.; Vanka, K.; Pye, C. C.; Ziegler, T. *Organometallics* **1999**, *18*, 4624-4636.
- (38) Luo, L.; Marks, T. J. *Top. Catal.* **1999**, *7*, 97-106.
- (39) (a) Nelson, G. L.; Levy, G. C.; Cargioli, J. D. *J. Am. Chem. Soc.* **1972**, *94*, 3089-3094. (b) Spiesecke, H.; Schneider, W. G. *J. Chem. Phys.* **1961**, *35*, 731-738.

Chapter 2

- (1) (a) Cao, Y.; Irwin, P. C.; Younsi, K. *IEEE Trans. Dielectr. Electr. Insul.* **2004**, *11*, 797-807. (b) Nalwa, H. S. Ed. *Handbook of Low and High Dielectric Constant Materials and their Applications* Academic Press: New York, **1999**; Vol. 2. (c) Sarjeant, W. J.; Zirnheld, J.; MacDougall, F. W. *IEEE Trans. Plasma Sci.* **1998**, *26*, 1368-1392.
- (2) (a) Tanaka, T.; Montanari, G. C.; Mülhaupt, R. *IEEE Trans. Dielectr. Electr. Insul.* **2004**, *11*, 763-784. (b) Newnham, R. E. *Annu. Rev. Mater. Sci.* **1986**, *16*, 47-68.
- (3) (a) Saha, S. K. *Phys. Rev. B* **2004**, *69*, 1254161-125464. (b) Nelson, J. K.; Utracki, L. A.; MacCrone, R. K.; Reed, C. W. *IEEE Conf. Electr. Insul. Dielectr. Phenomena* **2004**, 314-317. (c) Li, J. *Phys. Rev. Lett.* **2003**, *90*, 217601/1-4.
- (4) Dang, Z.; Wu, J.; Fan, L.; Nan, C. *Chem. Phys. Lett.* **2003**, 376, 389-394.
- (5) (a) Parvatikar, N.; Ambika Prasad, M. V. N. *J. Appl. Polym. Sci.* **2006**, *100*, 1403-1405. (b) Badheka, P.; Magadala, V.; Gopi Devaraju, N.; Lee, B. I.; Kim, E. S. *J. Appl. Polym. Sci.* **2006**, *99*, 2815-2821. (c) Xie, S.; Zhu, B.; Xu, Z.; Xu, Y. *Mater. Lett.* **2005**, *59*, 2403-2407. (d) Schroeder, R.; Majewski, L.; Grell, M. *Adv. Mater.* **2005**, *17*, 1535-1539. (e) Bai, Y.; Cheng, Z.; Bharti, V.; Xu, H.; Zhang, Q. *Appl. Phys. Lett.* **2000**, *76*, 3804-3806.
- (6) (a) He, A.; Wang, L.; Li, J.; Dong, J.; Han, C. C. *Polymer* **2006**, *47*, 1767-1771. (b) Ginzburg, V. V.; Myers, K.; Malowinski, S.; Cieslinski, R.; Elwell, M.; Bernius, M. *Macromolecules* **2006**, *39*, 3901-3906. (c) Mizutani, T.; Arai, K.; Miyamoto, M.; Kimura, Y. *J. Appl. Polym. Sci.* **2006**, *99*, 659-669. (d) R. Popielarz, R.; Chiang, C. K.; Nozaki, R.; Obrzut, J. *Macromolecules* **2001**, *34*, 5910-5915.

- (7) (a) Lu, J.; Moon, K. S.; Xu, J.; Wong, C. P. *J. Mater. Chem.* **2006**, *16*, 1543-1548. (b) Yogo, T.; Yamamoto, T.; Sakamoto, W.; Hirano, S. *J. Mater. Res.* **2004**, *19*, 3290-3297.
- (8) (a) Vaia, R. A.; Maguire, J. F. *Chem. Mater.* **2007**, *19*, 2736-2751. (b) Mackay, M. E.; Tuteja, A.; Duxbury, P. M.; Hawker, C. J.; Van Horn, B.; Guan, Z.; Chen, G.; Krishnan, R. S. *Science* **2006**, *311*, 1740-1743. (c) Lin, Y.; Boeker, A.; He, J.; Sill, K.; Xiang, H.; Abetz, C.; Li, X.; Wang, J.; Emrick, T.; Long, S.; Wang, Q.; Balazs, A.; Russell, T. P. *Nature* **2005**, *434*, 55-59.
- (9) (a) Chen, G.; Davies, A. E. *IEEE Trans. Dielectr. Electr. Insul.* **2000**, *7*, 401-407. (b) Khalil, M. S. *IEEE Trans. Dielectr. Electr. Insul.* **2000**, *7*, 261-268.
- (10) (a) Maliakal, A.; Katz, H. E.; Cotts, P. M.; Subramoney, S.; Mirau, P. *J. Am. Chem. Soc.* **2005**, *127*, 14655-14662. (b) Rusa, M.; Whitesell, J. K.; Fox, M. A. *Macromolecules* **2004**, *37*, 2766-2774. (c) Bartholome, C.; Beyou, E.; Bourgeat-Lami, E.; Chaumont, P.; Zydowicz, N. *Macromolecules* **2003**, *36*, 7946-7952. (d) Corbierre, M. K.; Cameron, N. S.; Sutton, M.; Mochrie, S. G. J.; Lurio, L. B.; Rühm, A.; Lennox, R. B. *J. Am. Chem. Soc.* **2001**, *123*, 10411-10412. (e) von Werne, T.; Patten, T. E. *J. Am. Chem. Soc.* **2001**, *123*, 7497-7505. (f) Nuß, S.; Böttcher, H.; Wurm, H.; Hallensleben, M. L. *Angew. Chem. Int. Ed.* **2001**, *40*, 4016-4018.
- (11) (a) Kaminsky, W.; Funck, A.; Wiemann, K. *Macromol. Symp.* **2006**, *239*, 1-6. (b) Li, K.-T.; Kao, Y.-T. *J. Appl. Polym. Sci.* **2006**, *101*, 2573-2580. (c) du Fresne von Hohenesche, C.; Unger, K. K.; Eberle, T. *J. Mol. Cat. A: Chem.* **2004**, *221*, 185-199. (d) Fink, G.; Steinmetz, B.; Zechlin, J.; Przybyla, C.; Tesche, B. *Chem. Rev.* **2000**, *100*, 1377-1390.
- (12) Rabuffi, M.; Picci, G. *IEEE Trans. Plasma Sci.* **2002**, *30*, 1939-1942.

- (13) Guo, N.; DiBenedetto, S. A.; Kwon, D.-K.; Wang, L.; Russell, M. T.; Lanagan, M. T.; Facchetti, A.; Marks, T. J. *J. Am. Chem. Soc.* **2007**, *129*, 766-767.
- (14) Pangborn, A. B.; Giardello, M. A.; Grubbs, R. H.; Rosen, R. K.; Timmers, F. J. *Organometallics* **1996**, *15*, 1518-1520.
- (15) (a) Ma, D.; Hugener, T. A.; Siegel, R. W.; Christerson, A.; Mårtensson, E.; Önnby, C.; Schadler, L. S. *Nanotechnology* **2005**, *16*, 724-731. (b) Ma, D.; Siegel, R. W.; Hong, J.; Schadler, L. S.; Mårtensson, E.; Önnby, C. *J. Mater. Res.* **2004**, *19*, 857-863.
- (16) Yoon, M.-H.; Kim, C.; Facchetti, A.; Marks, T. J. *J. Am. Chem. Soc.* **2006**, *128*, 12851-12869.
- (17) (a) Jenkins, R.; Snyder, R. L. In *Introduction to X-ray Powder Diffractometry*; Winefordner, J. D., Ed.; Wiley: New York, **1996**; pp 89-91. (b) Scherrer, P. *Gött. Nachr.* **1918**, *2*, 98-100.
- (18) (a) Busico, V.; Cipullo, R.; Monaco, G.; Vacatello, M. *Macromolecules* **1997**, *30*, 6251-6263. (b) Busico, V.; Cipullo, R.; Corradini, P.; Landriani, L.; Vacatello, M.; Segre, A. L. *Macromolecules* **1995**, *28*, 1887-1892. (c) Zambelli, A.; Dorman, D. E.; Brewster, A. I. R.; Bovey, F. A. *Macromolecules* **1973**, *6*, 925-926.
- (19) Miller, S. A.; Bercaw, J. E. *Organometallics* **2006**, *25*, 3576-3592.
- (20) Auriemma, F.; De Rosa, C. *Macromolecules* **2002**, *35*, 9057-9068.
- (21) Friedrich, K.; Fakirov, S.; Zhang, Z. Eds.; In *Polymer Composites: From Nano- to Macro-Scale*; Springer: New York, **2005**.
- (22) Kulshrestha, A. K.; Talapatra, S. In *Handbook of Polyolefins*; Vasile, C., Ed.; Marcel Dekker: New York, **2000**; pp 1-70.
- (23) McKnight, A. L.; Waymouth, R. M. *Chem. Rev.* **1998**, *98*, 2587-2598.

- (24) (a) Qiu, X.; Redwine, D.; Gobbi, G.; Nuamthanom, A.; Rinaldi, P. L. *Macromolecules* **2007**, *40*, ASAP. (b) Liu, W.; Ray, D. G., III; Rinaldi, P. L. *Macromolecules* **1999**, *32*, 3817-3819. (c) Galland, G. B.; de Souza, R. F.; Mauler, R. S.; Nunes, F. F. *Macromolecules* **1999**, *32*, 1620-1625.
- (25) (a) Ishihara, N.; Kuramoto, M.; Uoi, M. *Macromolecules* **1988**, *21*, 3356-3360. (b) Ishihara, N.; Seimiya, T.; Kuramoto, M.; Uoi, M. *Macromolecules* **1986**, *19*, 2464-2465.
- (26) Murugaraj, P.; Mainwaring, D.; Mora-Huertas, N. *J. Appl. Phys.* **2005**, *98*, 054304/1-6.
- (27) DiBenedetto, S. A.; Paci, I.; Facchetti, A.; Marks, T. J.; Ratner, M. A. *J. Phys. Chem. B.*, **2006**, *110*, 22394-22399 and references therein.
- (28) (a) Murata, Y.; Sekiguchi, Y.; Lnoue, Y.; Kanaoka, M. *Proc. 2005 Intern. Sympos. Electr. Insul.* **2005**, 650-653. (b) Nelson, J. K.; Fothergill, J. C. *Nanotechnology* **2004**, *15*, 586-595.
- (29) Fujita, F.; Ruike, M.; Baba, M. *IEEE Intern. Sympos. Electr. Insul.* **1996**, *2*, 738-741.
- (30) (a) Imai, T.; Sawa, F.; Nakano, T.; Ozaki, T.; Shimizu, T.; Kozako, M.; Tanaka, T. *IEEE Trans. Dielectr. Electr. Insul.* **2006**, *13*, 319-326. (b) Uehara, H.; Kudo, K. *IEEE Trans. Dielectr. Electr. Insul.* **2005**, *12*, 1266-1271.
- (31) (a) Gorzkowski, E. P.; Pan, M.-J.; Bender, B.; Wu, C. C. M. *Ceram. Trans.* **2006**, *179*, 27-34. (b) Pan, M.-J.; Lanagan, M.; Bender, B. A.; Cheng, C.-T. *Ceram. Trans.* **2005**, *169*, 187-193.
- (32) Chu, B.; Zhou, X.; Neese, B.; Zhang, Q.-M.; Bauer, F. *Ferroelectrics* **2006**, *331*, 35-42.
- (33) (a) Gilbert, L. J.; Schuman, T. P.; Dogan, F. *Ceram. Trans.* **2006**, *179*, 17-26. (b) Slenes, K. M.; Winsor, P.; Scholz, T.; Hudis, M. *IEEE Trans. Magn.* **2001**, *37*, 324-327.
- (34) Brosseau, C.; Beroual, A.; Boudida, A. *J. Appl. Phys.* **2000**, *88*, 7278-7288.

- (35) Green, N. G.; Jones, T. B. *J. Phys. D: Appl. Phys.* **2007**, *40*, 78-85.
- (36) Sihvola, A. *Electromagnetic Mixing Formulas and Applications*; Institution of Electrical Engineers: London, **1999**; pp 61-84.
- (37) Yang, R.; Qu, J.; Marinis, T.; Wong, C.P. *IEEE Trans. on Comp. and Pack. Tech.* **2000**, *23*, 680-683.

Curriculum Vitae

Name: Neng Guo
Born: Dangshan, Anhui, P. R. China

EDUCATION

Northwestern University, Evanston, IL

Ph.D. in Chemistry (expected June 2007)

- Advisor: Tobin J. Marks, Vladimir N. Ipatieff Professor of Catalytic Chemistry and Professor of Materials Science and Engineering
- Thesis topic: "Bimetallic Effects in the Homopolymerization of Styrene and Copolymerization of Ethylene and Styrenic Comonomers. Scope, Kinetics, and Mechanism/Supported Metallocene Catalysis for In Situ Synthesis of High Energy Density Metal Oxide Nanocomposites"

University of Science and Technology of China, Hefei, Anhui, China

B.S. in Chemistry, July 2001

Undergraduate research under the guidance of Professor Yitai Qian

RESEARCH EXPERIENCE

Northwestern University, Evanston, IL

- Synthesized and characterized air-sensitive group IV metallocene complexes.
- Studied the catalyst/cocatalyst nuclearity effects in group IV metallocene-catalyzed styrene homopolymerization and ethylene-styrene copolymerization.
- Participated in the synthesis and characterization of a tetranuclear cocatalyst/activator used for the synthesis of linear low density polyethylene (LLDPE).
- Synthesized and characterized high permittivity, high breakdown strength inorganic metal oxide-polymer nanocomposite materials for supercapacitors.

University of Science and Technology of China, Hefei, Anhui, China

- Hydrothermally synthesized and characterized a series of lanthanide compounds with improved photoluminescent properties.
- Solvothermally synthesized and characterized stannous oxide crystals with different morphologies.

Affiliations

- American Chemical Society, 2002-present
- Chicago Local Section of the American Chemical Society, 2002-present

Publications

- **Guo, N.**; DiBenedetto, S. A.; Kwon, D.; Wang, L.; Russell, M. T.; Lanagan, M. T.; Facchetti, A.; Marks, T. J. "Supported Metallocene Catalysis for In Situ Synthesis of High Energy Density Metal Oxide Nanocomposites." *J. Am. Chem. Soc.* **2007**, *129*, 766-767.

- **Guo, N.**; Li, L.; Marks, T. J. “Bimetallic Catalysis for Styrene Homopolymerization and Ethylene-Styrene Copolymerization. Exceptional Comonomer Selectivity and Insertion Regiochemistry.” *J. Am. Chem. Soc.* **2004**, *126*, 6542-6543.
- **Guo, N.**; Stern, C. L.; Marks, T. J. “Bimetallic Effects in the Homopolymerization of Styrene and Copolymerization of Ethylene and Styrenic Comonomers. Scope, Kinetics, and Mechanism.” Submitted.
- **Guo, N.**; DiBenedetto, S. A.; Tewari, P.; Lanagan, M. T.; Ratner, M. A.; Marks, T. J. “Catalytic In Situ Synthesis of High Energy Storage Density Metal Oxide-Polyolefin Nanocomposites Using Supported Metallocenes. Systematics of Nanoparticle, Shape, and Interfacial Characteristics on Leakage Current Density, Permittivity, and Breakdown Strength.” Manuscript in preparation.
- Wang, J.; **Guo, N.**; Chen, M. C.; Marks, T. J. “Polynuclear Catalysis: Enhanced Enchainment Cooperativity between Different Single-site Olefin Polymerization Catalysts by Ion Pairing with a Tetranuclear Cocatalyst.” To be submitted.
- Wang, J.; Li, H.; **Guo, N.**; Li, L.; Stern, C. L.; Marks, T. J. “Covalently Linked heterobimetallic Catalysts for Olefin Polymerization.” *Organometallics* **2004**, *23*, 5112-5114.
- Han, Z.; Qian, Y.; Tang, K.; Lu, G.; Yu, S.; **Guo, N.** “Hydrothermal Deposition of Cerium Hydroxycarbonate Thin Films on Glass.” *Inorg. Chem. Comm.* **2003**, *6*, 1117-1121.
- Han, Z.; **Guo, N.**; Li, F.; Zhang, W.; Zhao, H.; Qian, Y. “Solvothermal Preparation and Morphological Evolution of Stannous Oxide Powders.” *Mater. Lett.* **2001**, *48*, 99-103.
- Han, Z.; **Guo, N.**; Tang, K.; Yu, S.; Zhao, H.; Qian, Y. “Hydrothermal Crystal Growth and Characterization of Cerium Hydroxycarbonates.” *J. Cryst. Growth* **2000**, *219*, 315-318.
- Han, Z.; Qian, Y.; Yu, S.; Tang, K.; Zhao, H.; **Guo, N.** “Hydrothermal Evolution of the Thiourea-Cerium(III) Nitrate System: Formation of Cerium Hydroxycarbonate and Hydroxysulfate.” *Inorg. Chem.* **2000**, *39*, 4380-4382.

Meetings and Presentations

- **Guo, N.**; DiBenedetto, S. A.; Marks, T. J.; Kwon, D.-K.; Lanagan, M. T. “Supported Metallocene Catalysis for In Situ Synthesis of High Energy Density Metal Oxide Nanocomposites.” *Abstracts of Papers, 233rd ACS National Meeting, Chicago, IL, United States, March 25-29, 2007.*
- **Guo, N.**; Marks, T. J. “Bimetallic Effects in the Homopolymerization of Styrene and Copolymerization of Ethylene and Styrenic Comonomers. Scope, Kinetics, and Mechanism” *Gordon Research Conference on Organometallic Chemistry, Newport, RI July 9-14, 2006.*
- **Guo, N.**; Marks, T. J. “Supported Ziegler-Natta Metallocene Catalysis. In Situ Route to High- ϵ_r Metal Oxide-Polyolefin Nanocomposites for Energy Storage.” *Center for Dielectric Studies, St. Louis, MO May 15-17, 2006.*
- **Guo, N.**; Marks, T. J. “Supported Ziegler-Natta Metallocene Catalysis. In Situ Route to High- ϵ_r Metal Oxide-Polyolefin Nanocomposites for Energy Storage.” *Center for Dielectric Studies, Annapolis, MD November 10-11, 2005.*

- **Guo, N.;** Li, L.; Marks, T. J. “Bimetallic Catalysis for Styrene Homopolymerization and Ethylene-Styrene Copolymerization. Exceptional Comonomer Selectivity and Insertion Regiochemistry.” *Abstracts of Papers, 229th ACS National Meeting, San Diego, CA, United States, March 13-17, 2005.*
- **Guo, N.;** Li, L.; Marks, T. J. “Bimetallic Effects on Styrene Homopolymerization and Ethylene-Styrene Copolymerization: Spectroscopy, Kinetics, and Mechanism.” *International Symposium on Relationships between Heterogeneous and Homogeneous Catalysis XI, Evanston, IL July 20-25, 2003.*